Summer 8-5-2025

Search for Higgs Boson Pair Production in the Two Light Leptons and One Tau Final State Using Proton-Proton Collision Data With $\sqrt{s} = 13$ TeV at the LHC From the ATLAS Detector

Susan Bataju
Southern Methodist University, sbataju@smu.edu

Recommended Citation

Bataju, Susan, "Search for Higgs Boson Pair Production in the Two Light Leptons and One Tau Final State Using Proton-Proton Collision Data With $\sqrt{s} = 13$ TeV at the LHC From the ATLAS Detector" (2025). *Physics Theses and Dissertations*. 21.
https://scholar.smu.edu/hum_sci_physics_etds/21

SEARCH FOR HIGGS BOSON PAIR PRODUCTION IN THE TWO LIGHT LEPTONS AND ONE TAU FINAL STATE USING PROTON-PROTON COLLISION DATA WITH $\sqrt{S} = 13$ TEV AT THE LHC FROM THE ATLAS DETECTOR

Approved by:

Dr. Allison Deiana
Associate Professor

Dr. Haleh K Hadavand
Associate Professor

Dr. Matthew Klein
Assistant Professor

Dr. Ryszard Stroynowski
Professor

SEARCH FOR HIGGS BOSON PAIR PRODUCTION IN THE TWO LIGHT LEPTONS AND ONE TAU FINAL STATE USING PROTON-PROTON COLLISION DATA WITH $\sqrt{S} = 13$ TEV AT THE LHC FROM THE ATLAS DETECTOR

A Dissertation Presented to the Graduate Faculty of the
Dedman College
Southern Methodist University
in
Partial Fulfillment of the Requirements
for the degree of
Doctor of Philosophy
with a
Major in Physics
by
Susan Bataju

B.S., Physics, University of Texas at Arlington

August 5, 2025

ACKNOWLEDGMENTS

I would like to express my sincerest gratitude to my advisor, Dr. Allison Deiana, for her exceptional guidance, expertise, and unwavering support throughout my graduate school journey.

I am also deeply thankful to Dr. Bartlomiej Henryk Zabinski, Dr. Katharine Leney, Dr. Rohin Narayan, and Dr. Santosh Parajuli for their valuable feedback, encouragement, and insightful discussions. I would further like to extend my appreciation to the members of the ATLAS Collaboration, especially the Di-Higgs Multilepton team, for their support and collaboration.

I am grateful to my thesis committee members Dr. Ryszard Stroynowski, Dr. Matthew Klein, and Dr. Haleh K. Hadavand for their time and constructive feedback on my dissertation. Their insights have been instrumental in shaping this work. I also sincerely acknowledge Dr. Hadavand for providing early mentorship and support during my undergraduate research journey, which laid a strong foundation for my graduate studies.

Finally, I would like to thank my family and friends for their unwavering support and encouragement throughout my academic journey. Your belief in me has been a constant source of strength and motivation.

Bataju, Susan B.S., Physics, University of Texas at Arlington

Search for Higgs Boson Pair Production in the two light Leptons and one Tau Final State Using Proton-Proton Collision Data with $\sqrt{s} = 13$ TeV at the LHC from the ATLAS Detector

Advisor: Dr. Allison Deiana
Doctor of Philosophy degree conferred August 5, 2025
Dissertation completed July 1, 2025

In this thesis, a search is presented for the pair production of Higgs bosons in a final state containing two same-charge light leptons (e/μ) and one opposite-charge hadronically decaying tau lepton (τ_h). The search is based on a data sample of proton-proton (pp) collisions at a center-of-mass energy $\sqrt{s} = 13$ TeV, collected by the ATLAS detector during Run 2 (2015-2018) of the Large Hadron Collider (LHC), corresponding to an integrated luminosity of 140 fb^{-1}. The Standard Model predicts that the Higgs potential has a non-zero expectation value leading to the spontaneous breaking of electroweak symmetry and when some fundamental particles (for example leptons, W and Z bosons) interact with the Higgs field they gain mass. The measurement of the Higgs boson self-interaction directly enables the study of Higgs potential. Furthermore, any deviation from the predicted Standard Model value will suggest the existence of new physics. The pair production of the Higgs boson is sensitive to the Higgs boson self-coupling, thus its study is critical for our understanding of particle physics.

TABLE OF CONTENTS

ACKNOWLEDGMENTS iii

LIST OF FIGURES ix

LIST OF TABLES xiv

CHAPTER

1 Introduction 1
  - 1.1. Overview of the Thesis 3
  - 1.2. The Standard Model 3
  - 1.3. Overview of the Theory 6
  - 1.4. The Electroweak Interaction 7
  - 1.5. Electroweak Spontaneous Symmetry Breaking 9
  - 1.6. Higgs Self-Coupling 12
  - 1.7. Higgs Boson physics at the LHC 12
  - 1.8. Di-Higgs Boson physics at the LHC 15
  - 1.9. Di-Higgs Boson Decay 18

2 Large Hadron Collider and the ATLAS Experiment 20
  - 2.1. Large Hadron Collider 20
  - 2.2. The ATLAS Detector 24
    - 2.2.1. The ATLAS Coordinate System 26
    - 2.2.2. Inner Detector 27
    - 2.2.3. The ATLAS Calorimeters 29
    - 2.2.4. The Muon Detectors 34

2.2.5. The Trigger and Data Acquisition System 35

3 Search for $HH \to multilepton$ 37

3.1. Object Reconstruction 37

3.1.1. Track Reconstruction 39

3.1.2. Primary vertices 40

3.1.3. Topological Clusters 40

3.1.4. Trigger 40

3.1.5. Leptons 41

3.1.6. Hadronically Decaying Taus 43

3.1.7. Jets 44

3.1.8. Missing Transverse Energy 45

3.1.9. Object Overlap Removal 45

3.2. Data and Simulated samples 46

3.2.1. Signal Samples 47

3.2.2. Background Samples 48

3.3. Event Selection 51

3.4. Multivariate Analysis Strategy 51

3.5. Signal Region 56

3.6. Background Modeling 59

3.6.1. Estimation of Heavy-Flavor Electrons Using a Fitting Function 62

3.6.1.1. HF Electron Reweighting Uncertainty 65

3.6.2. Diboson background estimation 66

3.6.3. HF background estimation 67

3.6.4. Template Fit Method 70

3.6.4.1. Template Fit Uncertainties 71
3.6.5. Fake τ_{had} Background Estimation 73
3.6.5.1. Event Selection 74
3.6.5.2. Fake Tau SF Method 76
3.6.5.3. Fake Tau Composition Systematics 78
3.6.5.4. Fake Tau Numerator Systematic 80
3.6.5.5. Closure test 81
3.7. Validation Region 83
3.8. Systematic Uncertainties 84
3.8.1. Experimental Uncertainties 84
3.8.2. Theoretical Uncertainties 86
3.9. Statistical Analysis 88
3.9.1. Profile Likelihood Ratio Test 89
3.9.2. Test statistic 90
3.9.3. p-values and the CL_s Method 91
3.9.4. Significance of Observed Excess 91
3.10. Results 92
4 Conclusion 99
BIBLIOGRAPHY 101

LIST OF FIGURES

Figure Page

1.1 Overview of all the known elementary particles according to the SM. 4

1.2 The coupling of the Higgs boson to fermions and bosons as a function of the particle's mass. [16] 5

1.3 Leading order Feynman diagrams for the dominant production modes of Higgs boson. 13

1.4 Examples of one-loop dependent single Higgs diagrams for the Higgs boson self-energy, and for single Higgs production in different modes [23]. 14

1.5 Variation of the cross-sections (a) and branching fractions (b) as a function of the κ_λ for single Higgs production [23]. 15

1.6 Example of leading-order Feynman diagrams for gluon-gluon fusion HH production, via (a) the top-quark box, and (b) the self-interaction 'triangle' modes. 16

1.7 Leading-order diagrams for VBF HH production containing (a) the HHVV vertex, (b) the trilinear HHH vertex, and (c) via the VVHH production mode. 17

1.8 Variation of the cross-sections as a function of κ_λ for single and Higgs pair production [39]. 17

1.9 Predicted total cross section at the LO and NLO in QCD for HH production channels as a function of κ_λ. The dashed (solid) lines and light (dark) color bands correspond to the LO (NLO) results and to the scale and PDF uncertainties added linearly [40]. 18

1.10 Branching ratio for the decay of di-Higgs boson system [54]. 19

1.11 Observed and expected 95% CL upper limits on the signal strength for inclusive ggF HH and VBF HH production from the $HH \rightarrow b\bar{b}b\bar{b}$, $HH \rightarrow b\bar{b}\tau^+\tau^-$, $HH \rightarrow b\bar{b}\gamma\gamma$, multi-lepton, and $HH \rightarrow b\bar{b} + E_T^{miss}$ decay channels and their statistical combination. The predicted SM cross section assumes $m_H = 125$ GeV. The expected limit, along with its associated $\pm 1\sigma$ and $\pm 2\sigma$ bands, is calculated for the assumption of no HH production and with all NPs profiled to the observed data [46]. 19

2.1 LHC delivered luminosity for the high luminosity experiments to ATLAS and CMS. [58] 22

2.2 A schematic diagram of the CERN accelerator complex with various interaction points [68]. 24

2.3 Geometry of magnet windings and tile calorimeter steel. The eight barrel toroid coils, with the end-cap coils interleaved are visible. The solenoid winding lies inside the calorimeter volume. The tile calorimeter is modeled by four layers with different magnetic properties. [67] 25

2.4 A schematic view of the ATLAS detector. 26

2.5 Plan view of a quarter-section of the ATLAS inner detector showing each of the major detector elements with its active dimensions and envelopes [67]. 27

2.6 Cut-away view of the ATLAS calorimeter system [67]. 30

2.7 Sketch of a barrel module where the different layers are visible. The granularity in η and ϕ of the cells of each of the three layers are also shown. [67] 33

2.8 Schematic of the Tile Calorimeter [67]. 33

2.9 Cut-away view of the ATLAS muon system. [67] 35

2.10 Schematic layout of the ATLAS TDAQ system in Run 2 [77]. 36

3.1 The distributions of variables used for MVA training for the signal region. The signal has been normalized to the total background. Systematic errors are not included. 53

3.2 Signal (blue) and background (red) distributions of 13 input variables used in the BDT training of $2lSC1\tau_{had}$ channel. 54

3.3 Correlation coefficients between the 13 BDT input variables for signal (left) and background (right) of $2lSC1\tau_{had}$ channel. 55

3.4 Number of different trials vs AUC value for the trial. 55

3.5 The BDT with Gradient Boost distribution for the signal and background obtained during the training and testing of $2lSC1\tau_{had}$ channel. 57

3.6 The background rejection versus signal efficiency for BDT of $2lSC1\tau_{had}$ channel. 57

3.7 BDT output score distribution for fold 0. 57

3.8 The distributions of BDTG score (left) and the number of jets (right) in the SR. The signal has been normalized to the total background. Systematic errors are not included. 58

3.9 Types of fake backgrounds in the $2lSC1\tau_{\text{had}}$ channel. In the bin labels, 'T' denotes a prompt lepton, 'F' a fake lepton, and 't', 'l0', 'l1' correspond to the hadronic tau, leading lepton, and subleading lepton, respectively. The category 'otherVV' includes all diboson processes except $WZ \to ll l\nu$, such as WZ with other decay modes, ZZ, WW, and $VVjj$. Panel (b) shows the same data as (a) but with a logarithmic scale on the Y-axis. 61

3.10 BDT output score distribution for the HF-e control region. The HH signal distribution is scaled to match the total background, and the expected HH yield is indicated in the legend. 63

3.11 HF-e BDT Distributions in the 2ℓSS$1\tau_{\text{had}}$ Channel 64

3.12 The pre-fit signal region distribution after reweighing HF electron samples using a liner fit from the ratio of HF electron in signal region to the control region. 65

3.13 Systematic variations in the reweighted HF-e distribution in the signal region due to $\pm 1\sigma$ variations in the fit parameters. 66

3.14 Origins for the leading and sub-leading fake leptons in same-sign dilepton channels: $e^{\pm}e^{\pm}$ (top), $e^{\pm}\mu^{\pm}$ (middle), and $\mu^{\pm}\mu^{\pm}$ (bottom). The definition of particle origin is as follows: Not defined = 0, Photon conversion = 5, Dalitz = 6, top = 10, W boson = 12, Z boson = 13, Higgs = 14, Charmed meson = 25, Bottom meson = 26, Bottom baryon = 33, Kaon decay = 35, Diboson = 43, Z or heavy boson = 44. The HH signal distribution is scaled to the total background events and the expected HH yield is quoted in the legend. 69

3.15 Pre-fit distributions in the template fit control regions. Top left: VV CR. Top right and bottom: HF-e and HF-μ control regions. 71

3.16 The OS light leptons Control Samples with removing isolation criteria: ΔR_{ll} in $\mu e + ee$ channel (left),HT_{lep} in $\mu e + ee$ channel (center) and HT_{lep} in $e\mu + \mu\mu$ channel (right). A part of systematic errors are included. 73

3.17 MCTruthClassifier type of tau in nominal scale factor CR. Bins: 0: unknown, 1-8: light leptons, 9-12: tau, 13-16: photon, 17-38: hadron, nentrino and other BSM particles. As seen in bin0, most of the Vjets faking tau samples lost its truth information. 74

3.18 Truth jet flavor composition of fake tau in nominal CR. Bins: -1: unknown, 1-3: light, 4: c, 5: b, 6: t, 21: gluon. 75

3.19 τ_{had} p_{T} distribution in nominal fake tau scale factor CR for (a) 1-prong and (b) 3-prong tau. 77

3.20 Nominal fake tau scale factors for (a) 1-prong and (b) 3-prong tau. 77

3.21 Fake tau scale factors for (a) 1-prong and (b) 3-prong tau. Uncertainty band combines all SF systematic sources. 79

3.22 Truth jet flavor composition of fake tau in alternative Zjets and $t\bar{t}$ CRs. Bins: -1: unknown, 1-3: light, 4: c, 5: b, 6: t, 21: gluon. 79

3.23 Fake tau scale factors with difference in alternative CRs as composition systematic for (a) 1-prong and (b) 3-prong tau. 80

3.24 Fake tau scale factors with true tau MC subtraction systematic for (a) 1-prong and (b) 3-prong tau. 81

3.25 Showing closer test by applying the nominal SF back to nominal CR shown in (a) τ_{had} p_{T}, (b) leading lepton p_{T}, (c) leading lepton η, (d) leading jet p_{T}, (e) jet multiplicity. Uncertainty band includes SF systematics. 82

3.26 Distributions of the BDT output score in the validation region for $2\ell\mathrm{SC}1\tau_{\mathrm{had}}$ channel showing pre-fit (left) and post-fit (right). The non-prompt distribution is reweighted using a linear fit, see Section 3.6.1. The total pre-fit background (and its ratio to data) is also shown, as is the SM HH signal scaled up by a factor of 100. The uncertainty bands include all sources of statistical and systematic uncertainties in the background prediction. 83

3.27 Distributions of the BDT output score in the signal region for $2\ell\mathrm{SC}1\tau_{\mathrm{had}}$ channel before (left) and after (right) background fit. The non-prompt distribution is reweighted using a linear fit, see Section 3.6.1. The total pre-fit background (and its ratio to data) is also shown, as is the SM HH signal scaled up by a factor of 100. The uncertainty bands include all sources of statistical and systematic uncertainties in the background prediction. 93

3.28 Pulls and constraints of nuisance parameters. 94

3.29 Impact of nuisance parameters on the signal strength in the signal region. 95

3.30 Fitted normalization factors for template components, including signal strength. The signal strength of non-resonant SM HH production is defined as the ratio of the signal cross-section to the SM prediction. 95

3.31 Post-fit distributions in the template fit control regions. Top left: VV CR. Top right and bottom: HF-e and HF-μ control regions. 96

3.32 (a) Pre-fit and (b) post-fit yield summary in signal and control regions. 97

3.33 Expected (dashed line) and observed (solid line) likelihood-ratio scans as a function of κ_λ (left) and κ_{2V} (right) for the 2ℓSS+1τ channel. The intersection of the solid curves and the horizontal dashed lines indicate the 68% and 95% confidence intervals. 98

4.1 Observed (filled circles) and expected (open circles) 95% CL upper limits on the signal strength for HH production in the background-only (μHH $= 0$) hypothesis. The dashed lines indicate the expected 95% CL upper limits on μHH in the SM hypothesis (μHH $= 1$). The inner and outer bands indicate the $\pm1\sigma$ and $\pm2\sigma$ variations on the expected limit under the background-only hypothesis due to statistical and systematic uncertainties, respectively. Results are shown individually for the different search channels, the statistical combination of ML and $\gamma\gamma$+ML channels separately, and the statistical combination of all channels [14]. 100

LIST OF TABLES

Table Page

2.1 Summary of beam and machine parameters during Run 2. [58] 21

2.2 Main parameters of the muon spectrometer [67]. 34

3.1 List of lowest p_T-threshold, un-prescaled single lepton and dilepton triggers used for 2015–2018 data taking. 42

3.2 The definition of the light leptons used in the analysis. 43

3.3 The definition of τ_{had} candidates used in the analysis. 44

3.4 The configurations are used for event generation of signal and background processes, with the samples used to estimate the systematic uncertainties enclosed in parentheses. 50

3.5 Summary of event selection. 51

3.6 Variables used in the multivariate analysis for $2lSC1\tau_{had}$ channel. 52

3.7 Event yields from pre-fit plots for all the MC samples in 2ℓSS$1\tau_{\text{had}}$ signal region. The uncertainties are only statistical. 59

3.8 Correlation and Covariance Matrices for Parameters m and c 65

3.9 Eigenvalues and Eigenvectors of the Covariance Matrix for Parameters m and c 66

3.10 Event yields for VV samples in $2lSC1\tau_{\text{had}}$ control region.The rest of the VV subprocesses are not participating in the VV background. The uncertainties are only statistical. 67

3.11 Values of template fit uncertainties in the 2ℓSC$1\tau_{\text{had}}$ channel. 73

3.13 The background sample normalizations and their uncertainties used in the analysis. 88

3.14 Expected and observed 95% CL exclusion limit on the signal strength in $2lSC1\tau_{had}$ final state. 97

To my parents, grandparents, and friends, for your unconditional love, support, and belief in me.

CHAPTER 1

Introduction

Since time immemorial, humans have been curious about their existence and pondered the mysteries of the universe: What are we and the universe made of? How does our universe work? These age-old questions, coupled with our innate curiosity, have driven the quest for knowledge and guided humanity from ancient philosophy to modern science. Ancient philosophers, such as the Greek scholars Democritus and Leucippus, as well as ancient Indian thinkers, proposed that the physical universe is composed of fundamental, indivisible components known as atoms, derived from the Greek word atomon, meaning "uncuttable" or "indivisible". This theory is known as Atomism.

The modern concept of the atom begins with the work of John Dalton in the early 19th century. Dalton developed a scientific model of atomic theory based on empirical experimental data [1]. By the late 19th century, J.J. Thomson discovered the first subatomic particle, the electron, expanding upon Dalton's atomic theory and demonstrating that the atom was not a simple, indivisible entity but rather made up of smaller, subatomic particles [2]. In 1911, Ernest Rutherford, through his gold foil experiment, revealed the existence of the atomic nucleus, showing that most of the atom's mass is concentrated in a dense core, surrounded by electrons [3]. These discoveries and many others laid the foundation for modern atomic and subatomic physics. Also, in the 19th century, as atomic particles were being discovered, James Clerk Maxwell developed his classical theory of electromagnetic radiation [4]. Maxwell's work was the first theoretical framework to unify the phenomena of electricity, magnetism, and light, all of which are manifestations of electromagnetic radiation. His theory introduced the concept of fields as fundamental entities, inspiring future physicists to extend it to other forces of nature.

By the latter half of the 20th century, the basic structure of the atom was well understood, and the discovery of the proton and neutron (collectively called hadrons) had provided a clear picture of the atomic nucleus. However, a crucial question remained: Are protons and neutrons themselves fundamental particles, or are they composed of even smaller constituents? This question became the focus of a new wave of research in particle physics. In 1964, Murray Gell-Mann [5] and George Zweig [6] independently proposed the quark model, suggesting that protons, neutrons, and other hadrons were not elementary, but rather composed of more fundamental particles called quarks.

In the 1970s, the work of Glashow [7], Weinberg [8], and Salam [9] formulated the electroweak theory, which unified two of the four fundamental forces, electromagnetic and weak forces, into a single theoretical framework. Their theory predicted the existence of the W± and Z bosons, the force carriers for the weak interaction, and made key predictions about their masses. These predictions were experimentally confirmed at CERN in 1983 [10], providing strong evidence for the validity of the electroweak theory. Their work has been known as the Standard Model (SM) of particle physics, which successfully unifies the electromagnetic and weak forces. The SM has since become the cornerstone of modern particle physics, successfully explaining the behavior of matter and forces in the universe. The validity of SM has been further cemented after the landmark discovery of the top quark in 1995 from the Collider Detector at Fermilab (CDF) [11] and the Higgs boson in 2012 from ATLAS and CMS Collaborations [12, 13]. However, the SM remains an incomplete theory. Many unanswered questions remain, such as the origin of the matter-antimatter asymmetry, the reason for neutrino masses, the unification of the fundamental forces (including incorporating gravity), and the nature of the dark matter.

1.1. Overview of the Thesis

Chapter 1 provides an introduction and the underlying theoretical framework needed in this dissertation. The chapter includes an overview of the SM, a brief description of the spontaneous symmetry-breaking mechanism, the Higgs field, and the Higgs self-coupling. Chapter 2 describes the experimental apparatus used to record the data used in this thesis, namely the Large Hadron Collider and the ATLAS experiment. Chapter 3 is devoted to the search for the Higgs boson pair production with a final state containing two same-charge light leptons (e/μ) and one opposite-charge hadronically decaying tau lepton (τ_{had}). This chapter describes in detail the simulated sample that is used, the composition of the background, object, and event selections, and the background estimation. This chapter also describes the uncertainties present in the analysis and, finally, the results that are obtained. The analysis described in the thesis is part of the larger Higgs boson pair production to multi-lepton search [14]. After joining the analysis team, I worked on continuous updates to the object and event selection and the harmonization with other channels in the larger multi-lepton search. I worked on developing the variables and the Boosted Decision Tree (BDT) and tested other classification techniques, like XGBoost [15] and Deep Neural Networks, for the multivariate analysis. I also worked to develop the background estimation used in the analysis and the uncertainties present in the analysis, excluding the τ_{had} background estimation. Finally, I also ran the statistical fits for the results.

1.2. The Standard Model

The Standard Model of particle physics is a theory based on the principles of quantum mechanics and relativity. The SM is formulated using Lorentz invariant Lagrangians, ensuring that its equations hold true in any inertial reference frame. Furthermore, SM treats particles as quantum excitations of underlying fields that permeate space and time. The lowest energy states of these fields are known as the vacuum states, and the excitation of these fields occurs in discrete amounts. All elementary particles are grouped as matter particles (fermions) or force carriers (bosons). An overview of all the elementary particles is shown in Figure 1.1. Bosons have integral spin, obey the Bose-Einstein statistics, and do not follow

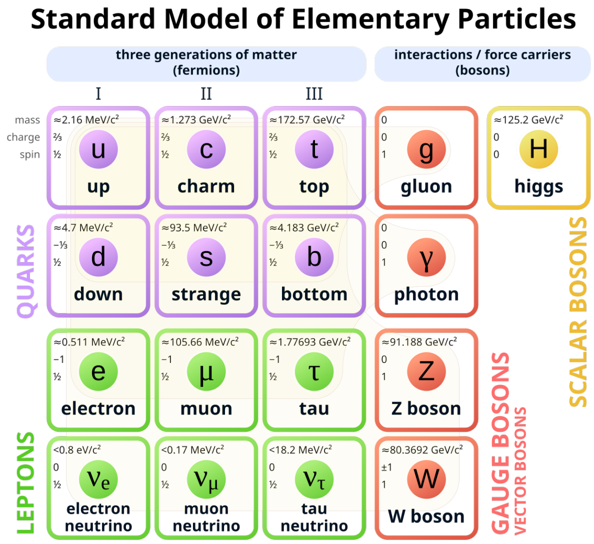

Figure 1.1: Overview of all the known elementary particles according to the SM.

the Pauli exclusion principle. Bosons also have symmetric wave functions, and thus more than one boson can occupy the same quantum state. Bosons with a spin equal to one are also gauge bosons, the force carriers of fundamental forces. The electromagnetic force between two electrons is mediated by an exchange of photons. Here, the photons are the force carriers of electromagnetic interaction. Similarly, W± and Z bosons are responsible for the weak force, and gluons are responsible for the strong force. The Higgs boson is the only particle to have zero spin in the SM, and it is associated with the Higgs field. The Higgs field permeates space, and particles interact with the Higgs field by the exchange of the Higgs boson. Furthermore, fundamental particles acquire mass through the Higgs mechanism when they interact with the Higgs field. The Higgs field is constant throughout the universe, leading to the same mass contribution, but particles interact with Higgs bosons at different strengths, as shown in Figure 1.2. The photons and gluons do not interact directly with the Higgs field, so they are massless. The origin of the mass of the neutrino is not explained by the SM interactions. Fermions have half-integer spin, obey the Fermi-Dirac statistics, and follow the

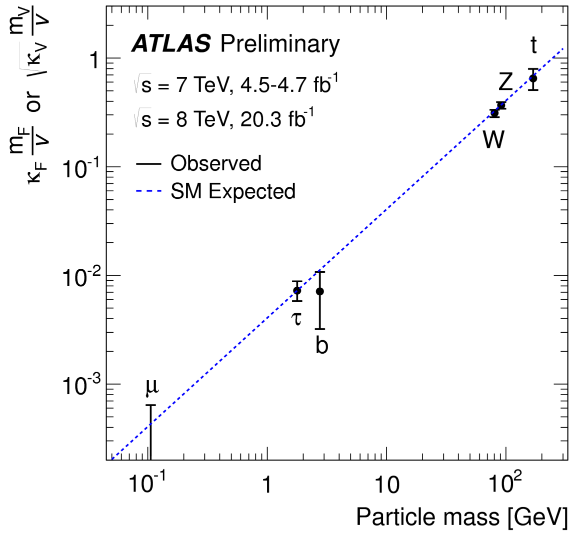

Figure 1.2: The coupling of the Higgs boson to fermions and bosons as a function of the particle's mass. [16]

Pauli exclusion principle. Fermions also have anti-symmetric wave functions, and no more than one fermion can occupy one quantum state. Fermions are arranged in three generations, where each successive generation is heavier than the last, and the only difference between the generations is their mass. Fermions are further classified into two groups based on their interaction with the strong force: quarks and leptons. Fermions that interact through the strong force are called quarks and thus carry a color charge. Quarks can also interact through electromagnetic and weak forces. There are six flavors of quarks seen in nature, which are up, down, charm, strange, bottom, and top quarks. The u, c, and t flavors of quarks have an electric charge of +2/3, and the d, s, and b flavors of quarks have an electric charge of -1/3. Quarks are always paired with other quarks, as it is energetically more favorable to create new quarks than it is to overcome the strong force binding them together. However, leptons have an integral electric charge and no color charge. Electron, muon, and tau leptons have a charge of -1, and their neutrino counterparts have zero electric charge. Charged leptons can interact through electromagnetic and weak forces, but neutral leptons interact via weak force only. In addition to the fundamental particles discussed so far, there are antiparticle counterparts with an opposite electric charge, but all other quantum mechanical properties are the same. The neutral particles, for example, photons, Z bosons, Higgs bosons, and so on, are their own antiparticles. However, it is currently unknown whether the lepton neutrino and lepton antineutrino are the same particle.

1.3. Overview of the Theory

The SM is a non-Abelian gauge theory, where the Lagrangians are invariant under local gauge transformation and thus gauge invariant. These transformations are classified into symmetric groups, which are non-commutative. From Noether's theorem, the symmetric groups represent important conservation laws in the SM, for example, electric charge, color charge, lepton number, etc. The symmetry group for the SM is given as follows:

$$SU(3)_C \times SU(2)_L \times U(1)_Y \tag{1.1}$$

$SU(3)_C$ is the color gauge symmetry responsible for the strong force and color charge. This subgroup has eight generators, which are represented by the Gell-Mann matrices. $SU(2)_L$ corresponds to the weak isospin symmetry, which governs the weak interactions with three generators. It acts on the left-handed components of the fermion fields. $U(1)_Y$ represents the hypercharge symmetry and is abelian in nature with only one generator. The general idea is that gauge bosons and fermions are massless to begin with; the Lagrangians only have massless terms. A scalar field (the Higgs field) is then introduced with a non-vanishing vacuum-expectation value. The resulting spontaneous breakdown of symmetry gives masses to the fermions and the gauge bosons, but not to the photon and neutrino. A more detailed explanation can be found in ref. [17, Chapter 8]. Additionally, Sections 1.4 and 1.5 are inspired by [17, Chapter 8] as well.

1.4. The Electroweak Interaction

Fermions in the SM are represented as spinor fields. They are arranged as “isospin” doublets since the transformation under $SU(2)_L \times U(1)_Y$ must be between particles whose space-time properties are the same. The weak isospin doublets for leptons are as follows:

$$\begin{pmatrix} \nu_e \\ \\ e_L \end{pmatrix} \quad \begin{pmatrix} \nu_\mu \\ \\ \mu_L \end{pmatrix} \quad \begin{pmatrix} \nu_\tau \\ \\ \tau_L \end{pmatrix}$$

and quarks are given as

$$\begin{pmatrix} u \\ \\ d' \end{pmatrix} \quad \begin{pmatrix} c \\ \\ s' \end{pmatrix} \quad \begin{pmatrix} t \\ \\ b' \end{pmatrix}$$

Here, the states d', s', and b' are linear combinations of d, s, and b quarks; the flavor mixing is given by the Kobayashi-Maskawa Matrix (CKM-Matrix) [18, 19], while the lepton flavor is conserved in SM. Neutrino flavor oscillation is observed in nature but not explained by any SM interactions [20, 21]. All the doublets are assigned a non-Abelian charge $I_W = \frac{1}{2}$ (weak isospin). The remaining right-handed components are singlet states with $I_W = 0$, and according to the 2-component neutrino theory, the lepton neutrino has left-handed components only [22].

If L is taken as the left-handed electron-neutrino doublet and R as the right-handed electron singlet state. Under $SU(2)_L$ transformation, L transforms as a rotation in weak isospin space, whereas R is unchanged, as shown in Equation 1.2.

$$\begin{aligned} &L \rightarrow exp(-\frac{i}{2} g\tau \cdot \theta(x))L \\ &R \rightarrow R \end{aligned} \tag{1.2}$$

Here, g is a coupling constant, τ are the Pauli matrices, and $\theta(x)$ is a local phase transformation. The relation between electric charge Q and the third component of isospin I^3_W is as follows:

$$\begin{aligned} L :& Q = I^3_W - \frac{1}{2} \\ R :& Q = I^3_W - 1 \end{aligned} \tag{1.3}$$

The $U(1)_Y$ gauge symmetry acts by multiplying the field by a phase factor. For a fermion field, hypercharge (Y) is conserved under $U(1)_Y$ transformation. The hypercharge is given by the Gell-Mann-Nishijima relation shown in Equation 1.4.

$$Q = I^3_W + \frac{Y}{2} \tag{1.4}$$

Comparing with Equation 1.3, L has $Y = -1$ and R has $Y = -2$. Then, under $U(1)_Y$ transformation, the lepton transforms as shown in Equation 1.5.

$$\psi \rightarrow exp(i\alpha Y)\psi \tag{1.5}$$

Where α is a parameter of transformation. Finally, gauging $SU(2)_L$ means introducing three gauge potentials, $W^i\mu$, and the covariant derivative is given as follows:

$$D_\mu L = \partial_\mu L - \frac{i}{2} g\tau \cdot W_\mu L \tag{1.6}$$

Here g is the $SU(2)$ coupling constant and g' the coupling constant for $U(1)_Y$. Gauging $U(1)_Y$ means introducing another potential, X_μ, and then the covariant derivatives are as follows:

$$\begin{aligned} D_\mu L &= \partial_\mu L + \frac{i}{2} g' X_\mu L \\ D_\mu R &= \partial_\mu R + \frac{i}{2} g' X_\mu R \end{aligned} \tag{1.7}$$

Then, the SM Lagrangian for a lepton with the gauge field terms is given by

$$\begin{aligned}\mathcal{L} = i\bar{R}\gamma^\mu(\partial_\mu + \frac{i}{2}g'X_\mu)R + i\bar{L}\gamma^\mu(\partial_\mu + \frac{i}{2}g'X_\mu - \frac{i}{2}g\tau\cdot W_\mu)L \\ -\frac{1}{4}(\partial_\mu W_\nu - \partial_\nu W_\mu + gW_\mu \times W_\nu)^2 - \frac{1}{4}(\partial_\mu X_\nu - \partial_\nu X_\mu)^2\end{aligned} \tag{1.8}$$

1.5. Electroweak Spontaneous Symmetry Breaking

The Higgs field is introduced in the SM as a weak isospin doublet scalar field with the quantum number $I_W = \frac{1}{2}$ and $Y = 1$

$$\phi = \begin{pmatrix} \phi^+ \\ \\ \phi^0 \end{pmatrix} = \frac{1}{\sqrt{2}}\begin{pmatrix} \phi_3 + i\phi_4 \\ \\ \phi_1 + i\phi_2 \end{pmatrix} \tag{1.9}$$

so that both ϕ^+ and ϕ^0 are complex fields and $\phi_1, ..., \phi_4$ are real fields, and the covariant derivative is given as follows:

$$D_\mu\phi = (\partial_\mu - \frac{i}{2}g\tau\cdot W_\mu - \frac{i}{2}g'X_\mu)\phi \tag{1.10}$$

Now, the overall Lagrangian containing the Higgs fields is given by Equation 1.11. The interaction of the Higgs field with e^- and ν_e is written fully in Equation 1.12 where the interaction strength between the Higgs field with e^- and ν_e is given by G_e.

$$\mathcal{L} = (D_\mu\phi)^\dagger(D_\mu\phi) - V(\phi) - G_e(\bar{L}\phi R + \bar{R}\phi^\dagger L) \tag{1.11}$$

$$G_e(\bar{L}\phi R + \bar{R}\phi^\dagger L) = G_e(\bar{\nu_e} e_R \phi^\dagger + \bar{e_L} e_R \phi^0 + \bar{e_R} \nu_e \phi^- + \bar{e_R} e_L \bar{\phi^0}) \tag{1.12}$$

Here, the Higgs potential is given in Equation 1.13 where we assume $\lambda > 0$ to keep the potential bounded from below.

$$V(\phi) = \frac{m^2}{2}\phi^\dagger\phi + \frac{\lambda}{4}(\phi^\dagger\phi)^2 \tag{1.13}$$

The ground state is obtained by minimizing the potential as given in Equation 1.14.

$$\frac{\partial V(\phi)}{\partial\phi} = \phi(\frac{m^2}{2} + \frac{\lambda}{2}\phi^\dagger\phi) \tag{1.14}$$

There are two solutions: when $m^2 > 0$, $\phi = 0$ the only solution is the trivial ground state, where the vacuum expectation value would be zero, but when $m^2 < 0$ the ground state is given by Equation 1.15 with a non-zero vacuum expectation value.

$$(\phi^\dagger\phi)_0 = -\frac{m^2}{\lambda} \tag{1.15}$$

Now, we are free to choose the gauge in any isospin frame, so, fixing the Higgs field with the gauge given in Equation 1.16, the ground state Higgs fields are given by Equation 1.17 where η is real. With the Higgs field written as Equation 1.17, we now have a degenerate vacuum and spontaneous breaking of the gauge symmetry. Since there is local symmetry, we can perform independent gauge transformations at each point in space-time. Therefore, we can select the unitary gauge so that every point in space-time ϕ lies along the neutral component. With this chosen gauge, the Higgs field can be represented as shown in Equation 1.18 where, $\sigma(x)$ represents the Higgs field linked to a new massive particle, the Higgs boson, and $\sqrt{2}\cdot\eta$ is also known as the vacuum expectation value. The non-zero vacuum expectation value of the Higgs field is around 246 GeV.

$$\begin{gathered}(\phi_1^2)_0 = -\frac{2m^2}{\lambda}, \quad (\phi_2^2)_0 = 0 = (\phi_3^2)_0 = (\phi_4^2)_0 = 0 \\ \sqrt{2}\eta \equiv \sqrt{\frac{-2m^2}{\lambda}}\end{gathered} \tag{1.16}$$

$$(\phi_0) = \begin{pmatrix} 0 \\ \\ \eta \end{pmatrix} \tag{1.17}$$

$$\phi(x) = \begin{pmatrix} 0 \\ \\ \eta + \frac{\sigma(x)}{\sqrt{2}} \end{pmatrix} \tag{1.18}$$

Then from Equation 1.11 and Equation 1.18 we get the following:

$$\begin{aligned} (D_\mu\phi)^\dagger(D_\mu\phi) = \frac{1}{2}(\partial\sigma)^2 + \frac{g^2\eta^2}{4}[(W_\mu^1)^2 + (W_\mu^2)^2] \\ + \frac{\eta^2}{4}(gW_\mu^3 - g'X_\mu)^2 + \text{cubic } + \text{quartic terms} \end{aligned} \tag{1.19}$$

We can then define the following:

$$Z_\mu = \frac{gW_\mu^3 - g'X_\mu}{\sqrt{g^2 + g'^2}} \equiv \cos\theta_W W_\mu^3 - \sin\theta_W X_\mu \tag{1.20}$$

and the orthogonal field to Z_μ as

$$A_\mu = \frac{g'W_\mu^3 + gX_\mu}{\sqrt{g^2 + g'^2}} \equiv \sin\theta_W W_\mu^3 + \cos\theta_W X_\mu \tag{1.21}$$

where θ_W is the 'Weinberg angle' given by

$$\cos\theta_W = \frac{g}{\sqrt{g^2 + g'^2}}, \quad \tan\theta_W = \frac{g'}{g} \tag{1.22}$$

From Equation 1.19, W_μ^1,W_μ^2 and Z_μ pick up masses as shown in Equation 1.23 but A_μ (the photon) remains massless. The first two components in the W_μ fields are mixed to create two charge bosons $W^\pm$ by a simple basis transformation of the $SU(2)_L$ basis as $W_\mu^\pm = (W_\mu^1 \mp iW_\mu^2)/\sqrt{2}$.

$$M_{W1}^2 = M_{W2}^2 = \frac{g^2\eta^2}{2}, \quad M_Z^2 = \frac{M_w^2}{\cos^2\theta_W} \tag{1.23}$$

1.6. Higgs Self-Coupling

Now, taking the Higgs potential in Equation 1.13 and defining vacuum expectation value as $v = \sqrt{2}\eta$ in Equation 1.18, the Higgs potential can be defined in terms of v using the unitary gauge as follows:

$$V(h) = \lambda v^2 h^2 + \lambda v h^3 + \frac{1}{4}\lambda h^4 + \text{higher order terms} \tag{1.24}$$

Here, the first term is related to the mass of the Higgs boson, $m_H = \sqrt{2\lambda v^2}$, the second term corresponds to the trilinear coupling constant, while the third term is the Higgs quartic coupling constant. The SM Higgs self-coupling, or the trilinear coupling constant at the ground state, is expected to be as follows:

$$\lambda_{SM} = \frac{m_H^2}{2v^2} = 0.129 \tag{1.25}$$

Then, the ratio of the measured Higgs trilinear coupling constant to its expected SM value can be defined as κ_λ,

$$\kappa_\lambda = \frac{\lambda}{\lambda_{SM}} \tag{1.26}$$

Where λ is the experimentally determined Higgs trilinear coupling constant and λ_{SM} is the SM predicted Higgs trilinear coupling constant. Thus, any potential deviations from unity in κ_λ would indicate new physics beyond the SM. κ_λ can be measured experimentally using the production cross-section of HH and single Higgs decays. Furthermore, measuring κ_λ is an important test for the electroweak symmetry breaking and also to measure the shape of the Higgs potential.

1.7. Higgs Boson physics at the LHC

At the LHC for Run 2, proton-proton beams are collided at high energy ($\sqrt{s} = 13$ TeV). At such high energy, gluons carry most of the proton's momentum, which makes gluon-gluon initiated decay the most prevalent for the Higgs decay mode at the LHC. The gluon-gluon fusion (ggF) process accounts for 87% of all the Higgs production at LHC. The ggF process is mediated by a top-quark loop. The next dominant process at LHC is vector-boson fusion (VBF) which accounts for 6.8% of all the Higgs boson events. In VBF, two high-energy protons collide such that the quarks emit a virtual vector boson, which interacts with another vector boson to produce a Higgs boson. The initial quarks continue to travel forward, producing two high-energy forward jets. The other two modes seen at LHC are Higgs-strahlung associated with W or Z boson (VH) production and the associated production with a pair of top quarks ($t\bar{t}H$). The leading order Feynman diagram for all four production modes is shown inFigure 1.3. The Higgs boson can interact with massive and

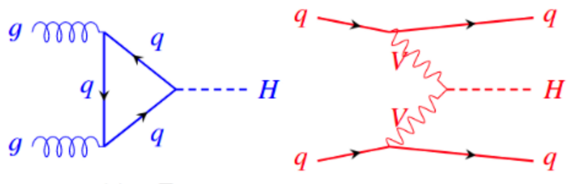

(a) ggF

(b) VBF

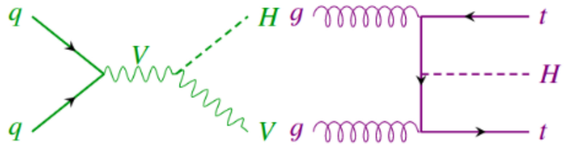

(c) VH

(d) ttH

Figure 1.3: Leading order Feynman diagrams for the dominant production modes of Higgs boson.

massless particles. The Higgs boson can decay into massless particles like photons, which involves virtual loops of heavy particles. Due to the brief lifespan of the Higgs boson, it can't be observed directly, but its decay products are studied. The decay products we can directly observe are electrons, muons, various jets, and photons, and using these final state particles, it is possible to detect the Higgs boson. The interaction strength for various particles with the Higgs boson is given in Figure 1.2.

While the Higgs boson self-coupling has been explored using the single Higgs boson production, such constraints become significantly weaker in new physics scenarios where simultaneous modifications to the single Higgs boson couplings are allowed [23]. The single Higgs boson production does not provide significant information about the Higgs self-coupling at the leading order (LO), but only in the next-to-leading order (NLO), as depicted by the Feynman diagrams in Figure 1.4. The dependence on the trilinear coupling modifier, κ_λ (Section 1.6), of the Higgs boson production cross sections and the decay branching fractions are shown in Figure 1.5.

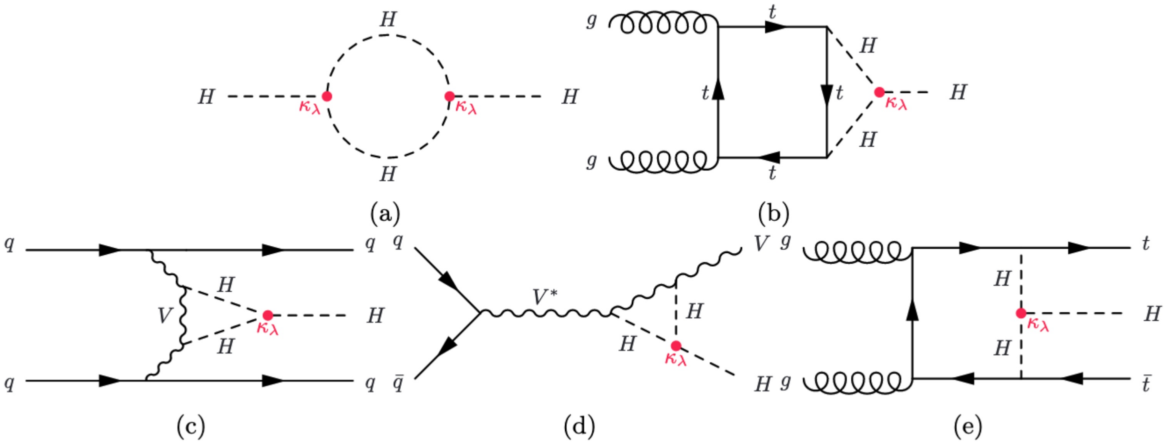

(a) (b)

(c) (d) (e)

Figure 1.4: Examples of one-loop dependent single Higgs diagrams for the Higgs boson self-energy, and for single Higgs production in different modes [23].

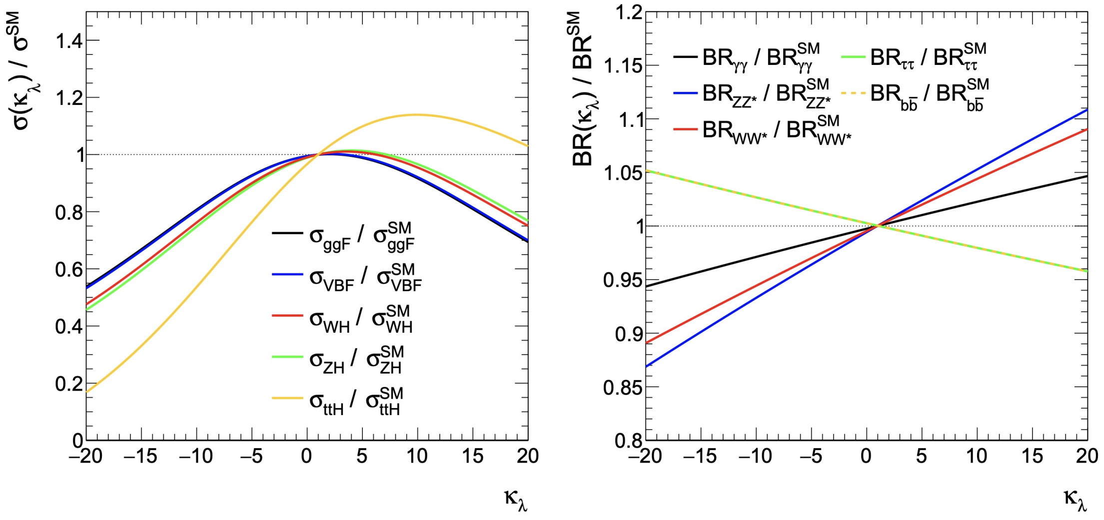

(a)

(b)

Figure 1.5: Variation of the cross-sections (a) and branching fractions (b) as a function of the κ_λ for single Higgs production [23].

1.8. Di-Higgs Boson physics at the LHC

More substantial insights can be gained by examining the production of Higgs boson pairs, as this process directly depends on the Higgs self-coupling. Compared to single Higgs production, the pair production of the Higgs boson has a major effect on the Higgs cross-sections, branching ratios, and overall kinematics when modifying the κ_λ. The effect of κ_λ on the HH process can be seen in Figure 1.8; as compared to the single Higgs processes, the HH processes are affected dramatically more than single Higgs processes.

The leading production mode, about 90% of the HH production in the SM, is through the gluon-gluon fusion (ggF) at LHC. The ggF cross-section, for a Higgs boson mass of $m_H = 125$ GeV, calculated at next-to-next-to-leading order (NNLO) accuracy in the finite top-quark mass approximation, is $\sigma_{HH}(ggF) = 31.1^{+6.7\%}_{-23.2\%}$ fb [24–31]. The box and triangle Feynman diagrams for the ggF production of HH are shown in Figure 1.6. The two ggF production modes interfere destructively with each other in the SM [32]. The HHH vertex in the triangle diagram is sensitive to the Higgs self-coupling (κ_λ), while both diagrams are sensitive to the top-quark Yukawa coupling (κ_t). For this analysis, the value of κ_t is set to its SM value of 1. At the SM value of $\kappa_\lambda = 1$, the destructive interference between the box and triangle diagrams leads to a negligible HH production cross-section. However, as seen in Figures 1.8 and 1.9, the HH production cross-section rapidly increases as κ_λ deviates from the SM value of 1. The interference between the two ggF processes makes this highly sensitive to the κ_λ coupling.

The sub-leading production mode, about 5% of the HH production, is through the vector-boson fusion (VBF) and has a total cross-section of 1.73±2.1% fb, calculated at next-to-next-to-next-to-leading order (N^3LO) with $m_H = 125$ GeV [33–38]. The VBF production mode offers additional sensitivity to κ_λ while also being sensitive to the $VVHH$ coupling, where κ_{2V} denotes the coupling strength with respect to the SM prediction. The leading-order diagrams for the VBF production of HH are shown in Figure 1.7.

Other production modes, VVH, $ttHH$, and $tjHH$, have negligible contributions towards HH production at the LHC, have lower cross-sections, and thus are not considered in this analysis.

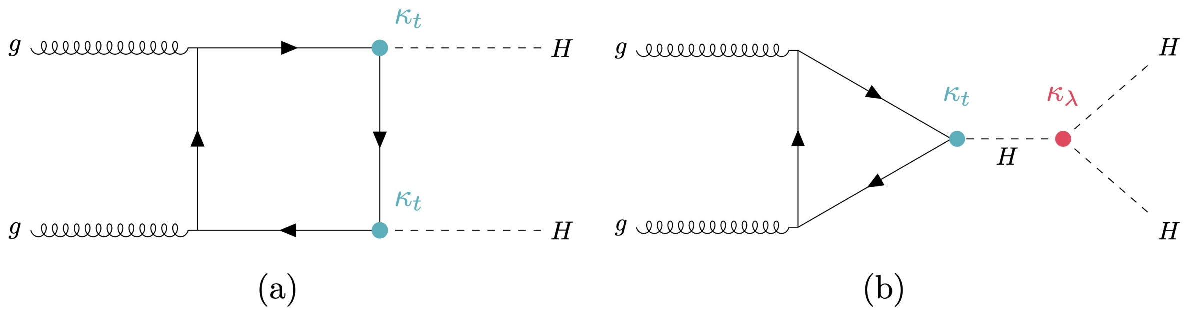

Figure 1.6: Example of leading-order Feynman diagrams for gluon-gluon fusion HH production, via (a) the top-quark box, and (b) the self-interaction ‘triangle’ modes.

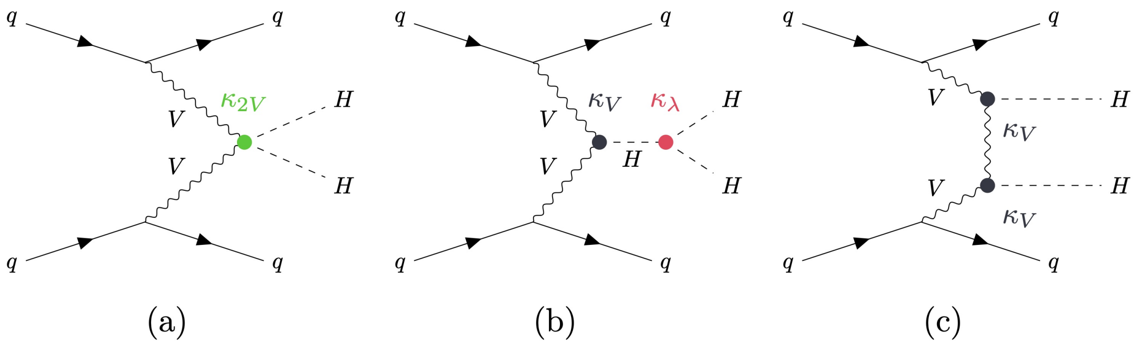

Figure 1.7: Leading-order diagrams for VBF HH production containing (a) the HHVV vertex, (b) the trilinear HHH vertex, and (c) via the VVHH production mode.

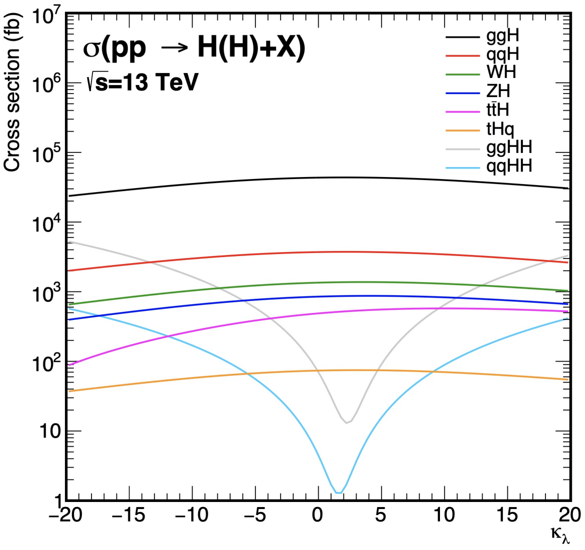

Figure 1.8: Variation of the cross-sections as a function of κ_λ for single and Higgs pair production [39].

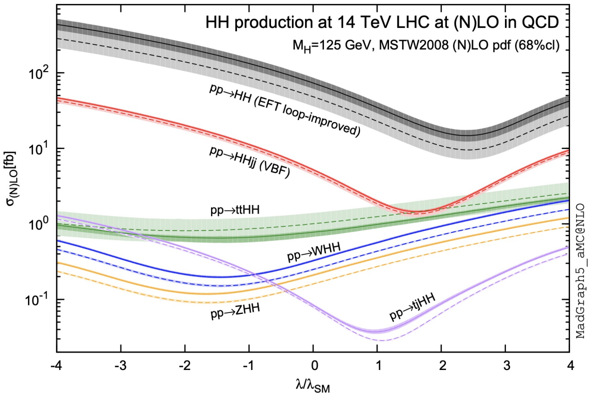

Figure 1.9: Predicted total cross section at the LO and NLO in QCD for HH production channels as a function of κ_λ. The dashed (solid) lines and light (dark) color bands correspond to the LO (NLO) results and to the scale and PDF uncertainties added linearly [40].

1.9. Di-Higgs Boson Decay

There is a possibility of a wide range of decay modes from a pair of Higgs bosons. Figure 1.10 shows the branching ratio and the different decay modes of the Higgs boson. While the $\bar{b}b\bar{b}b$ decay mode is the most dominant decay mode with a branching ratio of 33%, due to the large multi-jet background, it is challenging to separate this signal from the background. There is a trade-off between a large signal event rate and a low or clean background. Thus, various searches for Higgs pair production exist in ATLAS and CMS. A statistical combination of ATLAS results in the $HH \rightarrow b\bar{b}b\bar{b}$ [41, 42], $HH \rightarrow b\bar{b}\tau^+\tau^-$ [43], $HH \rightarrow b\bar{b}\gamma\gamma$ [44], multi-lepton [14], and $HH \rightarrow b\bar{b} + E_T^{miss}$ [45] channels using the full Run 2 data set with up to 140 fb^{-1} of data collected at center-of-mass $\sqrt{s} = 13$ TeV sets an observed (expected) upper limit on the Higgs boson pair production cross-section at 2.4 (2.9) times the SM prediction at 95% confidence level (CL) for $m_H = 125$ GeV [46]. A similar statistical combination of CMS results is carried out in $HH \rightarrow b\bar{b}b\bar{b}$ [47, 48], $HH \rightarrow b\bar{b}\tau^+\tau^-$ [49], $HH \rightarrow b\bar{b}\gamma\gamma$ [50], multi-lepton [51], and $HH \rightarrow b\bar{b}ZZ^*$ [52] channels using the Run 2 data set with at least 138 fb^{-1} of data collected at $\sqrt{s} = 13$ TeV sets an observed (expected) upper limit on the Higgs boson pair production cross-section at 2.5 (3.4) times the SM prediction at 95% CL for $m_H = 125$ GeV [53]. The result of the search presented in this thesis is used in statistical combination for the ATLAS results as part of the multi-lepton channel. The combined limits on the pair production cross-section of a pair of Higgs bosons at ATLAS are shown in Figure 1.11.

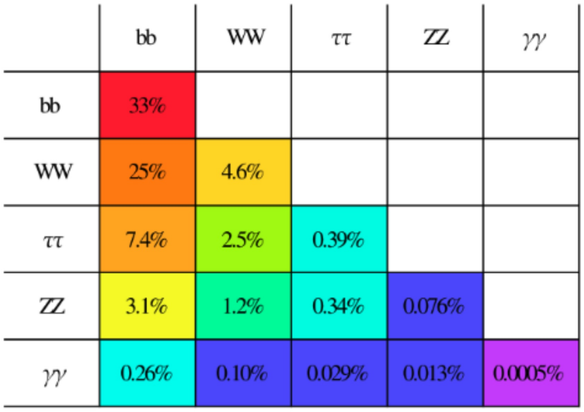

	bb	WW	ττ	ZZ	γγ
bb	33%				
WW	25%	4.6%			
ττ	7.4%	2.5%	0.39%		
ZZ	3.1%	1.2%	0.34%	0.076%	
γγ	0.26%	0.10%	0.029%	0.013%	0.0005%

Figure 1.10: Branching ratio for the decay of di-Higgs boson system [54].

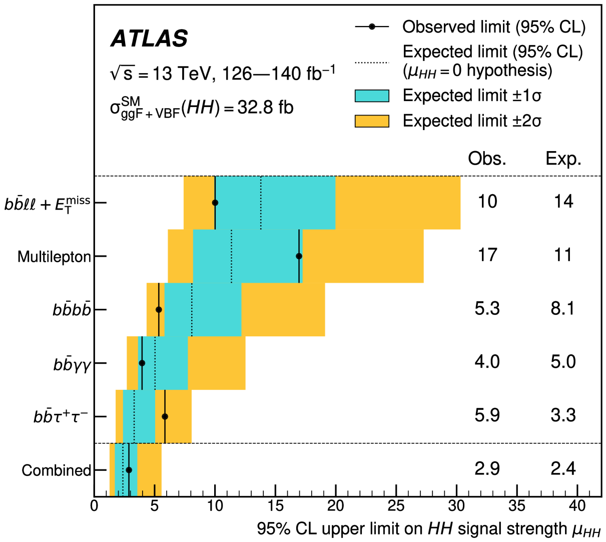

Figure 1.11: Observed and expected 95% CL upper limits on the signal strength for inclusive ggF HH and VBF HH production from the $HH \rightarrow b\bar{b}b\bar{b}$, $HH \rightarrow b\bar{b}\tau^+\tau^-$, $HH \rightarrow b\bar{b}\gamma\gamma$, multi-lepton, and $HH \rightarrow b\bar{b}\ +\ E_T^{miss}$ decay channels and their statistical combination. The predicted SM cross section assumes $m_H = 125$ GeV. The expected limit, along with its associated $\pm 1\sigma$ and $\pm 2\sigma$ bands, is calculated for the assumption of no HH production and with all NPs profiled to the observed data [46].

Chapter 2

Large Hadron Collider and the ATLAS Experiment

2.1. Large Hadron Collider

The Large Hadron Collider (LHC) located at the European Organization for Nuclear Research, CERN, from the French ‘Conseil Européen pour la Recherche Nucléaire’, is a circular particle accelerator spanning 27 km in circumference and more than 100 m deep underground on the border of France and Switzerland [55]. The LHC was built by CERN between 1998 and 2008. Its main function is to collide high-energy beams of protons and lead ions. The LHC‘s first run (Run 1) was between 2009 and early 2013 at center-of-mass energies ($\sqrt{s}$) between 900 GeV and 8 TeV. In the LHC, protons are grouped together into tight packets called bunches. Each bunch consists of about 100 billion protons. Two bunches circulating in opposite directions are collided; bunches are spaced out every 50 ns for Run 1 with a peak number of collisions per bunch of 40 at the peak luminosity of $8{\cdot}10^{33} cm^{-2}s^{-1}$ [56]. Luminosity is a measure of the number of interactions or collisions at a given time. The LHC was shut down after Run 1 from 2013 to 2014 for long shutdown (LS1); then in 2015, the LHC restarted for a second run of data taking. The second three-year data-taking run from 2015 to 2018 of the LHC is called Run 2, and the machine reached a center-of-mass energy of 13 TeV and peak luminosity up to $1.5 \cdot 10^{34} cm^{-2}s^{-1}$. Furthermore, bunch crossings occurred every 25 ns, where each bunch was composed of about 10^{11} protons [57].

The data collected from the collision is measured in “integrated luminosity”, which is the instantaneous luminosity integrated over the data-taking time. The instantaneous luminosity (L) times the cross-section of a certain process (σ) is directly proportional to the number of events (N) produced per second, as shown below.

$$\frac{dN}{dt} = L \cdot \sigma \tag{2.1}$$

Then, the instantaneous luminosity is related to the LHC accelerator parameters as follows:

$$L = \frac{N_b^2 \cdot n_b \cdot f_{rev} \cdot \gamma}{4\pi\epsilon\beta^*} \cdot F \tag{2.2}$$

where N_b is the number of particles per bunch, n_b is the number of bunches per beam, f_{rev} is the revolution frequency, and γ is the Lorentz factor. β^* is the value of the β-function at the collision point and is related to the longitudinal dimension of the beam and also gives the envelope of the beam. Lastly, F is a geometric factor that also includes the angles at which the beams collide [55]. These machine parameters are given in Table 2.1 for Run 2 of LHC operation, and Figure 2.1 shows the delivered luminosity from the LHC.

Table 2.1: Summary of beam and machine parameters during Run 2. [58]

Parameter	**2018**	**2017**	**2016**	**2015**
Energy (TeV)	6.5	6.5	6.5	6.5
Number of bunches	2556	2556 - 1868	2220	2244
Max. stored energy (MJ)	312	315	280	280
$\beta^\star$ (cm)	30 → 27 → 25	40 → 30	40	80
Bunch population, N_b (10^{11} p)	1.1	1.25	1.25	1.2
Normalized Emittance Stable Beams (μm)	1.8 - 2.2	1.8 - 2.2	1.8 - 2	2.6 - 3.5
Peak Luminosity (10^{34} cm^{-2}s^{-1})	2.1	2.0	1.5	< 0.6
Half Crossing Angle (μrad)	160 → 130	150 → 120	185 → 140	185

The LHC operates various accelerators that accelerate particles to increasingly higher energies. Each successive accelerator boosts the energy of a beam before injecting it into the next machine in the sequence. The starting point for proton bunches is a bottle of hydrogen

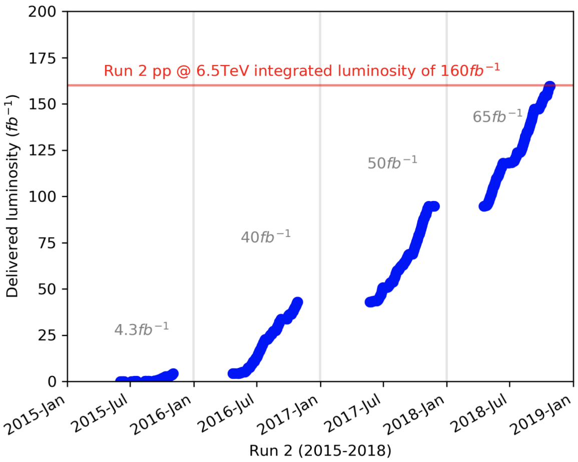

Figure 2.1: LHC delivered luminosity for the high luminosity experiments to ATLAS and CMS. [58]

at one end of Linear Accelerator 2 (Linac2) [59]. The hydrogen atoms pass through an electric field, which strips off their electrons before entering Linac2. The radio-frequency (RF) cavities inside the Linac2 accelerate the proton bunches and reach an energy of 50 MeV. The proton bunches then enter the Proton Synchrotron Booster (PSB) that raises the energy to 1.4 GeV, which is then fed to the Proton Synchrotron (PS). The PS, which has a circumference of 628 m, accelerates the proton bunches to 26 GeV. Finally, the Super Proton Synchrotron (SPS), with a circumference of 7 km, ramps up the proton energy to 450 GeV, which is then fed to the LHC. The proton bunches at the LHC are accelerated to the final energy of 7.5 GeV or the energy of the center-of-mass collision of $\sqrt{s} = 13$ TeV, as illustrated by Figure 2.2.

The LHC‘s main tunnel is repurposed from the previous LEP (Large Electron-Positron Collider) experiment, which was commissioned from 1989 to 2000 [60]. Since LHC operates as a particle-particle collider, there are two rings with counter-rotating beams, unlike a particle-antiparticle collider where both beams can share the same phase space in a single ring [55]. The LEP tunnel had eight straight and eight arc sections. The eight crossing points were flanked by long, straight sections for RF cavities that compensated for the high synchrotron radiation losses from bending for the electron-positron beam. A proton beam does not have the same problem of synchrotron losses as an electron beam and thus ideally could have longer arcs and shorter straight sections for a given circumference. However, it was deemed a cost-effective solution to reuse the existing LEP tunnel for the LHC. LHC is equipped with only four of the possible eight interaction regions to suppress beam crossing, preventing unnecessary disruption of the beams. Furthermore, the finished internal diameter of the LHC tunnel in the arc regions is 3.7 m, preventing the installation of two separate proton rings. Due to this constraint on the available space, a twin-bore magnet design was adopted, which was proposed by John Blewett at the Brookhaven laboratory in 1971 [61], also known as the "two-in-one" superconducting magnet design, which was also put forth as a cost-saving measure [62, 63]. The twin bore magnets design consists of two sets of coils and beam channels within the same mechanical structure and cryostat.

The LHC has four interaction points where collisions occur, and each interaction point houses one of the four major experimental detectors designed with specific physics goals. The four detectors are LHCb (Large Hadron Collider beauty) [64], ALICE (A Large Ion Collider Experiment) [65], ATLAS (A Toroidal LHC ApparatuS) [66], and CMS (Compact Muon Solenoid) [67]. The LHCb detector is designed to study B-physics, the ALICE detector uses lead-lead ion collision to study heavy-ion physics, and the ATLAS and CMS detectors are general-purpose detectors designed to study a wide range of physics phenomena, including the study of SM searches, measurements of SM processes, searches for new physics beyond the Standard Model (SM), and searches for dark matter. The search for pair production of Higgs boson into two light leptons and one τ_{had} final state studied in this thesis uses the Run 2 data set collected from the ATLAS detector.

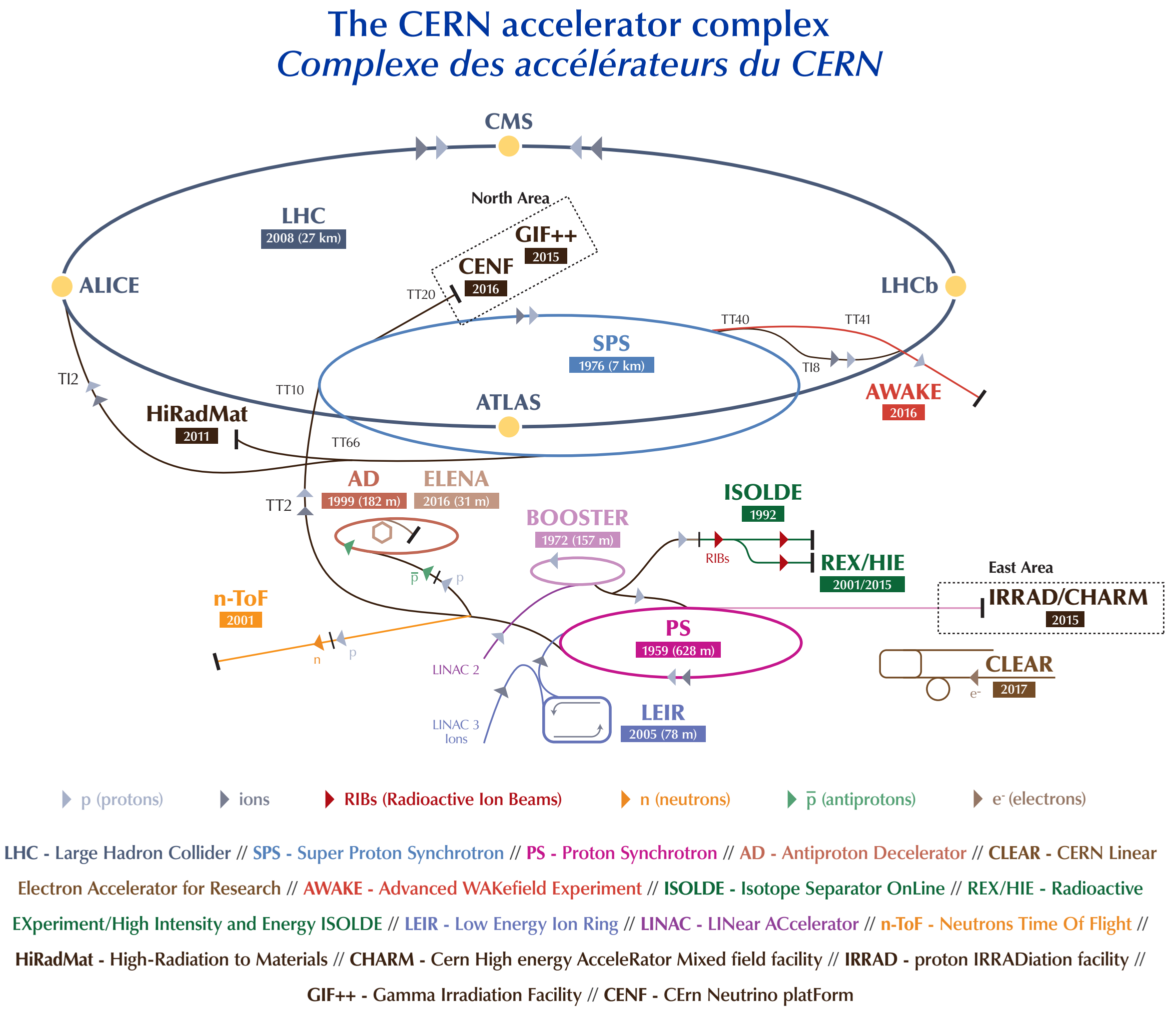

Figure 2.2: A schematic diagram of the CERN accelerator complex with various interaction points [68].

2.2. The ATLAS Detector

The ATLAS detector is a general-purpose detector designed to explore a wide range of physics phenomena, from precision measurements and searches of the SM processes to searches for new physics such as supersymmetry and dark matter. The ATLAS detector is the largest particle detector ever constructed for a collider experiment, with a length of 46 meters, a diameter of 25 meters, and a weight of approximately 7,000 tons. It lies at the interaction point, known as Point 1 (P1) at the LHC, and is situated 100 meters underground.

It has forward-backward symmetry with respect to the interaction point and encompasses a solid angle of almost 4π.

The ATLAS detector features a thin superconducting solenoid surrounding the inner-detector cavity and three large superconducting toroids (one barrel and two end caps) arranged with an eight-fold azimuthal symmetry around the calorimeters. Figure 2.3 shows the geometry and relative location of the magnets. The Inner Detector (ID) is immersed in a 2 T solenoidal field, which consists of three parts: the silicon Pixel Detector, the SemiConductor Tracker (SCT), and the Transition Radiation Tracker (TRT), capable of generating and detecting transition radiation to outer parts. Outside the ID lie two calorimeters: liquid-argon (LAr) electromagnetic sampling calorimeters for measuring electromagnetic radiation and the scintillating Tile calorimeter for measuring hadronic radiation. After the LAr and Tile calorimeters lies a 3.5 T toroidal magnetic field and the Muon Spectrometer to track muon trajectories [67]. A schematic of the ATLAS detector is shown in Figure 2.4.

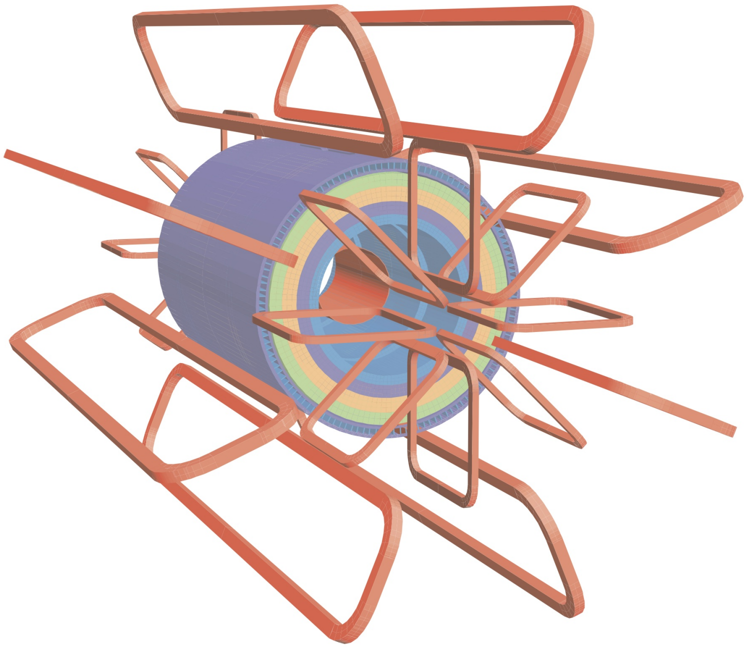

Figure 2.3: Geometry of magnet windings and tile calorimeter steel. The eight barrel toroid coils, with the end-cap coils interleaved are visible. The solenoid winding lies inside the calorimeter volume. The tile calorimeter is modeled by four layers with different magnetic properties. [67]

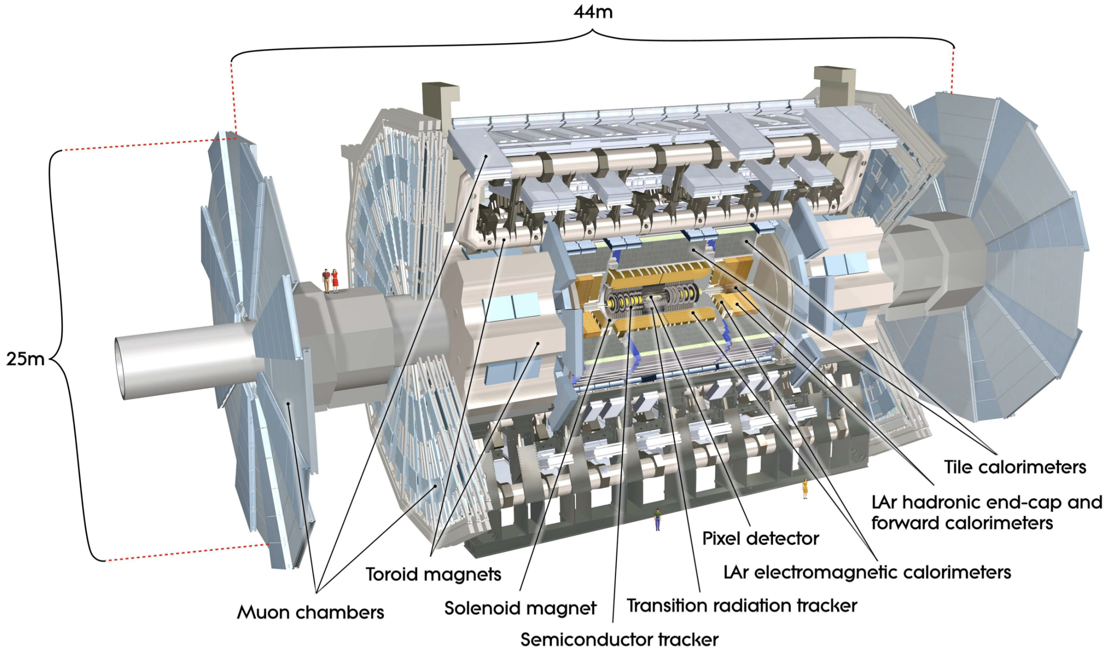

Figure 2.4: A schematic view of the ATLAS detector.

2.2.1. The ATLAS Coordinate System

Due to the cylindrical geometry of the ATLAS detector, cylindrical and spherical coordinate systems are used to describe the position at any point in the detector. The origin of the coordinate system is located at the collision point, which is the center of the detector. The x-axis points from the collision point to the center of the LHC ring, the y-axis points upwards towards the surface, and the z-axis points along the horizontal beam line. The x and y axes are in the transverse plane to the beamline. Side A of the detector is defined with positive z-axis values, and side C is the side with negative z-axis values. Side A points towards the Salève mountains, and side C points towards the Jura mountains. An azimuthal angle ϕ is defined as the angle around the z-axis and lies on the transverse plane (x-y plane). The polar angle θ is defined as the angle made with the beam line. However, it is convenient to use the pseudorapidity (η) instead of the polar angle θ, as pseudorapidity is approximately equal to rapidity (y) for massless or highly relativistic particles, and rapidity differences are invariant with respect to longitudinal boosts which is invariant under Lorentz boost. The pseudorapidity is defined as $\eta = ln(\tan(\frac{\theta}{2}))$ for massless objects, and for massive objects $\eta = \frac{1}{2}ln(\tan(\frac{E+p_z}{E-p_z}))$ is used, where E is the energy and p_z is the longitudinal momentum of the particle. Here, $\eta = \infty$ lies along the z-axis and $\eta = 0$ points towards the y-axis. The distance between two points can be defined in $\eta - \phi$ space as $\Delta R = \sqrt{(\Delta\eta)^2 + (\Delta\phi)^2}$.

2.2.2. Inner Detector

The ID operates within a $|\eta|$ less than 2.5. It is capable of robust pattern recognition, excellent momentum resolution, and both primary and secondary vertex measurements for charged particles. The ID has a footprint of ±3512 mm in length and 1130 mm in radius inside a 2 T solenoidal magnetic field. As charged particles pass through the magnetic field, the momentum and charge of a particle can be measured using the curvature of the particle‘s track. The ID is composed of three sub-detectors: the Pixel Detector, the SemiConductor Tracker (SCT), and the Transition Radiation Tracker (TRT).

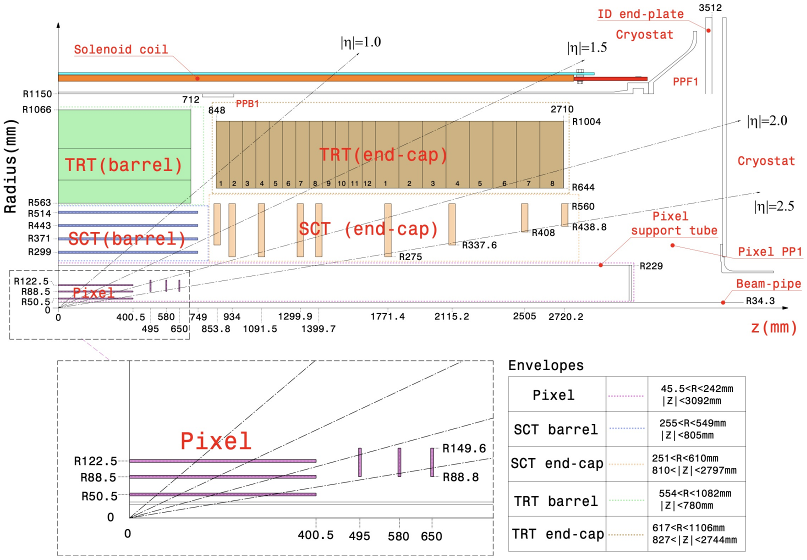

Figure 2.5: Plan view of a quarter-section of the ATLAS inner detector showing each of the major detector elements with its active dimensions and envelopes [67].

The pixel detector is located closest to the beam pipe. It is composed of three barrel layers and a total of six disk layers, three at each end of the barrel region. The individual sensors on the pixel detector are called pixel sensors. The pixel sensor is composed of an array of bipolar diodes made by implanting high positive (p^+) and negative (n^+) dose regions on each side of an oxygenated n-type bulk wafer. Each pixel sensor consists of a 256 ± 3 μm thick n-bulk. The bulk contains n^+ implants on the read-out side and the p-n junction on the back side. There are 1744 identical pixel modules where each pixel sensor has a nominal size of 50×400 μm^2 in the barrel region and 50×600 μm^2 in the disk-shaped front-end region. The total number of pixels in the system is approximately 67 million in the barrel and 13 million in the end caps, covering a total active area of about 1.7 m^2. During the first long shutdown in 2013-2014, a new innermost detector was installed called the Insertable B-layer (IBL) at a distance of 33.25 mm from the beam pipe. The IBL consists of even finer pixel sensors at 50×200 μm^2 and a total of 26880 pixel cells.

The SCT has four cylinders in the barrel and nine discs in each of the two end caps. There are 8448 identical rectangular sensors using single-sided p-in-n sensors in the barrel region and 6944 with different wedge-shaped geometries in the end caps. SCT sensors are arranged back-to-back with a relative angle of 40 $mrad$ to allow measuring two space points in each set of strips. Both Pixel and SCT are kept at -5°C to -10°C to reduce noise performance after radiation damage [67].

The TRT consists of three parts: a barrel and two end caps capable of detecting transition radiation. They are composed of thin-walled polyimide drift tubes (straws) with a diameter of 4 mm, and at the center is a gold-plated tungsten wire 31 μm in diameter. The barrel part is comprised of 52,544 straws 144 cm in length oriented parallel to the beam. The two end caps each contain 122,880 straws 37 cm in length radially aligned to the beam axis. Due to the detector geometry, particles traverse at least 36 straws in the region $|\eta| < 2$, providing continuous large radii tracking in ID, which enhances particle identification, momentum measurement, and tracking. The straw tubes are filled with a mixture of Xe (70%), CO_2 (27%), and O_2 (3%) gas, which acts as the active material. When charged particles cross the TRT straws, they ionize the active gas mixture and produce about 5-6 primary ionization clusters per mm of path in gas. The ions are accelerated towards the central anode wire, outputting a detectable signal [69]. The straw tube wall is made of two 35 μm thick multi-layer films that are bonded back-to-back. The bare material, a 25 μm thick polyimide film, is coated on one side with a 0.2 μm aluminum layer, which is protected by a 5-6 μm thick graphite-polyimide layer [67]. The straws are interleaved with polypropylene fiber in the barrel and foil in the end caps, which serve as transition radiation material. Electrons passing through this material will produce transition radiation photons, which are used for electron identification and discrimination from photons and hadrons.

2.2.3. The ATLAS Calorimeters

Calorimeters are designed to measure particle energy. Particles entering the calorimeter initiate a particle shower, and their energy is deposited in the calorimeter material. There are two types of calorimeters based on the particle interaction. Electromagnetic (EM) calorimeters are specifically designed to measure the energy of particles that interact primarily via the EM interaction, and hadronic calorimeters are designed to measure particles that interact via the strong nuclear force and EM interaction. The total thickness of the calorimeters is designed to provide sufficient interaction length for the decaying particles and reduce punch-through into the muon system. The ATLAS calorimeter is shown in Figure 2.6.

The high-energy electrons and positrons mainly lose energy through Bremsstrahlung processes, whereas high-energy photon interactions are dominated by electron-positron pair production. If the energy of an incident electron, positron, or photon is high enough (in the GeV range), these processes give rise to particle multiplication, which is referred to as electromagnetic showers [70]. The number of particles is doubled, and the energy of the particles is halved at each increment of radiation length, X_0. This is called the Heitler

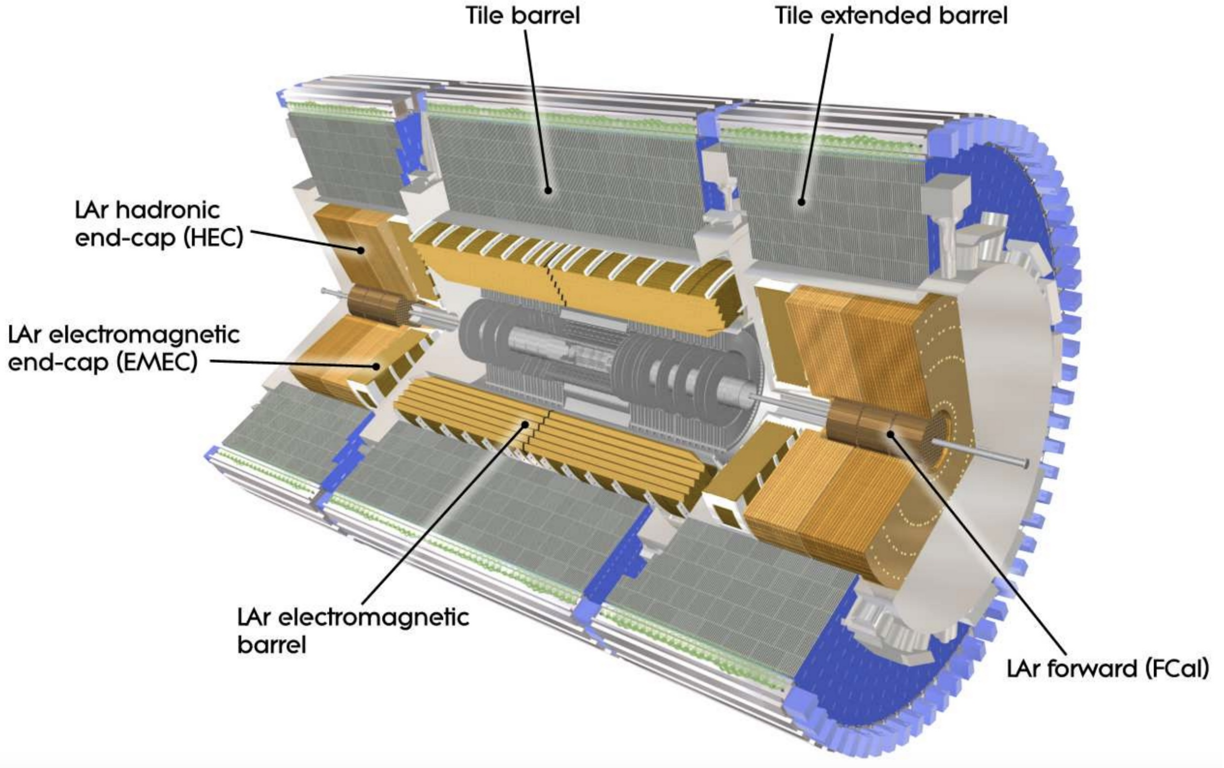

Figure 2.6: Cut-away view of the ATLAS calorimeter system [67].

model [71]. When the energy of electrons and positrons drops below a critical energy, energy loss is dominated by ionization and excitation.

Whereas the inelastic collision between high-energy hadrons and nuclei produces forward-directed collision products (more hadrons), which are subject to further collisions. The interaction of secondary particles with more nuclei gives rise to particle multiplication, leading to hadronic showers. The multiplication process roughly continues until the energy falls below the pion production threshold (at energies greater than 290 MeV). Hadronic showers also have an electromagnetic component, owing to the production of neutral pions, which decay into energetic photon pairs. Additionally, the interaction length for hadronic showers is significantly longer than that for electromagnetic showers, as hadronic interactions occur via the strong force, which has a lower cross-section compared to electromagnetic interactions.

The ATLAS electromagnetic calorimeter (ECAL) can accurately measure the energy, position, and identity of a particle. The ATLAS ECAL is a sampling calorimeter composed of lead plates and liquid argon (LAr). The lead plates absorb the incident particles, whereas LAr is ionized by the incoming charged particles. The ionized electrons drift toward Kapton electrodes due to an applied high voltage, which produces a signal. The signal has a triangular shape whose peak is proportional to the energy loss of the particle. The lead plates are arranged in an accordion geometry to provide full coverage in ϕ. The accordion waves in the barrel are axial and run in ϕ, and the waves are parallel to the radial direction and run axially in the end caps.

The ATLAS ECAL is subdivided into four subsystems, as shown in Figure 2.6: EM barrel calorimeter (EMB), EM end-cap calorimeter (EMEC), hadronic end-cap calorimeter (HEC), and forward calorimeter (FCal). The EMB is composed of two identical half-barrels, centered around the z-axis. The EMB covers the region $|\eta| < 1.475$ with 1024 accordion-shaped lead absorbers with readout electrodes in between. The EMB module is divided into three layers, as shown in Figure 2.7: the first layer has a high granularity in η to provide precise measurements of the EM shower position, the second layer is the main energy measurement layer, and the third layer is used to measure EM shower tails. Additionally, a presampler module is placed in front of the EMB to correct for energy loss in the material upstream of the calorimeter. The EMEC consists of two coaxial wheels located on each side of the EMB. The EMEC covers the region $1.375 < |\eta| < 2.5$ and $2.5 < |\eta| < 3.2$. The region $1.375 < |\eta| < 1.52$ is called the "crack" region or transition region as the transition region between the barrel and the end-cap calorimeters, where particles traverse more material. The EMEC is also divided into three layers with similar functions as the EMB.

The subset of detectors used to measure energy from hadronic showers are the Tile Calorimeter (shown in Figure 2.8), the HEC, and the FCal. The Tile calorimeter is a sampling calorimeter with steel as the absorber material and scintillating tiles as the active material. The Tile calorimeter is located behind the LAr calorimeter and covers the region $|\eta| < 1.7$. The Tile calorimeter is divided into a barrel ($|\eta| < 1.0$) and two extended barrels ($0.8 < |\eta| < 1.7$). The inner and outer radii are 2280 mm and 4230 mm, respectively. The barrel part is 5640 mm in length along the beam axis, while each of the extended barrels is 2910 mm long [72]. The Tile calorimeter is divided into three layers: the first layer is the thin gap scintillator, the second layer is the thick gap scintillator, and the third layer is the steel absorber. Ionizing particles crossing the tiles induce the production of ultraviolet scintillation light in the scintillator (polystyrene), and this light is subsequently converted to visible light by wavelength-shifting fibers. The light is then collected by photomultiplier tubes. The HEC is located behind the EMEC and covers the region $1.5 < |\eta| < 3.2$. The HEC is also a sampling calorimeter with copper as the absorber material and LAr as the active material. The FCal is located at the very forward region of the detector and covers the region $3.1 < |\eta| < 4.9$. The FCal is composed of three modules: the first module is made of copper and measures the electromagnetic component, while the second and third modules are made of tungsten and measure the hadronic component. Each module consists of a metal matrix with regularly spaced longitudinal channels filled with the electrode structure consisting of concentric rods and tubes parallel to the beam axis. The LAr in the gap between the rod and the tube is the sensitive medium.

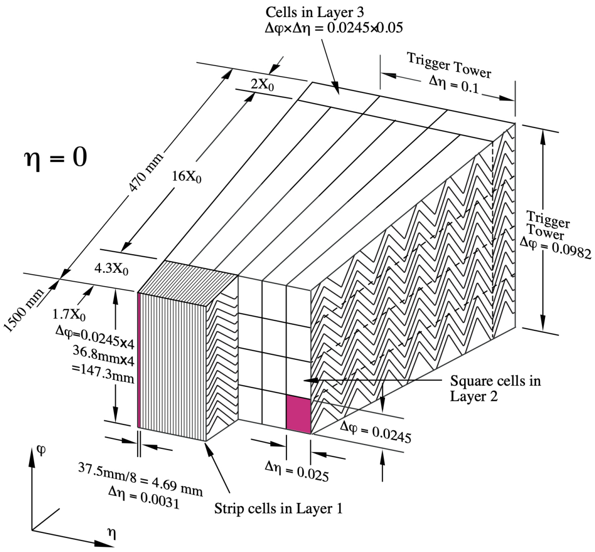

Figure 2.7: Sketch of a barrel module where the different layers are visible. The granularity in η and ϕ of the cells of each of the three layers are also shown. [67]

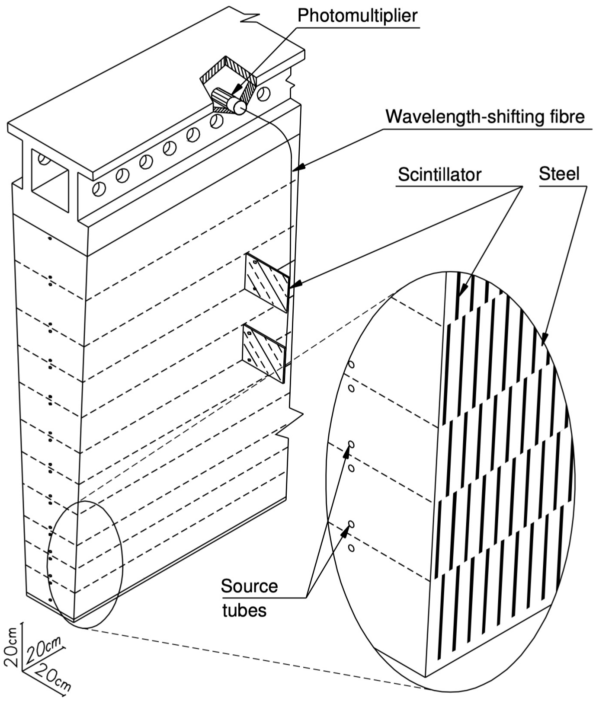

Figure 2.8: Schematic of the Tile Calorimeter [67].

2.2.4. The Muon Detectors

The Muon Spectrometer (MS) is based on the magnetic deflection of muon tracks in the large superconducting air-core toroid magnets. There are three such toroidal magnets; two end-cap toroids covering a range of $1.6 < |\eta| < 2.7$ provide magnetic bending power of 1 to 1.7 Tm, and one barrel toroid provides bending power of 1.5 to 5.5 Tm in the range of $|\eta| < 1.4$. The region $1.4 < |\eta| < 1.6$ is the transition region between the end-cap toroid and barrel toroid where the magnetic deflection is provided by a combination of barrel and end-cap fields with lower magnetic bending power. Each toroid consists of eight coils assembled radially and symmetrically around the beam axis. The end-cap toroid coils are rotated by 22.5 *deg* with respect to the barrel toroid coil. The combined magnetic field is approximately orthogonal to the muon trajectory [73]. The MS is composed of four types of subdetectors: the Resistive Plate Chambers (RPC), the Monitored Drift Tubes (MDT), the Cathode Strip Chambers (CSC), and the Thin Gap Chambers (TGC). The main parameters of the MS are shown in Table 2.2.

Table 2.2: Main parameters of the muon spectrometer [67].

Monitored drift tubes	**MDT**
- Coverage - Function	$\|\eta\|< 2.7$ (innermost layer: $\|\eta\|< 2.0$) Precision tracking
Cathode strip chambers	**CSC**
- Coverage - Function	$2.0 < \|\eta\|< 2.7$ Precision tracking
Resistive plate chambers	**RPC**
- Coverage - Function	$\|\eta\|< 1.05$ Triggering, second coordinate
Thin gap chambers	**TGC**
- Coverage - Function	$1.05 < \|\eta\|< 2.7$ (2.4 for triggering) Triggering, second coordinate

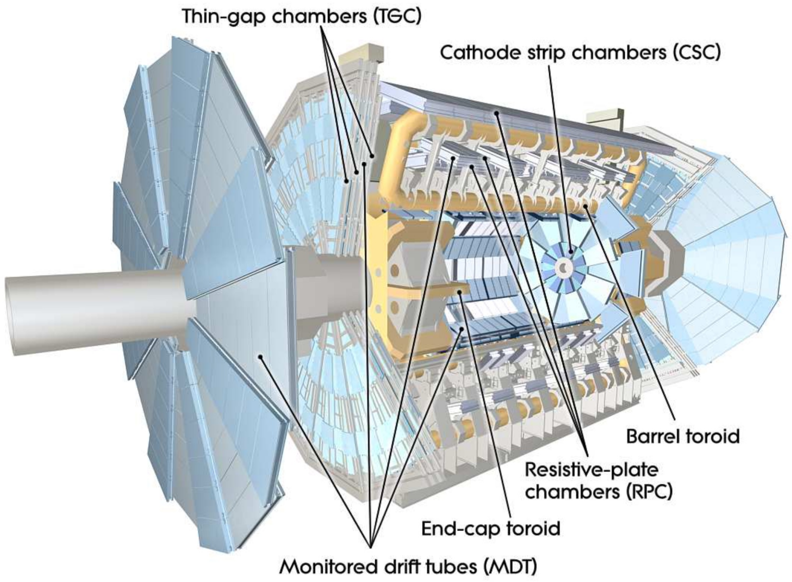

Figure 2.9: Cut-away view of the ATLAS muon system. [67]

2.2.5. The Trigger and Data Acquisition System

At the LHC, multiple proton-proton interactions can occur within a single bunch crossing or in nearby bunch crossings; this is known as pile-up events. There are two main types of pile-up scenarios: in-time pile-up, which is additional proton-proton collision occurring in the same bunch-crossing as the collision of interest, and out-of-time pile-up, which is additional proton-proton collision occurring in the previous or next bunch-crossing. Other types of pile-up are beam halo events, which are events affected by upstream collimators; beam gas events, which are collisions between proton bunches and residual gas inside the beam pipe; and effects from gas in the detector cavern called cavern background [74]. These pile-up events affect the identification of collisions of interest.

The Trigger and Data Acquisition (TDAQ) system is responsible for real-time decision-making on data recording and saving events for a given collision. High instantaneous luminosity of $1.5 \cdot 10^{34}\ cm^{-2}s^{-1}$ seen in Run 2 with a center-of-mass energy of 13 TeV meant a significant increase in the event rate from interesting physics processes compared to Run 1 conditions where the instantaneous luminosity was $8 \cdot 10^{33}\ cm^{-2}s^{-1}$ with a center-of-mass energy of 8 TeV [56,57]. To record and identify interesting events, the TDAQ system selects events using a two-stage trigger system: a hardware-based first-level trigger (L1) [75] and a software-based high-level trigger (HLT) [76]. The L1 trigger uses custom electronics to determine Region-of-Interest (RoIs) in the detector, and as an input takes coarse granularity information from the calorimeter and muon detector. The L1 trigger reduces the event rate from approximately 40 MHz to a rate below 100 kHz. The L1 trigger has less 2.5 μs of decision latency time to construct RoIs, which are sent to the HLT. The HLT can run sophisticated selection algorithms using full granularity detector information in either the RoIs or the whole event. The HLT further reduces the output event rate to approximately 1 kHz with an average processing time of 200 ms in order to record events to disk [77]. A schematic overview of the ATLAS TDAQ system is shown in Figure 2.10. The Fast TracKer (FTK) was undergoing commissioning during Run 2 and was not used by the HLT for trigger decisions [77].

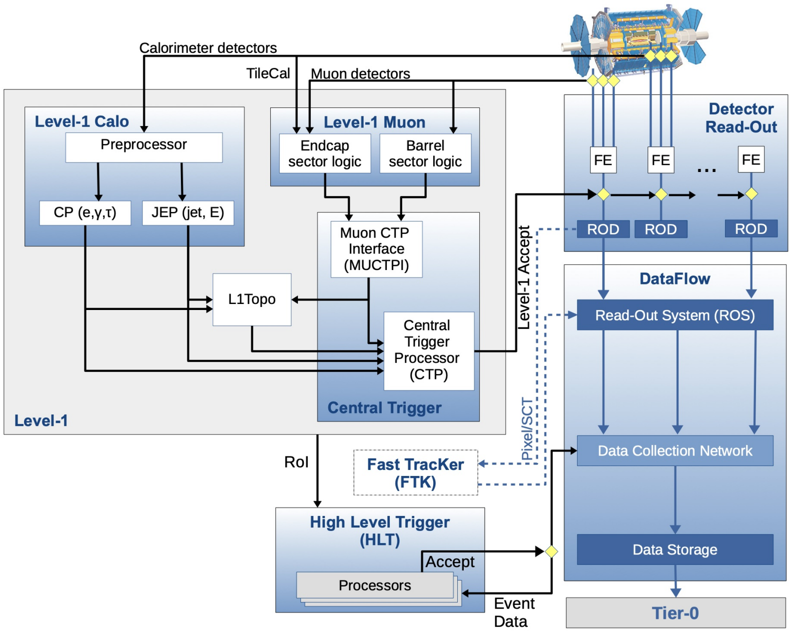

Figure 2.10: Schematic layout of the ATLAS TDAQ system in Run 2 [77].

Chapter 3

Search for $HH \rightarrow multilepton$

The goal of this thesis is to search for Higgs boson pair production (HH) in a final state containing two same-sign light leptons (electrons or muons) and one hadronically decaying tau lepton, where only the neutral and charged hadrons stemming from the tau lepton decay constituting the visible part of the tau lepton decay ($\tau_{\text{had-vis}}$) are considered. The $\tau_{\text{had-vis}}$ is required to have the opposite charge to one of the light leptons. The final state also includes missing transverse energy from neutrinos and a low jet multiplicity, with at least two reconstructed jets expected. Such a signature arises predominantly from the decay modes $HH \rightarrow W^+W^-\tau^+\tau^-$, $HH \rightarrow W^+W^-W^+W^-$, and $HH \rightarrow \tau^+\tau^-\tau^+\tau^-$. Only combinations yielding the target final state of two same-sign light leptons and one oppositely charged hadronic tau are selected which is defined as $2lSC1\tau_{\text{had}}$ channel. Due to the complexity and ambiguity involved in fully reconstructing the Higgs boson pair decay chain, this analysis instead focuses on the observable final-state objects without explicitly reconstructing the intermediate particles. Events with the same final state signature ($2lSC1\tau_{\text{had}}$) that do not originate from Higgs boson pair production constitute the background. This background is dominated by diboson (VV) production, primarily VV fully leptonic decays, where V can be either W or Z bosons, with at least one tau decaying hadronically. To enhance sensitivity, the analysis employs a multivariate technique based on boosted decision trees to discriminate signal events from background.

3.1. Object Reconstruction

To accurately interpret proton-proton collisions at the LHC, both theoretical modeling and detector simulation are essential. This analysis relies heavily on Monte Carlo (MC) simulations to model signal and background processes, as well as the detector response to final-state particles [78–80]. High-energy hadron collisions are broadly categorized into hard- and soft-scattering processes, governed by quantum chromodynamics (QCD). While hard-scattering processes can be described using perturbative QCD (pQCD), soft processes rely on phenomenological models due to their non-perturbative nature. Monte Carlo simulations provide a chain of steps that model the full evolution of an event, from the initial parton-level interactions to the final reconstructed objects. In ATLAS, MC simulation consists of six main stages [81].

The MC production at ATLAS begins with the matrix element calculation stage, which samples individual events from the matrix element of the hard scattering process. This step produces a list of high-momentum partons for the parton showering/hadronization stage. These event generators are general purpose software packages that produce matrix elements that describe the probability and kinematics while taking into account the underlying physics and fundamental interactions like the electroweak and strong interactions.

The parton shower/hadronization takes the partons from the hard scatter and simulates the QCD processes that happen at lower energy scales until hadronization (the formation of color-singlet bound states) using phenomenological models tuned to data. The output is a list of stable particles that are then passed to the detector simulation. Stable particles are particles that have sufficient lifetime to enter the detector. Up to this point, the MC simulation is referred to as the truth record and is not ATLAS specific, as the result depends entirely on theory predictions. The matrix element calculation and/or parton shower/hadronization is sometimes collectively referred to as the event generator; some examples are MadGraph [82], Sherpa [83], Powheg [84], Pythia [85] and Herwig [86].

The detector simulation uses the GEANT4 [87] software package to simulate the path of stable particles through the detector as they interact with the detector material and magnetic fields, while also producing new particles in those interactions, or potential decay.

The output of the detector simulation is a list of energy deposits in various sub-detectors of ATLAS. The digitization step converts the energy deposits into electronic signals that are read out by the detector electronics. The outcome of digitization is equivalent to the raw data read in by the ATLAS detector with additional truth information. The trigger simulation simulates the trigger decisions that are the same as in the data. The final step is the reconstruction, which reconstructs the digital signals into "physics objects" such as electrons, photons, hadronic jets, and missing transverse energy. An extensive software suite [88] is used to reconstruct the data and MC events using information from various parts of the detector and sub-detector or other low-level reconstructed objects. Below is a brief description of the reconstruction and identification of physics objects (electrons, muons, jets, and missing transverse energy) used in this thesis. This section describes the object definition for the $2lSC1\tau_{had}$ channel.

3.1.1. Track Reconstruction

Tracks refer to the reconstructed trajectories of charged particles as they traverse the detector. These tracks are formed by identifying and connecting a series of localized energy deposits, or hits, in the inner tracking detectors, particularly the pixel and semiconductor tracker (SCT) layers, and extended to TRT whenever feasible. The track reconstruction begins with the formation of clusters from the hits in the pixel and SCT detectors. These clusters are used to create three-dimensional position measurements (space points), from which track seeds are formed. The track-finding algorithm proceeds iteratively, using combinations of these space points to generate candidate tracks [89]. A set of quality criteria is required to reject poorly reconstructed or misidentified tracks from low-energy particles, pile-up, and noise. The 'loose' tracks must have p_T greater than 500 MeV, $|\eta|$ less than 2.5, a minimum of 7 silicon hits, no shared hits, 2 or fewer 'holes' in the pixel and semiconductor tracker, and 1 or fewer pixel 'holes'. The 'holes' are an intersection between the reconstructed trajectory and a sensitive detector element where no corresponding cluster is found. The 'tight' tracks must fulfill additional requirements, including having 9 or more silicon hits if $|\eta|$ is less than 1.65 (barrel region) or 11 or more hits if $|\eta|$ is greater than 1.65 (endcap region), at least one hit in one of the two innermost pixel layers, and no holes in the pixel detector.

3.1.2. Primary vertices

A vertex requires two tight tracks to be a candidate vertex. Multiple candidate vertices may exist due to pile-up events in the same bunch crossing. Therefore, the primary vertex in an event is chosen as the vertex with the highest $\sum p_T^2$ of associated tracks [90]. All physics objects are then derived from the selected primary vertex.

3.1.3. Topological Clusters

A cluster algorithm is used to reconstruct the energy deposits in the calorimeter called topocluster. The algorithm starts with a seed cell, which is a cell with energy above a certain threshold. The algorithm then expands the cluster by adding neighboring cells that are above a lower threshold and are within a certain distance from the seed cell. The cluster is then calibrated to account for the energy deposited in the dead material between the cells and the energy lost due to leakage outside the cluster. The topological clusters are used to reconstruct electromagnetic and hadronic objects such as photons, electrons, and jets [91].

3.1.4. Trigger

Events in ATLAS are selected using trigger chains, where each chain is composed of an L1 trigger item and a sequence of HLT algorithms. These algorithms reconstruct physics objects—such as leptons, photons, jets, missing transverse momentum, total energy, or B-

meson candidates—and apply kinematic selection criteria. Each trigger chain is specifically designed to target a particular physics signature. The complete set of trigger chains configured for a given data-taking period is referred to as the trigger menu. The single-lepton triggers and dilepton triggers used in this analysis for 2015-2018 data are listed in Table 3.1. All of those triggers are un-prescaled, meaning that every event passing the trigger conditions is recorded, rather than only a fraction of them. The trigger strategies follows that of the ttH multilepton analysis using 80 fb^{-1} of data [92], which features a similar final state. A logical OR between dilepton (DL) and single-lepton (SL) triggers is applied. The trigger efficiencies in the simulated samples are corrected to match the measured efficiencies in the data using trigger scale factors.

3.1.5. Leptons

Electrons are reconstructed and identified by matching tracks in ID tracks to the energy deposited in the ECAL. Electron candidates are required to have $p_T > 10$ GeV and $|\eta| < 2.47$, excluding the transition region in calorimeter $1.37 < |\eta| < 1.52$. The electron candidates are identified using a likelihood technique based on the shower shape and track information. A light lepton requirement is defined as ‘Tight’ (T), as shown in Table 3.2. The tight electrons are required to satisfy a tight identification working point that is overall 80% efficient at selecting electrons in $Z \to ee$ events. Electron candidates are required to satisfy tight isolation working points of a ‘Prompt Lepton Veto’ (PLV) BDT designed to reject non-prompt electrons. Prompt leptons originate directly from the primary interactions, whereas non-prompt leptons do not originate from primary interactions. The isolation requirements are approximately 85% efficient for electrons with E_T of 10 GeV and fully efficient for electrons with $E_T > 40$ GeV. Electron candidates are also required to satisfy the ‘e/γ ambiguity’ criteria, which is designed to reject electrons that are likely to be converted photons based on track information. Lastly, electron candidates are required to satisfy the charge misidentification

Table 3.1: List of lowest p_T-threshold, un-prescaled single lepton and dilepton triggers used for 2015–2018 data taking.

	Single lepton triggers (2015)
μ	`HLT_mu20_iloose_L1MU15`, `HLT_mu50`
e	`HLT_e24_lhmedium_L1EM20VH`, `HLT_e60_lhmedium`, `HLT_e120_lhloose`
	Dilepton triggers (2015)
$\mu\mu$ (asymm.)	`HLT_mu18_mu8noL1`
ee (symm.)	`HLT_2e12_lhloose_L12EM10VH`
$e\mu, \mu e$ ($\sim$symm.)	`HLT_e17_lhloose_mu14`
	Single lepton triggers (2016)
μ	`HLT_mu26_ivarmedium`, `HLT_mu50`
e	`HLT_e26_lhtight_nod0_ivarloose`, `HLT_e60_lhmedium_nod0`, `HLT_e140_lhloose_nod0`
	Dilepton triggers (2016)
$\mu\mu$ (asymm.)	`HLT_mu22_mu8noL1`
ee (symm.)	`HLT_2e17_lhvloose_nod0`
$e\mu, \mu e$ ($\sim$symm.)	`HLT_e17_lhloose_nod0_mu14`
	Single lepton triggers (2017 / 2018)
μ	`HLT_mu26_ivarmedium`, `HLT_mu50`
e	`HLT_e26_lhtight_nod0_ivarloose`, `HLT_e60_lhmedium_nod0`, `HLT_e140_lhloose_nod0`
	Dilepton triggers (2017 / 2018)
$\mu\mu$ (asymm.)	`HLT_mu22_mu8noL1`
ee (symm.)	`HLT_2e24_lhvloose_nod0`
$e\mu, \mu e$ ($\sim$symm.)	`HLT_e17_lhloose_nod0_mu14`

BDT, which is designed to reject electron candidates where the charge is likely to have been wrongly attributed.

Muon candidates are reconstructed from tracks in MS, which are matched to ID tracks where available. The tight muon candidates are required to have $p_T > 10$ GeV and $|\eta| < 2.5$.

A tight muon is required to satisfy a medium identification working point that is typically 97% efficient at selecting prompt muons. The tight PLV working point is 57% efficient at selecting the lowest p_T prompt muons and rises to 87% for muons with $p_T > 20$ GeV. Additionally, selection on the transverse and longitudinal impact parameters with respect to the primary vertex, $|d_0|$ and $|z_0|$ respectively, is applied to all candidates, which reduces the contribution of non-prompt electrons and muons. Electrons (muons) are required to have $|d_0|/\sigma_{d_0} < 5(3)$ and $|z_0 \sin\theta| < 0.5$ mm (where σ_{d_0} is the uncertainty on the reconstructed d_0, and θ is the polar angle of the track).

Table 3.2: The definition of the light leptons used in the analysis.

	e	μ
Minimum p_T	10 GeV	10 GeV
η	$|\eta| < 1.36$ or $1.52 < |\eta| < 2.45$	$|\eta| < 2.5$
Isolation	PLV tight	PLV tight
Identification	Tight	Medium
Charge mis-ID BDT	Yes	N/A
e/γ ambiguity	Yes	N/A
$|d_0|/\sigma_{d_0}$	< 5	< 3
$|z_0 \sin\theta|$	< 0.5 mm	< 0.5 mm

3.1.6. Hadronically Decaying Taus

The hadronically decaying tau lepton candidates (τ_{had}) are reconstructed from tracks in the ID and energy deposits in the calorimeter. The τ_{had} candidates are seeded from jets using the anti$-k_T$ jet reconstruction algorithm [93,94] with radius parameter R =0.4, and clusters of calorimeter cells calibrated using a local hadronic calibration (LC) as inputs [95,96]. The τ_{had} candidates are required to have $p_T > 20$ GeV and $|\eta| < 2.5$. The calorimeter transition region ($1.37 < |\eta| < 1.52$) is excluded. The τ_{had} candidates are required to have either one or three associated tracks, with a total charge of ±1. A recursive neural network (RNN)-based identification algorithm is used to discriminate hadronically decaying tau lepton candidates τ_{had} from quark- or gluon-initiated jets. A medium identification working point is used, which has an identification efficiency of 75% (60%) for one (three) prong τ_{had} decays. The τ_{had} candidates geometrically overlapping with very loose electrons are rejected using a dedicated BDT discriminant algorithm that can differentiate between τ_{had} and electron candidates [97]. Furthermore, overlapping muons are also rejected, which is summarized in Section 3.1.9. The definition of τ_{had} is summarized in Table 3.3.

Table 3.3: The definition of τ_{had} candidates used in the analysis.

	τ_{had}
Identification	JetID RNN Medium
η	$\lvert\eta\rvert< 2.5$ exclude $1.37 < \lvert\eta\rvert< 1.52$
p_T	> 20 GeV
Number of Tracks (N_{track})	1 or 3
Charge	±1
Electron veto	pass

3.1.7. Jets

Reconstructed jets are based on particle-flow objects built from topological clusters in the calorimeter and reconstructed tracks [98]. The jets are clustered using the anti-k_T algorithm with a radius parameter of $R = 0.4$. Jets are required to have $|\eta|< 2.5$ and $p_T > 25$ GeV. Events with $|\eta|< 2.4$ and $p_T < 60$ GeV are required to satisfy the tight jet-vertex tagger [99] to reduce the contribution of jets originating from pile-up interactions. Events are required to pass the a quality selection to remove jets that may be contaminated by non-collision backgrounds or instrumental noise.

Jets with b-hadrons, b-jets, are identified using a deep learning neural network algorithm, DL1r [100] which takes the impact parameters of ID tracks to reconstruct jet flavors. A working point of 77% efficiency to identify jets associated with a b-hadron in simulated $t\bar{t}$ events is used to veto b-jets. Jets with $|\eta| < 2.4$ are considered.

3.1.8. Missing Transverse Energy

As protons travel in the longitudinal direction, the transverse momentum of the system is assumed to be zero and useful to measure particles invisible to the detector. The negative vector sum of transverse momenta of all the hard-event signals in the form of reconstructed and calibrated 'hard' physics objects that includes electrons, photons, muons, τ-leptons, and jets in an event is defined as the missing transverse momentum ($\overrightarrow{E}_T^{miss}$), and the magnitude of $\overrightarrow{E}_T^{miss}$ is defined as missing transverse energy (E_T^{miss}) [101]. The vector sum also contains soft-event signals, which are the reconstructed charged particle tracks that are associated with the hard-scatter vertex but not associated with a hard object [102].

3.1.9. Object Overlap Removal

The reconstructed electrons, muons, τ_{had} , and jets are produced independent of each other. There is no check to determine if the same set of clusters or tracks are used for reconstructing two different objects. In the overlap-removal procedure, when two reconstructed objects are geometrically close to each other under a certain threshold (here ΔR of 0.2), one of the objects is removed. The procedure is applied in sequence as follows:

- Any calorimeter muon found to share a track with an electron is removed.
- Any electron found to share a track with a non-calorimeter muon is removed.
- Any jet found within a ΔR of 0.2 of an electron is removed.

- Any electron subsequently found within ΔR of of 0.4 of a jet is removed.
- Any jet with less than 3 tracks associated to it found within ΔR of 0.2 of a muon is removed.
- Any jet with less than 3 tracks associated to it which has a muon inner-detector track ghost-associated to it, is removed.
- Any muon subsequently found within ΔR of 0.4 of a jet is removed.
- Any tau found within a ΔR of 0.2 of a electron is removed.
- Any tau found within a ΔR of 0.2 of any type of muon with p_T greater than 2 GeV is removed, while noting that if the tau p_T is greater than 50 GeV, it will only be removed if it is found to overlap with a combined-type muon, which are muons reconstructed using both the Inner Detector and Muon Spectrometer.
- Any jet found within a ΔR of 0.2 of a tau is removed.
- Any photon found within a ΔR of 0.4 of an electron or a muon is removed.
- Any jet found within ΔR of 0.4 of a photon is removed.

3.2. Data and Simulated samples

The analysis uses $140.1 \pm 1.2\ fb^{-1}$ of Run 2 data during 2015 to 2018 collected by the ATLAS detector at $\sqrt{s} = 13$ TeV [103, 104]. The number of pp interactions per bunch crossing (pile-up) in this data set ranges from about 8 to 70, with an average of 34.

MC simulations are used to model the HH signal and background production. There are three MC campaigns for each simulated process, mc16a, mc16d, and mc16e, corresponding to different assumptions on the distribution of pile-up in the 2015-2016, 2017, and 2018 periods, respectively. The different MC campaigns are needed because pileup is increasing across the years and detector conditions are also different. Corrections are applied to the simulated events so that the particle candidates selection efficiencies, energy scales, and resolutions match those determined from well-understood data samples where HH signal does not contribute. The simulated events are normalized to the corresponding predicted cross-sections, which is needed for fair comparison with the experimental data. Unless otherwise specified, charge conjugation is implied throughout this thesis; for example, “WW” refers to a W^+W^- pair, “tt” to a $t\bar{t}$ pair, and so on.

3.2.1. Signal Samples

- Nominal ggF signal samples: The event generation is performed at the next-to-leading-order (NLO) accuracy with Powheg-Box-V2 for matrix element calculation. Parton showering and hadronization are simulated using the PYTHIA8 generator with a set of tuned parton shower parameters (A14 tune) [105] and using the NNPDF 2.3 LO Parton Distribution Functions (PDF) set [106]. The PDF describes the probability distributions of the momentum and energy carried by the partons (quarks and gluons) inside a proton or other hadrons. The EvtGen [107] program is used for b- and c-hadron modeling. Detector effects are simulated using AltfastII (AF2) [108], with a fast simulation of the calorimeter response. The Higgs are allowed to decay to $WW/ZZ/\tau\tau$. Events containing leptons with $p_T > 7$ GeV and $|\eta| < 3$ are retained by applying a lepton filter. The same configurations of the options are applied for the $\kappa_\lambda = 10$ variation. Scale factors are derived as a function of κ_λ in bins of the generator-level invariant mass of the HH system and applied to the simulated ggF, $\kappa_\lambda = 1$ sample. The ggF, $\kappa_\lambda = 10$ signal sample is used to validate the derived scale factors. A reweighting method is used to obtain a ggF signal sample at other κ_λ values by performing a linear combination of independent generator-level samples at three different κ_λ values ($\kappa_\lambda = 0$, 1, and 20) [109].

- Alternative ggF signal samples: The alternative signal samples are produced by the Powheg-Box-V2 interface to Herwig7, using the PDF4LHC15 PDF set to measure the parton shower uncertainties. The filtering strategy is in line with PYTHIA8 sample cases.

- Nominal VBF signal samples: The event generation is performed at the leading-order (LO) accuracy with MadGraph5_aMC@NLO 2.2.X or 2.3.X [110] for matrix element calculation. Parton showering and hadronization are simulated using the PYTHIA8 generator with the A14 tune [105] and using the NNPDF 2.3 LO PDF set [106]. The EvtGen [107] program is used for b- and c-hadron modeling. Detector effects are simulated using AltfastII (AF2) [108], which is a fast simulation of the calorimeter response.
  - The branching ratios of the intermediate particles are set to BR($h^0 \to W^+W^-$) = 0.706, BR($h^0 \to Z^0Z^0$) = 0.087, and BR($h^0 \to \tau^+\tau^-$) = 0.207 to be consistent with the ggF values. A lepton filter limits the kinematics of electrons and muons to $p_T > 7$ GeV and $|\eta| < 2.8$, and a tau lepton filter limits hadronic τ leptons to $p_T > 13$ GeV and $|\eta| < 2.8$.

- Alternative VBF signal samples: The alternative signal samples are produced by the MadGraph5_aMC@NLO 2.2.X or 2.3.X [110] interface to Herwig7, using the PDF4LHC15 PDF set to study the parton shower uncertainties. The filtering strategy is in line with PYTHIA8 sample cases.

3.2.2. Background Samples

Monte Carlo simulation samples were produced for the different background processes using the configurations shown in Table 3.4, with the samples used to estimate the systematic uncertainties in parentheses. The pileup is modeled using events from minimum-bias interaction generated with Pythia 8.186 [85] using the NNPDF2.3LO set of PDFs and the A3 set of tuned parameters [111], and overlaid onto the simulated hard-scatter events according to the luminosity profile of the recorded data. The generated events were processed through a simulation [112] of the ATLAS detector geometry and response using Geant4 [87], and through the same reconstruction software as the data. Corrections were applied to the simulated events so that the particle candidates‘ selection efficiencies, energy scales, and energy resolutions match those determined from data control samples. The simulated samples are normalized to their cross sections and computed to the highest order available in perturbation theory, as summarized in Table 3.13.

For Table 3.4, the samples used to estimate the systematic uncertainties are indicated in between parentheses, the difference between the nominal samples and alternative sample is taken as the systematic uncertainty. V refers to the production of an electroweak boson (W or Z). The parton distribution function (PDF) shown in the table is the one used for the matrix element (ME). If only one parton distribution function (PDF) is shown, the same one is used for both the matrix element (ME) and parton shower generators; if two are shown, the first is used for the matrix element calculation and the second for the parton shower. Tune refers to the underlying-event tune of the parton shower generator. MG5_aMC refers to MadGraph5_aMC@NLO 2.2.X or 2.3.X [110]; Pythia 8 refers to version 8.2 [113]; Herwig7 refers to version 7.0.4 [114]; MePs@Nlo refers to the method used in Sherpa [115–119] to match the matrix element to the parton shower. Samples using Pythia 8 have heavy flavor hadron decays modeled by EvtGen 1.2.0 [107]. All samples include leading-logarithm photon emission, either modeled by the parton shower generator or by PHOTOS [120]. The mass of the top quark and SM Higgs boson was set to 172.5 GeV and 125 GeV, respectively.

Table 3.4: The configurations are used for event generation of signal and background processes, with the samples used to estimate the systematic uncertainties enclosed in parentheses.

Process	Generator	ME order	Parton shower	PDF	Tune
$t\bar{t}W$	Sherpa 2.2.10	NLO	Sherpa	NNPDF3.0 NNLO	Sherpa default
	(MG5_aMC)	(NLO)	(Pythia 8)	(NNPDF3.0 NLO)	(A14)
$t\bar{t}t\bar{t}$	MG5_aMC	NLO	Pythia 8	NNPDF3.1 NLO	A14
	(Sherpa 2.2.10)	(NLO)	(Sherpa)	(NNPDF3.0 NNLO)	(Sherpa default)
$t\bar{t}H$	Powheg-BOX [121]	NLO	Pythia 8	NNPDF3.0 NLO [106]	A14
	(Powheg-BOX)	(NLO)	(Herwig7)	(NNPDF3.0 NLO)	(H7-UE-MMHT)
	(MG5_aMC)	(NLO)	(Pythia 8)	(NNPDF3.0 NLO)	(A14)
$t\bar{t}(Z/\gamma^* \to l^+l^-)$	Sherpa 2.2.11	NLO	Sherpa	NNPDF3.0 NNLO	Sherpa default
	(MG5_aMC)	(NLO)	(Pythia 8)	(NNPDF3.0 NLO)	(A14)
$t\bar{t} \to W^+bW^-\bar{b}l^+l^-$	MG5_aMC	LO	Pythia 8	NNPDF3.0 LO	A14
$t(Z/\gamma^*)$	MG5_aMC	NLO	Pythia 8	NNPDF2.3 LO	A14
$tW(Z/\gamma^*)$	MG5_aMC	NLO	Pythia 8	NNPDF2.3 LO	A14
$t\bar{t}W^+W^-$	MG5_aMC	LO	Pythia 8	NNPDF2.3 LO	A14
$t\bar{t}$	Powheg-BOX	NLO	Pythia 8	NNPDF3.0 NLO	A14
	(Powheg-BOX)	NLO	(Herwig7.1.3)	(NNPDF3.0 NLO)	(H7-UE-MMHT)
$t\bar{t}t$	MG5_aMC	LO	Pythia 8	NNPDF2.3 LO	A14
s-, t-channel, Wt single top	Powheg-BOX [122, 123]	NLO	Pythia 8	NNPDF3.0 NLO	A14
VV, $qqVV$, $lowm_{\ell\ell}$, VVV	Sherpa 2.2.2	NLO	Sherpa	NNPDF3.0 NNLO	Sherpa default
$Z \to l^+l^-$	Sherpa 2.2.1	NLO	Sherpa	NNPDF3.0 NLO	Sherpa default
$Z \to l^+l^-$ (matCO)	Powheg-BOX	NLO	Pythia 8	CTEQ6L1 NLO	A14
$Z \to l^+l^- + (\gamma*)$	Powheg-BOX	NLO	Pythia 8	CTEQ6L1 NLO	A14
W+jets	Sherpa 2.2.1	NLO	Sherpa	NNPDF3.0 NLO	Sherpa default
VH	Powheg-BOX	NLO	Pythia 8	NNPDF3.0 NLO	A14

3.3. Event Selection

For $2lSC1\tau_{had}$ channel, the events are required to pass the selection in Table 3.5.

Table 3.5: Summary of event selection.

Selection	Description
Trigger	• Global Trigger Decision from the central trigger processor (CTP) which is the initial L1 hardware-based decision based on predefined physics trigger conditions • Trigger matching with Tight electrons or muons for single-lepton or dilepton triggers in Table 3.1
Leptons	• Two leptons with same electric charge • Invariant mass of the two leptons must be larger than 12 GeV • Transverse momentum of each lepton must be larger than 20 GeV • Leptons pass the selection in Table 3.2
Hadronic Tau	• Exactly one hadronically decaying τ • τ_{had} must have opposite charge to the light leptons • Transverse momentum of τ_{had} must be larger than 25 GeV • τ_{had} candidates must pass the selection in Table 3.3
Jet	• b-jet veto: events containing b-jets are discarded • At least 2 jets are required

3.4. Multivariate Analysis Strategy

After selecting the events using the trigger, lepton, hadronic tau, and jet selection described in Section 3.3, a multivariate discriminant is used to separate signal from background. ROOT‘s TMVA framework [124, 125] is used to train a Boosted Decision Tree (BDT) classifier. It is based on the gradient boosting algorithm [126]. A single BDT is trained using a combined signal sample consisting of both ggF and VBF events, with only VV background samples used during training. The BDT is trained on the selected events using the 13 variables. The variables are listed in Table 3.6 ranked according to their separation power to discriminate signal from background. The distributions of the input variables for signal and background are shown in Figure 3.2, obtained using the TMVA framework. Figure 3.1 shows selected distributions for the signal region with the other backgrounds. Furthermore, the linear correlations are shown in Figure 3.3 between the input variables for both signal and background as a correlation matrix. The differences between the correlations are found to be consistent between signal and background.

Table 3.6: Variables used in the multivariate analysis for $2lSC1\tau_{had}$ channel.

Variable	Description	Rank	Separation power
$\Delta R(\ell_0,\ \ell_1)$	Distance between leading and sub-leading leptons	1	12.48%
$M(\ell_0,\ \mathrm{jet}_{\mathrm{leading}})$	Invariant mass of leading lepton and leading jet	2	11.57%
$M(\ell_0,\ \mathrm{closest}-\mathrm{jet})$	Invariant mass of leading lepton and it‘s closest jet	3	11.39%
$\Delta R(\ell_0,\ \mathrm{closest\ jet})$	Distance between leading lepton and it‘s closest jet	4	10.24%
$\Delta R(\ell_0,\ \mathrm{jet}_{\mathrm{leading}})$	Distance between leading lepton and leading jet	5	9.11%
$M(\ell_1,\ \mathrm{jet}_{\mathrm{leading}})$	Invariant mass of sub-leading lepton and leading jet	6	9.04%
$\Theta(boost\ell_0,\ell_1,\ \tau_{had},\mathrm{jet}_{\mathrm{leading}})$	Angle between tau and leading jet after Lorentz boost to two leading leptons system	7	8.50%
$\Theta(boost\ell_0,\ell_1,\ \tau_{had},\mathrm{jet}_{\mathrm{sub-leading}})$	Angle between tau and sub-leading jet after Lorentz boost to two leading leptons system	8	6.87%
$\Delta R(\ell_1,\ \mathrm{closest\ jet})$	Distance between sub-leading lepton and it‘s closest jet	9	6.60%
$\Delta R(boost\ell_0,\ \tau_{had},\ell 0,\mathrm{jet}_{\mathrm{sub-leading}})$	Distance between leading lepton and sub-leading jet after Lorentz boost to tau and leading leptons system	10	6.48%
$M(\ \tau_{had},\ell closest)$	Invariant mass of tau and it‘s closest lepton	11	6.00%
$\Delta R(boost\ell_1,\ \tau_{had},\ell 1,\mathrm{jet}_{\mathrm{leading}})$	Distance between sub-leading lepton and leading jet after Lorentz boost to tau and sub-leading leptons system	12	5.88%
$M(\ell_0,\ \mathrm{jet}_{\mathrm{sub-leading}})$	Invariant mass of leading lepton and sub-leading jet	13	5.85%

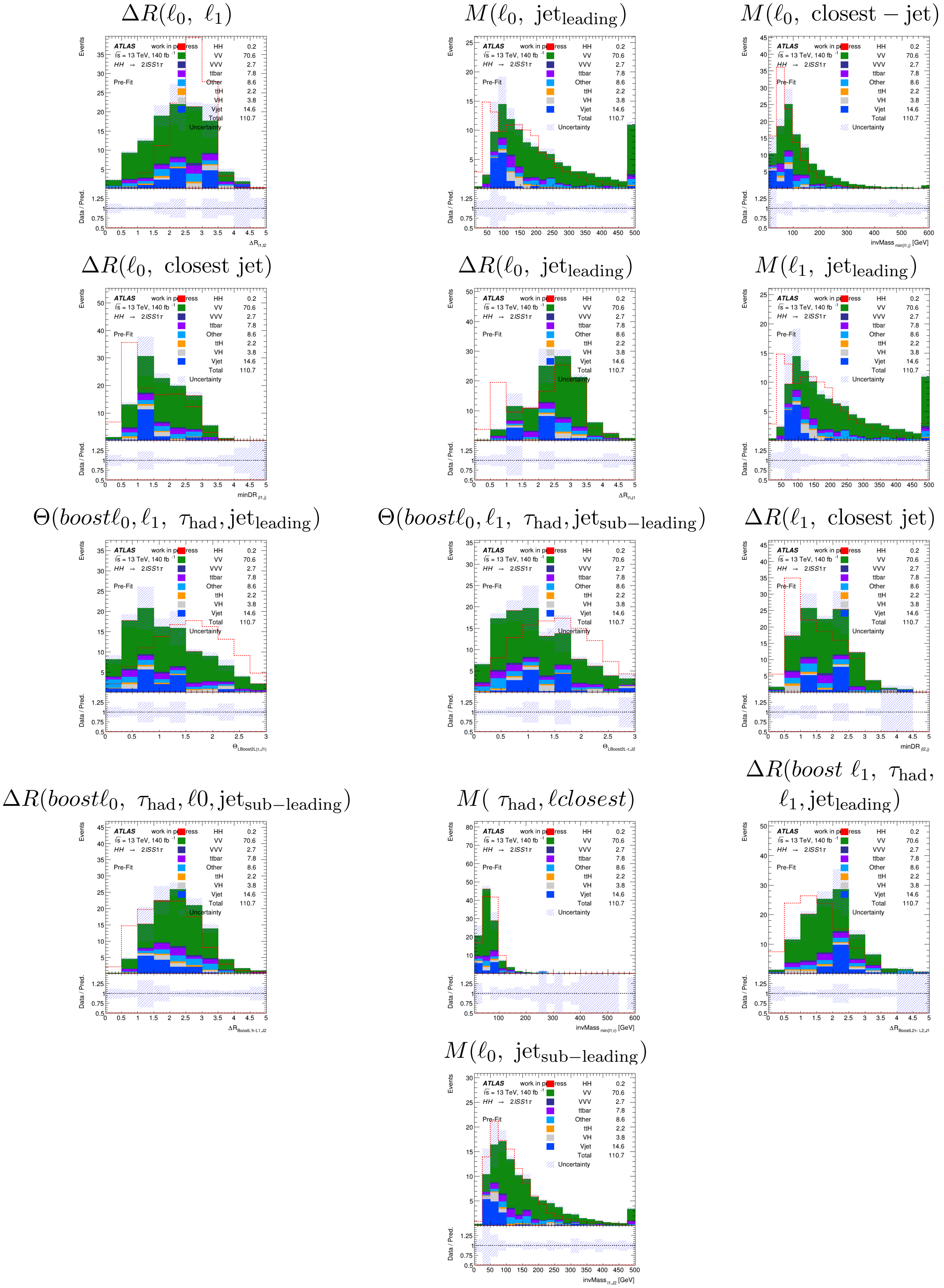

$\Delta R(\ell_0,\ \ell_1)$

$M(\ell_0,\ \mathrm{jet}_{\mathrm{leading}})$

$M(\ell_0,\ \mathrm{closest-jet})$

$\Delta R(\ell_0,\ \mathrm{closest\ jet})$

$\Delta R(\ell_0,\ \mathrm{jet}_{\mathrm{leading}})$

$M(\ell_1,\ \mathrm{jet}_{\mathrm{leading}})$

$\Theta(boost\ell_0,\ell_1,\ \tau_{\mathrm{had}},\mathrm{jet}_{\mathrm{leading}})$

$\Theta(boost\ell_0,\ell_1,\ \tau_{\mathrm{had}},\mathrm{jet}_{\mathrm{sub-leading}})$

$\Delta R(\ell_1,\ \mathrm{closest\ jet})$

$\Delta R(boost\ell_0,\ \tau_{\mathrm{had}},\ell 0,\mathrm{jet}_{\mathrm{sub-leading}})$

$M(\ \tau_{\mathrm{had}},\ell closest)$

$\Delta R(boost\ \ell_1,\ \tau_{\mathrm{had}},\ \ell_1,\mathrm{jet}_{\mathrm{leading}})$

$M(\ell_0,\ \mathrm{jet}_{\mathrm{sub-leading}})$

Figure 3.1: The distributions of variables used for MVA training for the signal region. The signal has been normalized to the total background. Systematic errors are not included.

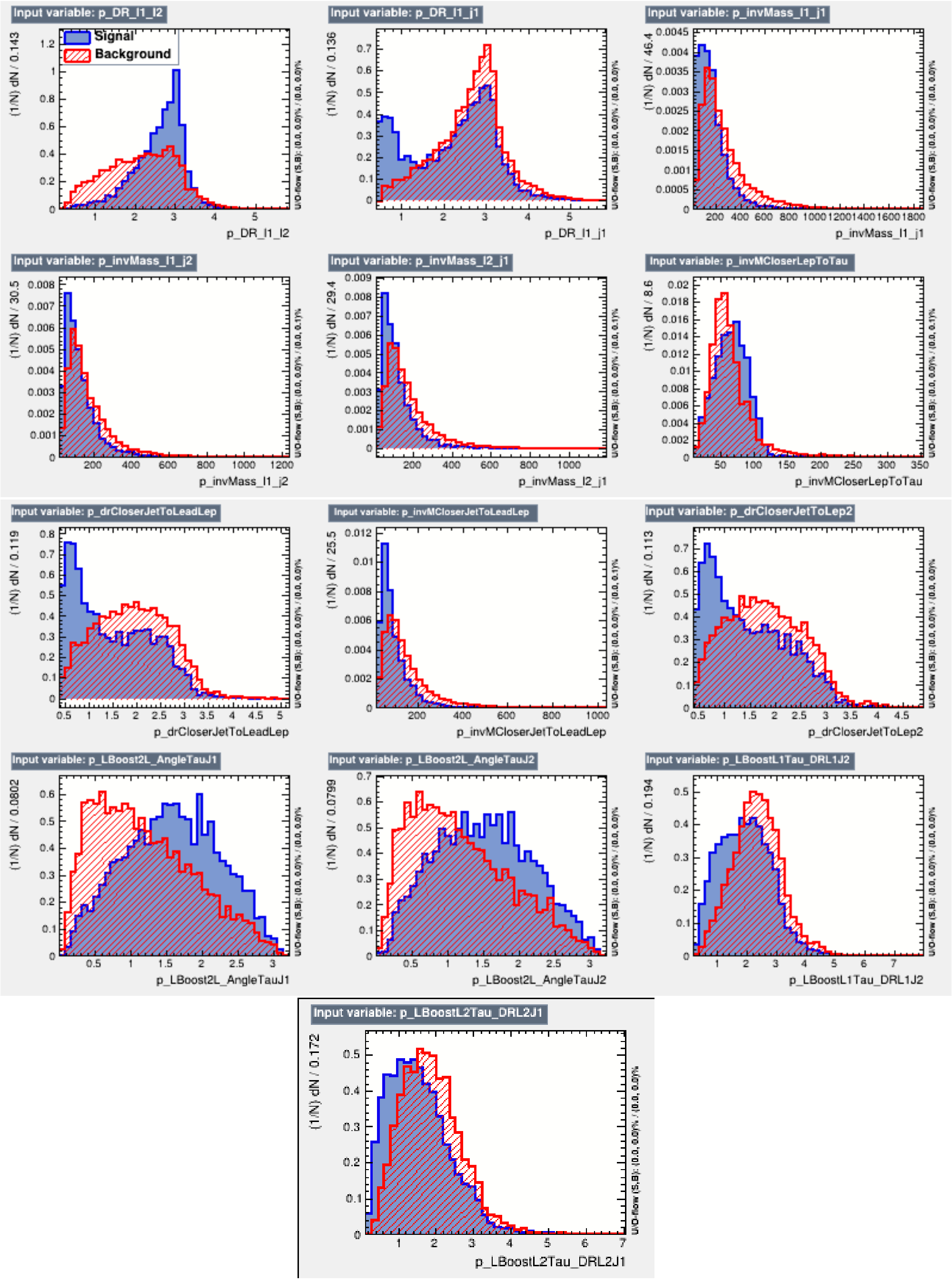

Figure 3.2: Signal (blue) and background (red) distributions of 13 input variables used in the BDT training of $2lSC1\tau_{had}$ channel.

The hyperparameters of the BDT are optimized to maximize the area under the receiver operating characteristic (ROC) curve. The ROC curve is a graphical representation of the trade-off between the true positive rate (TPR) and false positive rate (FPR) at various

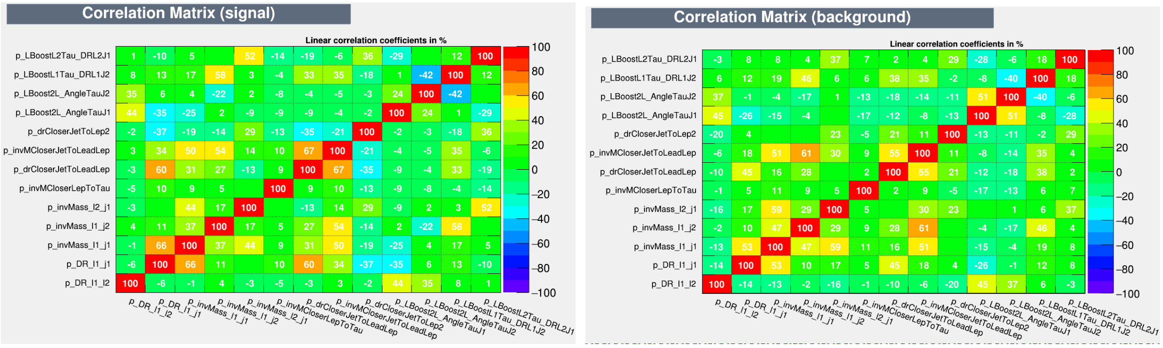

Figure 3.3: Correlation coefficients between the 13 BDT input variables for signal (left) and background (right) of $2lSC1\tau_{had}$ channel.

threshold settings. The area under the ROC curve (AUC) is a measure of the classification model‘s ability to distinguish between signal and background events. A hyperparameter optimization software called Optuna [127] was used to search for a set of hyperparameters that had the largest AUC value. The history of the number of trials that were run and the AUC value of each of those trials is shown in Figure 3.4. One-fifth of the dataset was selected at random to be used for testing, and the remainder was used for training. This was chosen to match the subset of the dataset needed for the $k-$fold cross-validation method.

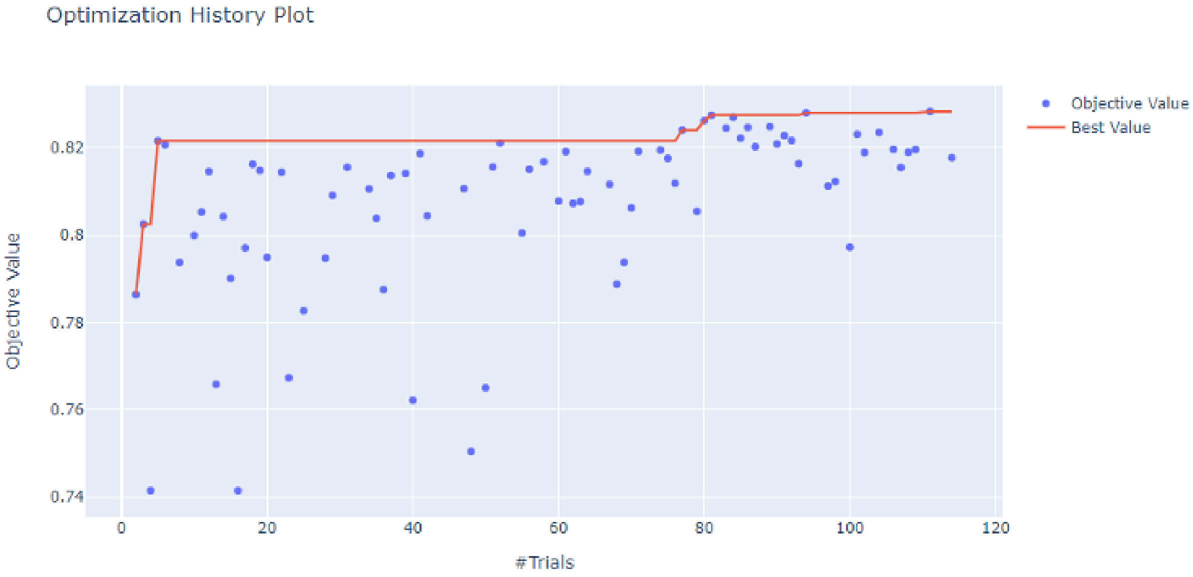

Figure 3.4: Number of different trials vs AUC value for the trial.

The hyperparameters from the optimization step above are used for the $k-$fold cross-validation method, first introduced in Ref. [128], with $k = 5$ folds over signal and background samples. The dataset is divided into k equally sized subsets, or "folds". Then, k number of BDT classifiers are trained, each time using $k - 1$ folds for training and the remaining fold for testing. The k test sets are used as the result of the cross-validation method. This ensures that the application of the BDT is unbiased from the training phase. Each event is assigned to a fold according to the remainder when its event number is divided by the total number of folds. For example, for event number 101 and $k = 5$ folds, the remainder when dividing the event number by the number of folds gives 1, so the event goes to fold 1. Each fold is treated as an independent training and testing set, and the hyperparameters remain the same for each fold.

The final BDT output score distributions for both training and testing are shown in Figure 3.5, and the corresponding ROC curve is presented in Figure 3.6. From the BDT output score distribution, it is evident that a high BDT output corresponds to signal-like events, while a low BDT output indicates background-like events. Additionally, the BDT output score distribution for fold 0, including both training and testing datasets, is shown in Figure 3.7. There is a close agreement between the training and testing BDT output score distributions, which suggests minimal overfitting or underfitting.

3.5. Signal Region

The BDT output score distribution is used to define the signal region (SR). The SR is selected as the region with a high BDT score (≥ -0.2), along with the selection criteria described in Section 3.3. The BDT distribution and the number of jets in the SR are shown in Figure 3.8, and the corresponding event yields are presented in Table 3.7. To minimize statistical fluctuations and enhance sensitivity, the binning of the BDT discriminant is optimized using an automated binning algorithm. In this procedure, bins are iteratively merged until a target fraction of signal and background events is achieved. The merging

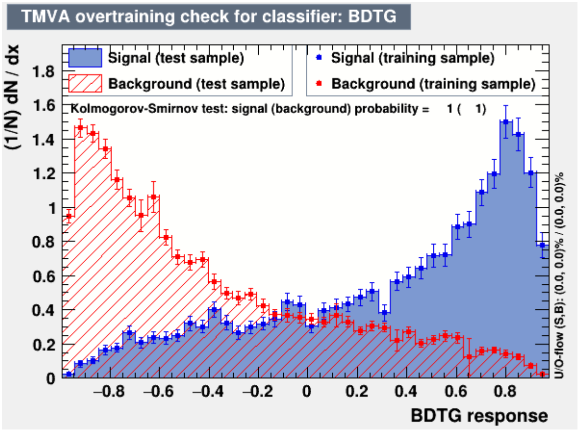

Figure 3.5: The BDT with Gradient Boost distribution for the signal and background obtained during the training and testing of $2lSC1\tau_{had}$ channel.

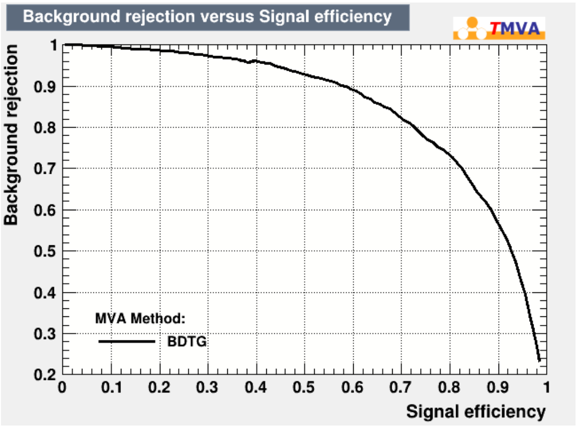

Figure 3.6: The background rejection versus signal efficiency for BDT of $2lSC1\tau_{had}$ channel.

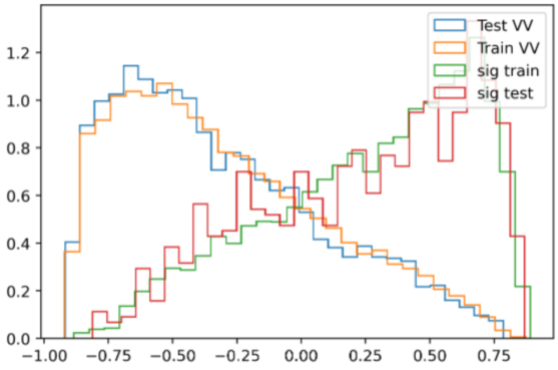

Figure 3.7: BDT output score distribution for fold 0.

criterion is governed by the function give below:

$$Z = z_s \frac{n_s}{N_s} + z_b \frac{n_b}{N_b}, \tag{3.1}$$

where n_s (n_b) is the number of signal (background) events in the current bin, and N_s (N_b) is the total number of signal (background) events. The parameters z_s and z_b are free coefficients that control the relative weight of signal and background in the merging decision. The bin merging process stops when $Z > 1$. For this analysis, the choice of $z_s = 2$ and $z_b = 3$ yields the optimal expected 95% CL exclusion limit. The resulting bin edges for the SR are [−0.200000, 0.094240, 0.311800, 0.584440, 0.777160, 1.000000].

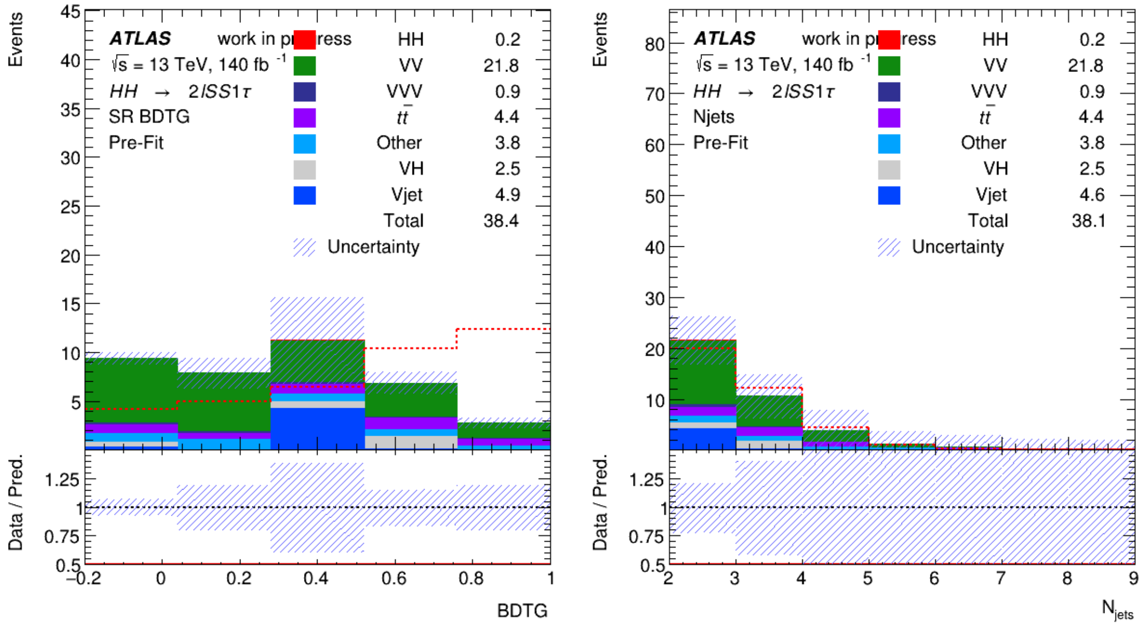

Figure 3.8: The distributions of BDTG score (left) and the number of jets (right) in the SR. The signal has been normalized to the total background. Systematic errors are not included.

Table 3.7: Event yields from pre-fit plots for all the MC samples in $2\ell SS1\tau_{\text{had}}$ signal region. The uncertainties are only statistical.

Process	Event yields
VV+jj	1.286 ± 0.091
VV fully leptonic	20.259 ± 1.41
WZ	0.046 ± 0.004
WW	0.232 ± 0.569
WZlνq, ZZ	0
VVV	0.88 ± 0.06
$t\bar{t}$	4.38 ± 0.35
tV	0.14 ± 0.02
tVV	0.22 ± 0.02
ttH	1.12 ± 0.08
VH	2.46 ± 1.26
ttW	1.07 ± 0.08
ttZ	0.82 ± 0.06
Z+jets	0.6 ± 0.03
W+jets	4.31 ± 1.2
ttWW	0.08 ± 0.004
stop	0.27 ± 0.03
Rare_tt	0.051 ± 0.004
Total Background	38.22 ± 4.93
HH (signal)	0.19 ± 0.02

3.6. Background Modeling

The background is composed of processes where the event selection criteria defined in Section 3.3 are satisfied by prompt leptons and real τ_{had} produced in the final states decay product using the background MC simulation as defined in Section 3.2.2. The background sources for leptons can be broadly categorized into two groups: irreducible and reducible backgrounds.

The irreducible background consists of processes that yield final states similar to the signal, with genuine prompt leptons and real hadronically decaying tau leptons (τ_{had}). These backgrounds are challenging to suppress, as they mimic the signal topology closely and pass the selection criteria naturally. The dominant irreducible background is diboson production (VV), with smaller contributions from VVV, tV, $t\bar{t}V$, VH, $t\bar{t}H$, $t\bar{t}t\bar{t}$, and other rare processes such as $t\bar{t}WW$ and $t\bar{t}t$. Since backgrounds other than VV contribute only marginally in the signal region, no dedicated control regions are defined for them, and their contributions are taken directly from MC simulations. However, to improve the accuracy of the simulation, a dedicated control region (CR) enriched in the dominant background, VV, events is used. This CR is constructed to be orthogonal to the signal region and is used to extract a normalization factor (NF) through a fit, which is then applied to correct the Monte Carlo modeling.

Reducible backgrounds are poorly modeled by MC due to the complex nature of object misidentification and non-prompt sources. Reducible backgrounds can be further divided into two categories according to fake types, as shown in Figure 3.9:

- Fake lepton background: events containing at least one fake lepton with/without fake tau. The objects which are incorrectly identified as leptons or non-prompt leptons are also called fake leptons.
- Fake τ_{had} background: events containing fake tau only, all leptons are prompt leptons. Some objects like jets can be misidentification or incorrectly reconstructed known as a fake τ_{had} .

Fake lepton background can originate from the decay of heavy-flavor hadrons (*b*- or *c*-quarks), internal conversions (arising from QED processes), external conversions (from high-energy photons interacting with detector material), and charge misidentification (“QmisID”), where at least one electron is reconstructed with the wrong charge. The primary sources of reducible background include $t\bar{t}$, Z+jets, and W+jets. The heavy-flavor hadrons decay, and fake τ_{had} has a dominant contribution to the reducible background, and dedicated CRs are constructed to improve the MC modeling. For fake leptons, a normalization factor is extracted by fitting CR to data through a fit that is applied to MC modeling. Whereas for fake τ_{had} background, a data-driven fake factor (FF) method is used to correct the MC modeling. Other reducible backgrounds, namely internal conversions, external conversions, and QmisID, have negligible contributions, and their contributions are taken directly from MC simulations.

Events containing both fake tau and fake lepton are categorized as fake lepton background. Events with only fake tau are categorized as fake τ_{had} background and estimated by the τ_{had} fake factor (FF) method [97]. The fake factor method has been chosen because the number of events in the signal region with only fake tau is small with respect to events containing at least one fake lepton; see bin 5 in Figure 3.9.

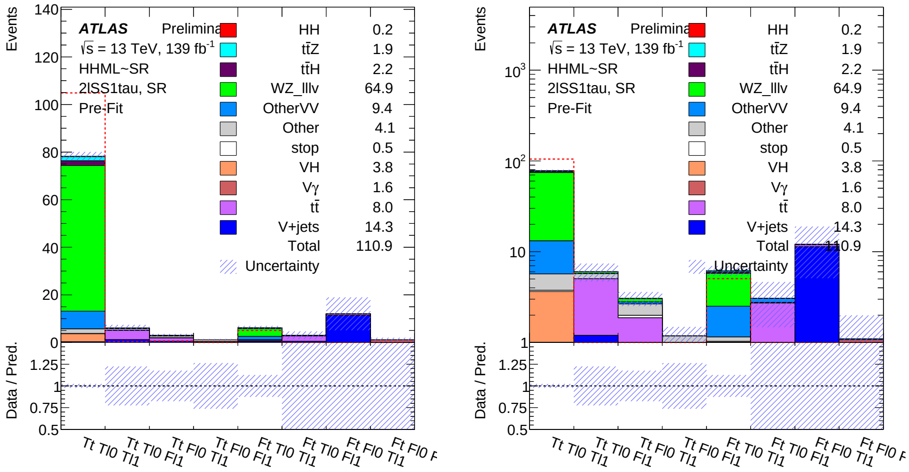

(a)

(b)

Figure 3.9: Types of fake backgrounds in the $2lSC1\tau_{\text{had}}$ channel. In the bin labels, ‘T’ denotes a prompt lepton, ‘F’ a fake lepton, and ‘t’, ‘l0’, ‘l1’ correspond to the hadronic tau, leading lepton, and subleading lepton, respectively. The category ‘otherVV’ includes all diboson processes except $WZ \to lll\nu$, such as WZ with other decay modes, ZZ, WW, and $VVjj$. Panel (b) shows the same data as (a) but with a logarithmic scale on the Y-axis.

3.6.1. Estimation of Heavy-Flavor Electrons Using a Fitting Function

As shown in Figure 3.11c and Table 3.7, the signal region contains heavy-flavor (HF) electron events with large statistical uncertainties. The BDT output distribution for these events peaks around 0.2, primarily due to the presence of only four MC raw events in this region. A raw event refers to an individual simulated event prior to the application of any corrections or normalizations. Each raw event is assigned a weight that accounts for the theoretical cross section, the integrated luminosity, and the efficiency of the event generator. These weights allow a limited number of simulated events to represent realistic event yields.

In this case, one of the four raw events was associated with an abnormally large weight, corresponding to a $W(\rightarrow \mu)+$jets event, which contributed disproportionately to the overall BDT distribution. Such large individual weights are considered unphysical, as they introduce significant variance and can distort both the total yield and the shape of the distribution, particularly in regions with limited statistics. As a result, the total estimated HF yield in the signal region was 6.92 ± 1.85, but this estimate is considered unreliable due to the impact of the overweighted event.

To mitigate this issue, the HF-electron control region described in Section 3.6.3, which offers improved statistics and more stable weighting, is employed to correct the BDT output in the signal region. The BDT developed in Section 3.4 is applied to the HF-e control region, and the resulting BDT response is shown in Figure 3.10. As expected, the low BDT output values correspond to background events.

First, the bin-by-bin ratio of the number of HF-e events in the signal region to those in the control region (as defined in Section 3.6.3) is computed. To enable a direct comparison, the BDT output distribution from the HF-e control region is rebinned to match the binning used in the signal region. A linear function, $f(x) = mx + c$, is subsequently fitted to this ratio. This fit is then used to reweight the estimated HF-e background in the signal

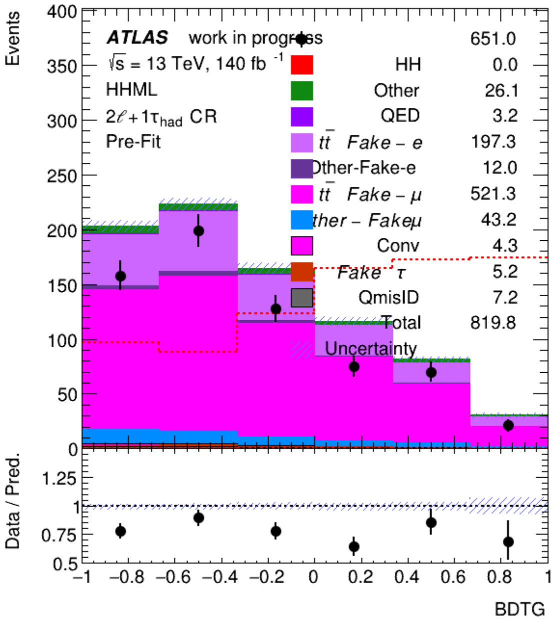

Figure 3.10: BDT output score distribution for the HF-e control region. The HH signal distribution is scaled to match the total background, and the expected HH yield is indicated in the legend.

region, providing an improved estimate of this contribution. The resulting reweighted HF-e background is shown in Figure 3.12. The fit yields the following parameters:

- $m = 0.0167 \pm 0.0074$
- $c = 0.0279 \pm 0.0254$

The chi-square per degree of freedom (χ^2/ndf) for this fit is 0.82 (2.45/3). The HF-e events in the signal region and control region are shown in Figure 3.11a and Figure 3.11c, respectively. The ratio of these two distributions along with the fitted function is illustrated in Figure 3.11b. Finally, the HF-e events in the control region are reweighted using the fit function, and the resulting distribution is shown in Figure 3.11d, along with the ratio of the reweighted to the original HF-e events.

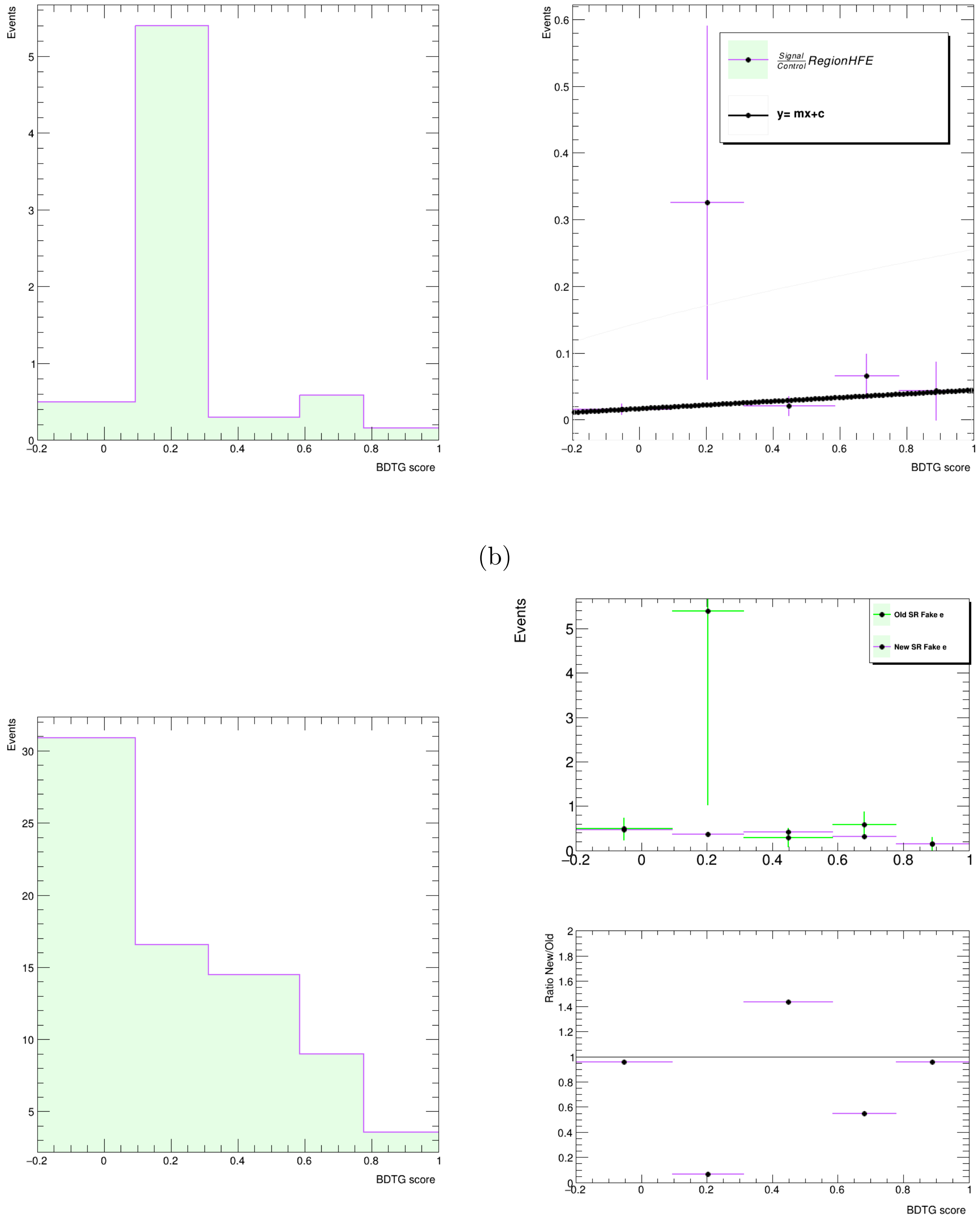

(a)

(b)

(c)

(d)

Figure 3.11: (a) BDT output distribution for HF-e events in the signal region without reweighting. (b) Ratio of HF-e events in the signal region to the control region, with the fitted linear function. (c) BDT output distribution for HF-e events in the control region using signal region binning. (d) BDT output for HF-e events in the signal region before and after reweighting, along with their ratio.

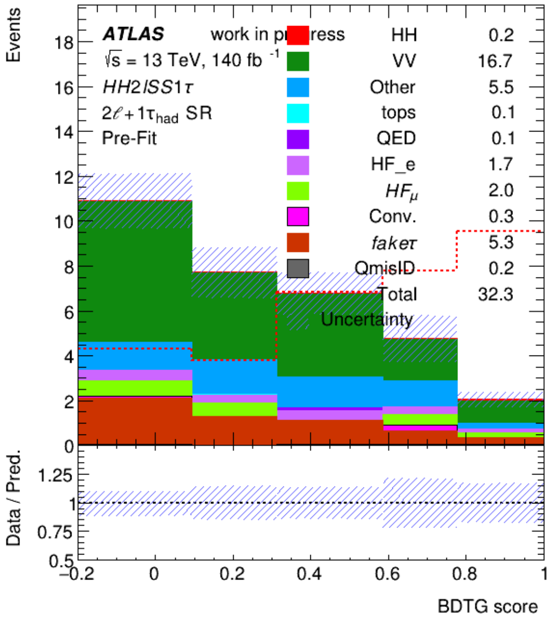

Figure 3.12: The pre-fit signal region distribution after reweighing HF electron samples using a liner fit from the ratio of HF electron in signal region to the control region.

3.6.1.1. *HF Electron Reweighting Uncertainty*

To evaluate the impact of the fitting uncertainties on the HF-e reweighting procedure, the covariance matrix of the fit parameters m and c is constructed, as shown in Table 3.8. The corresponding eigenvectors and eigenvalues are presented in Table 3.9.

Table 3.8: Correlation and Covariance Matrices for Parameters m and c

	Correlation Matrix		Covariance Matrix	
	c	m	c	m
c	1.0000	-0.3834	5.4905e-05	-7.2252e-05
m	-0.3834	1.0000	-7.2252e-05	0.0006470

Table 3.9: Eigenvalues and Eigenvectors of the Covariance Matrix for Parameters m and c

Eigenvalue	Eigenvectors	
4.6215e-05	-0.9928	-0.1194
6.5569e-04	-0.1194	0.9928

After obtaining the eigenvectors and eigenvalues in the eigenspace (f_m, f_c), variations of $\pm 1\sigma$ are applied to each eigenvector. These variations are then mapped back to the original (m, c) parameter space to construct modified fit functions. This procedure enables the estimation of systematic uncertainties associated with the HF-e reweighting. The resulting systematic variations are compared to the nominal reweighted HF-e distribution, as shown in Figure 3.13.

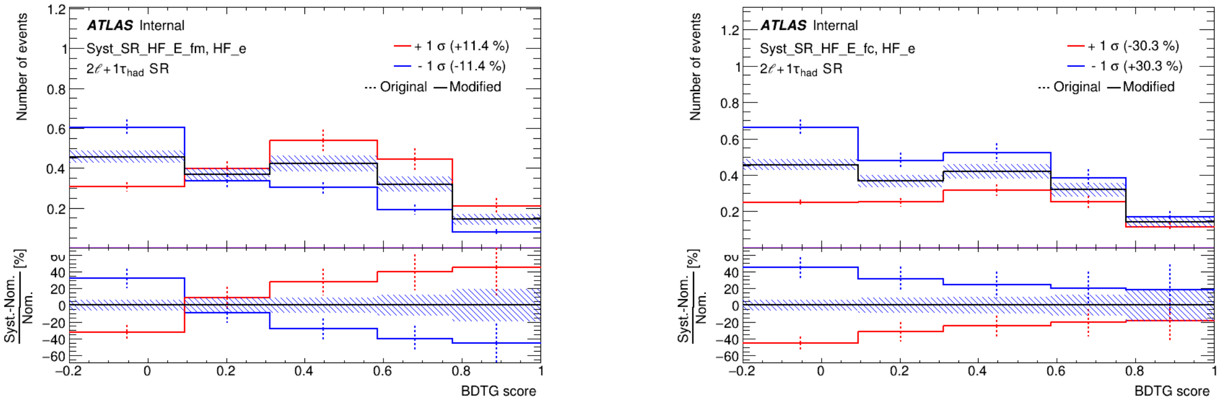

Figure 3.13: Systematic variations in the reweighted HF-e distribution in the signal region due to $\pm 1\sigma$ variations in the fit parameters.

3.6.2. Diboson background estimation

The irreducible diboson (VV) background poses a significant challenge, as its final states—typically involving three high-energy leptons, hadronic jets, or missing transverse energy—can closely resemble the signal. To validate the Monte Carlo (MC) modeling of this dominant background, a control region (CR) is defined by applying the same selection as in the signal region (Section 3.3) but inverting the BDT score requirement (BDT < -0.2).

This CR, which is enriched in VV events, is included in the fit, allowing the normalization of the diboson background to float freely.

The dominant contribution arises from fully leptonic diboson decays, accounting for approximately 48% of the total background in the signal region, as shown in Table 3.10. Additional contributions from $VV + jj$ and WZ processes amount to about 3% from the diboson background. Due to low statistics, the BDT distribution in the control region is binned into three intervals. The template fit is performed using this distribution to extract a normalization factor (NF_{VV}), which is then applied to the diboson MC prediction in the signal region.

- NF_{VV}: Normalization factor applied to prompt electrons from diboson decay

Table 3.10: Event yields for VV samples in $2lSC1\tau_{\text{had}}$ control region.The rest of the VV subprocesses are not participating in the VV background. The uncertainties are only statistical.

Process	Event yields
VV fully leptonic	40.38(117)
VVjj	1.83(5)
WW,ZZ,WZ	0.0

3.6.3. HF background estimation

The selection of at least one b-jet and removing the tight isolation working point for both light leptons, but other selections are the same as defined in Section 3.3, which provides CR enriched in HF background. This guarantees orthogonality with the SR as well. The leading and subleading lepton origination obtained from MCTruth Classifier are presented in Figure 3.14 for $e^{\pm}e^{\pm}$, $e^{\pm}\mu^{\pm}$, and $\mu^{\pm}\mu^{\pm}$, respectively. The multiple sources of fake leptons are dominated by undefined processes in leading leptons for the same flavor leptons. The additional top process plays the dominant role in the same flavor subleading fake light leptons. The fake leptons in $e^{\pm}\mu^{\pm}$ events are dominated by Dialitz and W boson processes for leading and subleading leptons, respectively. The HF background is further divided into HF electron and HF μ background estimation. The events with fake subleading leptons are more prevalent in the background, as seen in Figure 3.9. Thus, events with subleading electrons are categorized as HF electron CR, and events with subleading μ are categorized as HF μ CR. In addition, to accurately extract NF, the fake leptons have been measured in three dedicated regions, and three distributions are used in the fit to best extract the NFs to correct the MC. The number of bins and using two distributions to extract NF_e^{HF} were chosen so as to harmonize with other channels in the overall HH to multilepton search [51].

- ΔR_{ll} in $\mu e + ee$ channel with exactly 1 b-jet, to estimate NF_e^{HF}
- HT_{lep} in $\mu e + ee$ channel with at least 2 b-jets, to estimate NF_e^{HF}
- HT_{lep} in $e\mu + \mu\mu$ channel, to estimate NF_μ^{HF}

Using the template fit method, the normalization of the different ‘fakes’ contribution templates, as given by the Monte Carlo of all processes contributing to non-prompt lepton background, are left free-floating in a fit to data, and these normalization factors are used to correct the fakes Monte Carlo estimates. The two normalization factors are given as follows:

- NF_e^{HF}: Normalization factor applied to non-prompt electrons from heavy flavor decays
- NF_μ^{HF}: Normalization factor applied to non-prompt muons from heavy flavor decays

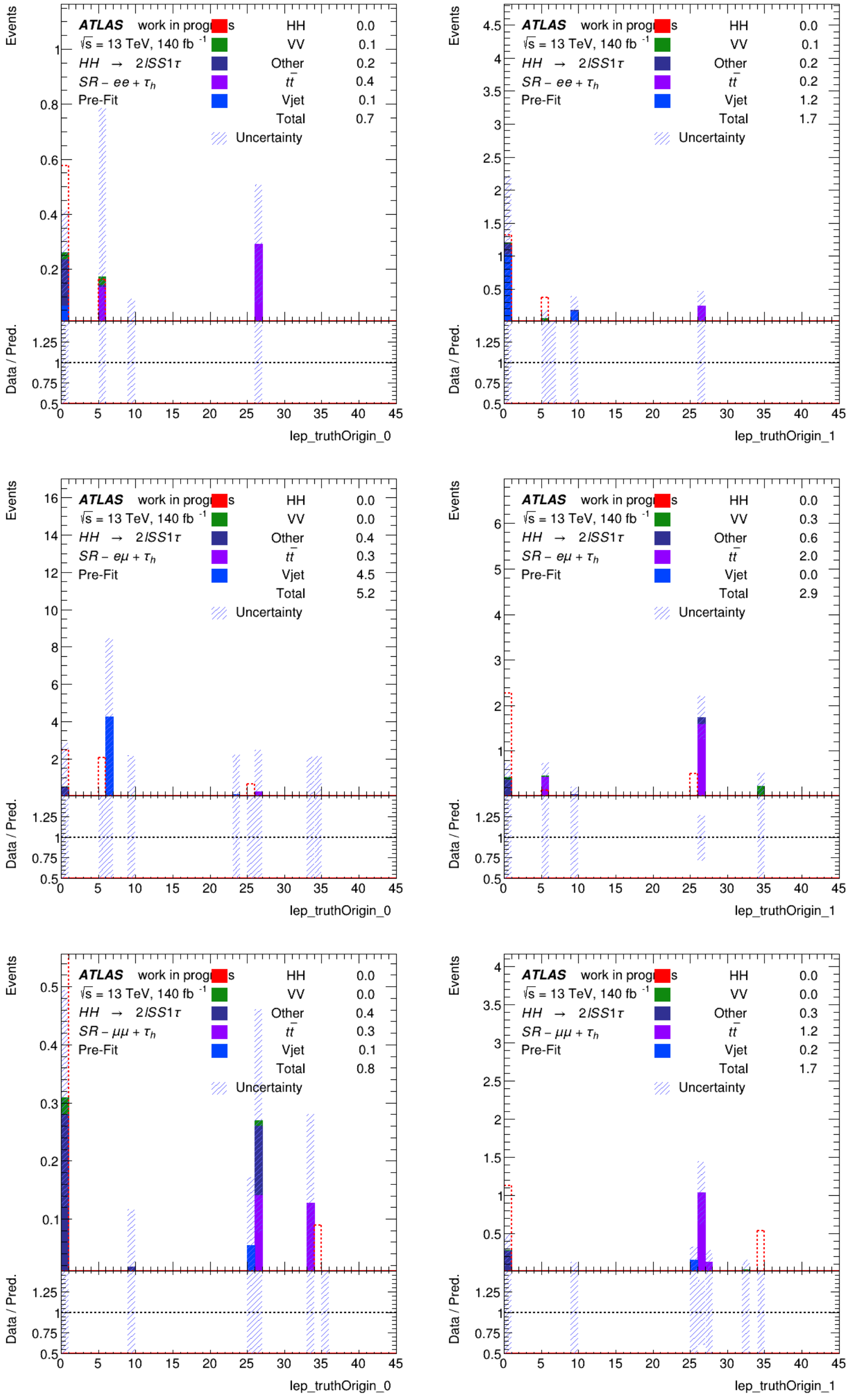

Figure 3.14: Origins for the leading and sub-leading fake leptons in same-sign dilepton channels: $e^{\pm}e^{\pm}$ (top), $e^{\pm}\mu^{\pm}$ (middle), and $\mu^{\pm}\mu^{\pm}$ (bottom). The definition of particle origin is as follows: Not defined = 0, Photon conversion = 5, Dalitz = 6, top = 10, W boson = 12, Z boson = 13, Higgs = 14, Charmed meson = 25, Bottom meson = 26, Bottom baryon = 33, Kaon decay = 35, Di-boson = 43, Z or heavy boson = 44. The HH signal distribution is scaled to the total background events and the expected HH yield is quoted in the legend.

3.6.4. Template Fit Method

The background from non-prompt light leptons arises primarily from semi-leptonic decays of heavy-flavor (HF) hadrons. To estimate this background, a dedicated template fit method has been developed [129]. This semi-data-driven method simultaneously addresses both non-prompt lepton and prompt diboson (VV) background estimations.

Within this approach, normalization factors for different background templates derived from MC simulations of all relevant processes are left free-floating in a fit to data. These normalization factors are subsequently applied to correct the MC predictions. The method leverages the truth-level classification of events in MC samples (such as $t\bar{t}$, $Z+$jets, $W+$jets, and single top) to define templates for different types of fake and prompt backgrounds.

Based on the MC truth labeling of non-prompt leptons, two dominant sources of fakes were identified:

- Heavy-flavor muons (HF_μ)
- Heavy-flavor electrons (HF_e)

Two separate normalization factors (NFs) are assigned to these components and determined via a fit to data. Further details are given in Section 3.6.3.

In addition to non-prompt backgrounds, the template fit is also used to constrain the normalization of prompt diboson (VV) backgrounds described in Section 3.6.2. Although VV processes are modeled using MC, their normalization is allowed to float in the fit to absorb potential discrepancies in production rates or detector modeling. A dedicated VV control region (CR) enriched in diboson events is used to extract the corresponding normalization factor. This treatment enhances the accuracy of the overall background modeling.

The three control regions used in the fit targeting VV, HF-e, and HF-μ backgrounds are shown in Figure 3.15 (pre-fit). The extracted normalization factors are summarized in Figure 3.30, and a comprehensive overview of the fit performance, including pre-fit and post-fit yields in all regions, is provided in Figure 3.32. The post-fit results demonstrate good agreement between the data and the MC model.

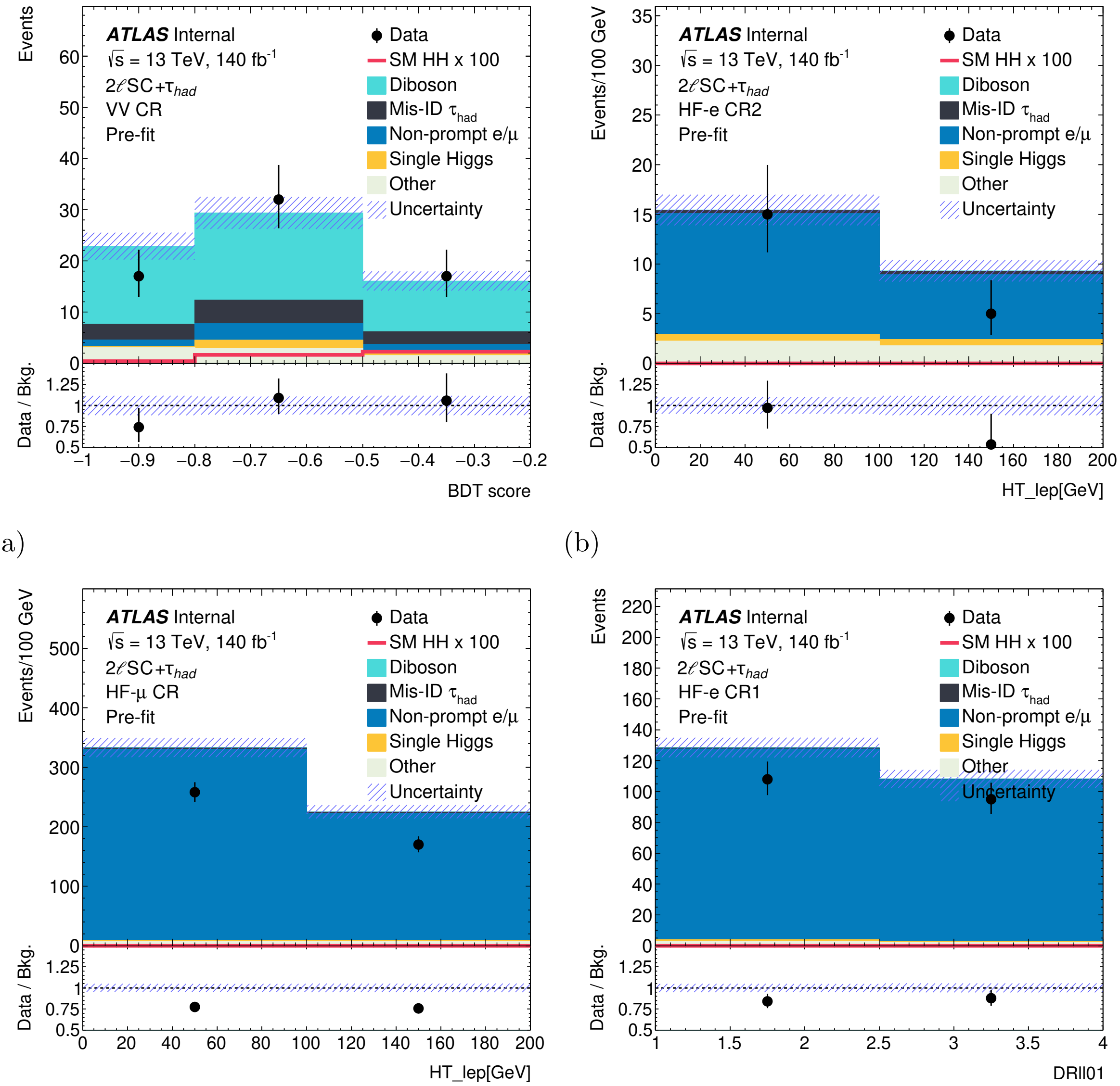

(a)

(b)

(c)

(d)

Figure 3.15: Pre-fit distributions in the template fit control regions. Top left: VV CR. Top right and bottom: HF-e and HF-μ control regions.

3.6.4.1. Template Fit Uncertainties

As the template fit relies on MC-based modeling, it is sensitive to theoretical and detector-related uncertainties, particularly in the modeling of non-prompt leptons. The associated systematic uncertainty is evaluated by comparing the shape of the fake lepton templates from MC with data-driven estimates.

These estimates are derived from dedicated control samples where the lepton isolation is loosened with two leptons requiring opposite charge, enhancing the fake contribution. The residual between data and non-fake MC backgrounds is taken as a proxy for the fake component. The ratio (Data − NonFakeBG)/FakeBG is used to derive a bin-by-bin uncertainty for each fake template. The HF-e and HF-μ templates are each assigned a dedicated shape uncertainty, treated as a single correlated nuisance parameter per template. These uncertainties are included in the final likelihood fit to account for potential mismodeling of the corresponding fake lepton backgrounds. While these uncertainties are incorporated, they are found to be subdominant in the overall uncertainty. The fake template shapes in control regions with modified selection criteria are shown in Figure 3.16 with the same variables and binning as described in Section 3.6.3. The numerical values of the HF uncertainties are summarized in Table 3.11. These systematic uncertainties were symmetrization where only one variation is provided and the opposite variation is added as a mirrored version of the provided variation.

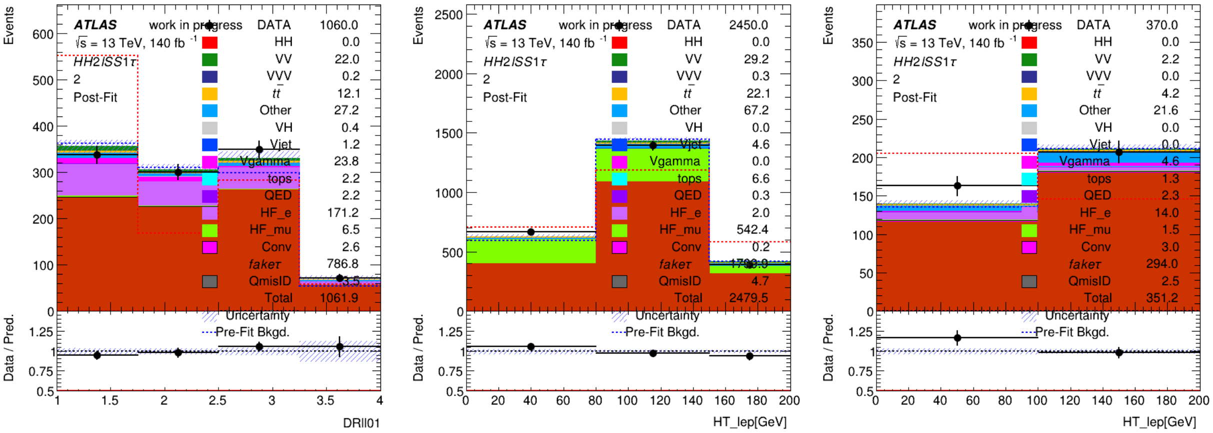

Figure 3.16: The OS light leptons Control Samples with removing isolation criteria: ΔR_{ll} in $\mu e + ee$ channel (left),HT_{lep} in $\mu e + ee$ channel (center) and HT_{lep} in $e\mu + \mu\mu$ channel (right). A part of systematic errors are included.

Table 3.11: Values of template fit uncertainties in the 2ℓSC$1\tau_{\text{had}}$ channel.

Uncertainties	BDT [-1, -0.741]	BDT [-0.741, -0.413]	BDT [-0.413, 0.162]	BDT [0.162, 1]
Heavy-flavor muons	25%	13%	15%	51%
Heavy-flavor electrons	83%	37%	47%	-35%

3.6.5. Fake τ_{had} Background Estimation

The 2ℓOS+$1\tau_{\text{had}}$ events are classified into a control region that is used to estimate the fake tau background in the 2ℓSS+$1\tau_{\text{had}}$ channel. The 2ℓOS+$1\tau_{\text{had}}$ channel is orthogonal to the 2ℓSS+$1\tau_{\text{had}}$ channel by construction because of the opposite charge requirement. There were two main reasons that the OSlltau region was re-categorized as a control region in this iteration of the analysis. First, this is a relatively high-statistics channel, but the expected significance is low due to the high background rates. Because of this, the channel is expected to contribute little to the overall HH sensitivity. The second reason can be seen in Figure 3.17, which shows the MCTruthClassifier type of tau in this region. As seen, the jet faking τ_{had} background makes up the vast majority of events in this region, and so 2ℓOS+$1\tau_{\text{had}}$ channel is used for the study of modeling of fake τ_{had} background.

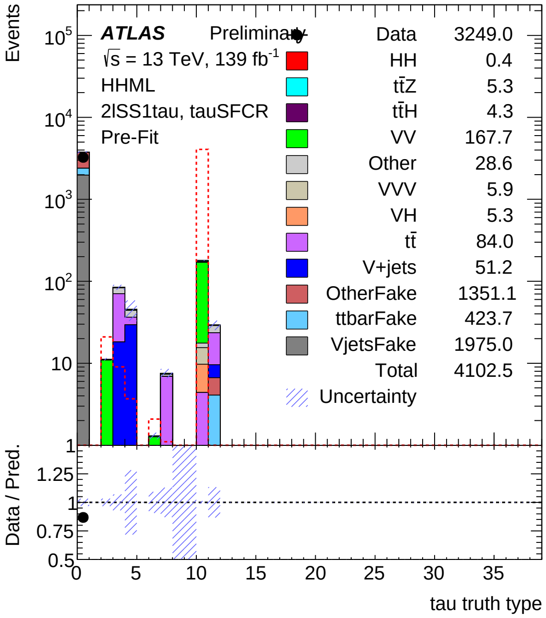

Figure 3.17: MCTruthClassifier type of tau in nominal scale factor CR. Bins: 0: unknown, 1-8: light leptons, 9-12: tau, 13-16: photon, 17-38: hadron, nentrino and other BSM particles. As seen in bin0, most of the Vjets faking tau samples lost its truth information.

3.6.5.1. Event Selection

All of the objects used in this section follows the selections outlined in Table 3.5 with following update to the event selection.

- Exactly two tight light leptons, passing the tight isolation working point, and with opposite electric charge.
- One hadronically decaying tau lepton, as defined in Table 3.5.

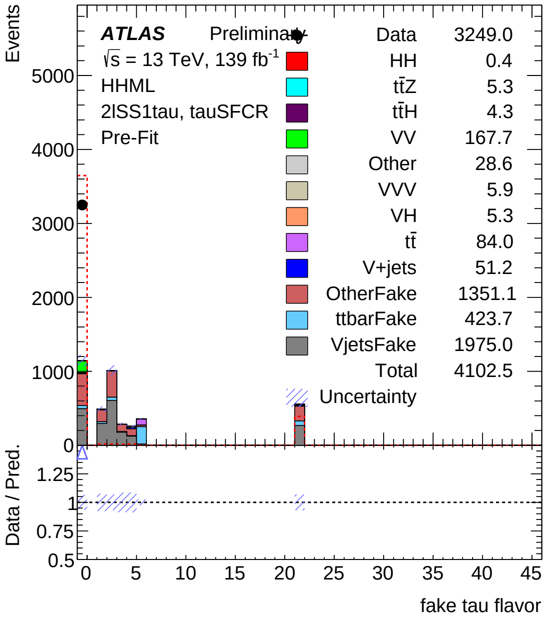

Figure 3.18: Truth jet flavor composition of fake tau in nominal CR. Bins: -1: unknown, 1-3: light, 4: c, 5: b, 6: t, 21: gluon.

- Veto placed on the invariant mass of opposite-sign same flavor lepton pairs falling in the Z mass window: $|M_{ll,OSSF} - 91.2GeV| > 10GeV$.
- Low invariant mass requirement on all opposite sign same flavor lepton pairs $|M_{ll,OSSF}| > 12GeV$.
- At least 2 jets and veto b-jet at the 77% WP.

This is defined as the nominal SF CR, which is the same as SR except for inverting the same sign charged requirement between the 2 light leptons and rejecting Z+jets events by excluding the Z mass (M_llOS) window. The motivation is that the OS requirement will gain us more statistics with respect to SR, at the same time rejecting massive Zjets contamination as expected.

3.6.5.2. Fake Tau SF Method

To estimate the fake-tau background, a data-driven (DD) scale factor (SF) is derived by comparing the normalization of fake-tau events in Monte Carlo (MC) to data. This SF is applied to each fake-tau event with a jet faking a tau individually to correct the normalization of the MC yield. Since the contribution coming from leptons faking taus is already scaled with a dedicated SF from the tau combined performance group [97], this contribution is not considered in the fake tau SF. Therefore, the fake tau SF is calculated as given in Equation 3.2 and applied using only events where the fake tau originates from a truth jet. The rate of jets faking taus in data is isolated by subtracting the real tau and fake tau from lepton contributions, and so these are the contributions to which the additional 50% systematic uncertainty is applied. Figure 3.19 shows data/MC comparison in nominal CR before applying the SF with the real tau and fake tau MC displayed separately. Because 1-prong tau is more likely to be faked by light quark jet while 3-prong tau by heavy flavor, the fake tau SF is derived and applied separately for 1- and 3-prong taus. The fake tau SF is derived as a function tau p_{T}. The binning was chosen to try and keep approximately similar statistics in each bin. The final SFs for 1- and 3-prong taus can be seen in Figure 3.20. This SF is applied to each fake-tau event individually to correct the normalization of the MC yield in the $2\ell\mathrm{SS}+1\tau_{\mathrm{had}}$ channel. The scale factors are derived as a function of τ p_{T} for 1- and 3-prong taus separately using Equation 3.2.

$$\text{Fake } \tau_{\text{had}} \text{ SF} = \frac{DD_{\text{Fakes}}}{MC_{\text{Fakes}}} = \frac{\text{Data} - MC_{\text{Real }\tau} - MC_{\text{FakeTauFromLepton}}}{MC_{\text{FakeTauFromJet}}} \tag{3.2}$$

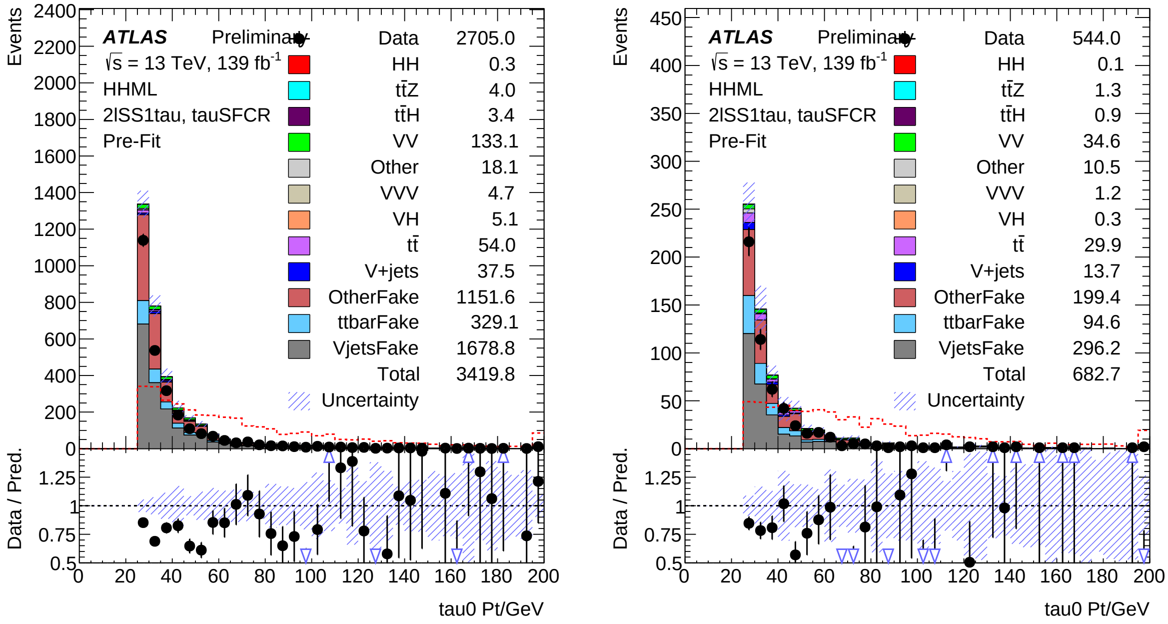

(a) (b)

Figure 3.19: $\tau_{\rm had}$ $p_{\rm T}$ distribution in nominal fake tau scale factor CR for (a) 1-prong and (b) 3-prong tau.

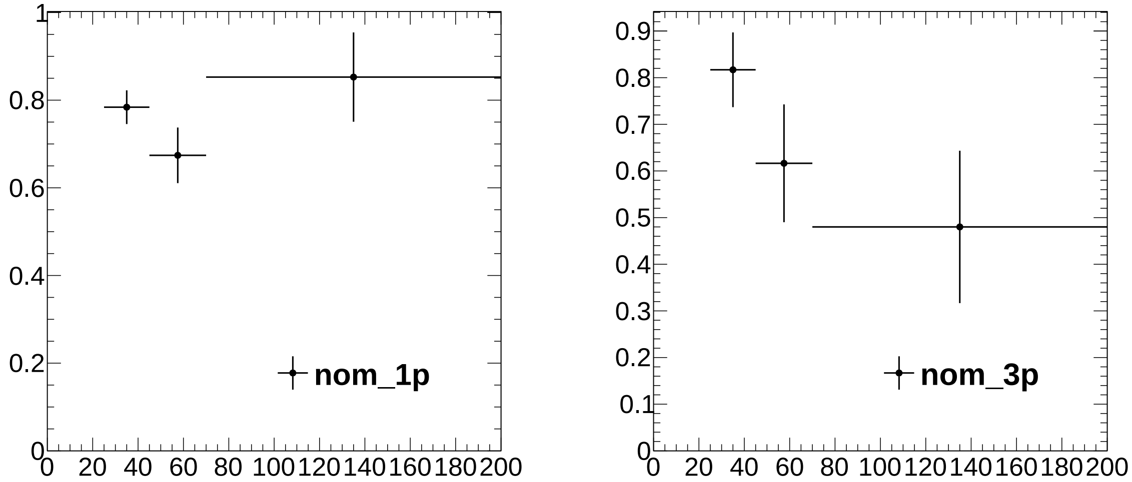

(a) (b)

Figure 3.20: Nominal fake tau scale factors for (a) 1-prong and (b) 3-prong tau.

3.6.5.3. Fake Tau Composition Systematics

Because of the composition differences between the $2\ell\text{OS}+1\tau_{\text{had}}$ control region and the other single tau signal region ($2\ell\text{SS}+1\tau_{\text{had}}$), additional control regions are defined to study the effect of modifying the fake tau composition and assign an additional uncertainty as a result. The differences in selections are described below, and the fake tau composition of these regions is shown in Figure 3.22.

- nominal CR : Described in Section 3.6.5.1.
- Z CR : Same as nominal CR except invert Z-veto.
- $t\bar{t}$ CR : Same as nominal CR except requiring one jets and one b-jet.

The final scale factors are presented in Figure 3.21 with statistical and systematic uncertainties. The measured scale factors in Zjets alternative CR are closer to nominal CR than in $t\bar{t}$ alternative CR, because truth jet flavor compositions of fake tau are both light flavor dominant in nominal and Zjets CR, while heavy flavor is important in $t\bar{t}$ CR, as shown in Figure 3.18 and Figure 3.22. In addition to the uncertainty of the truth of jet flavor composition of fake τ_{had} , a 50% uncertainty is assigned to real tau backgrounds subtracted in the numerator of SF and propagated as uncertainty of SF itself.

As seen in Figure 3.22, the TT-CR has a larger fraction of heavy quark jets, while the Z-CR has a larger fraction of light quark jets, indicating that these regions are working as intended. The only contribution that is not significantly varied is the fake taus originating from gluon jets. However, the contribution of these events is relatively constant between the nominal $2\ell\text{OS}+1\tau_{\text{had}}$ and other single tau regions, and so no additional uncertainty is applied. To quantify the systematic, the fake tau SFs were first derived in each of the 3 control regions separately. As in Figure 3.23, the values of SFs in each CR are shown, and the largest difference between the CRs is taken as the symmetric systematic uncertainty.

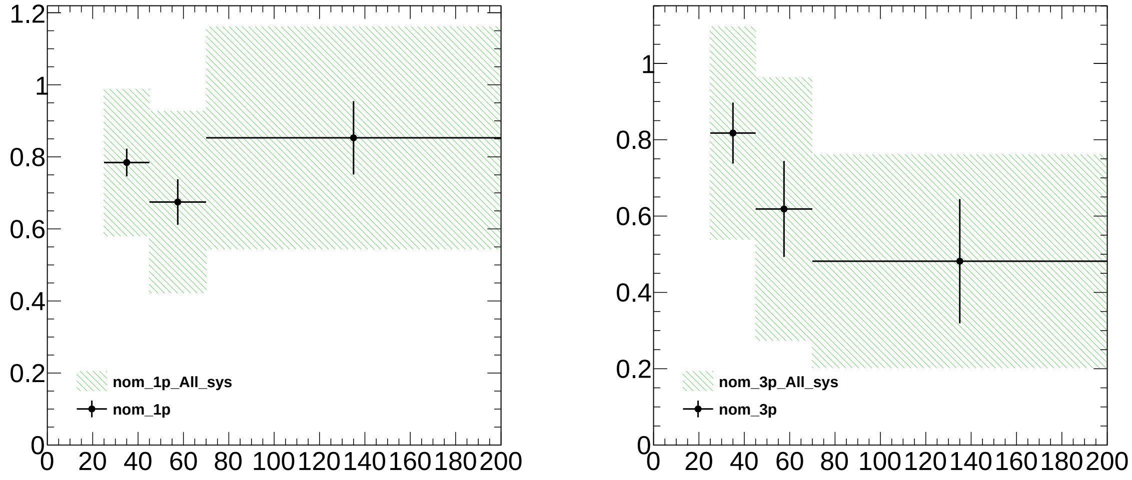

(a) (b)

Figure 3.21: Fake tau scale factors for (a) 1-prong and (b) 3-prong tau. Uncertainty band combines all SF systematic sources.

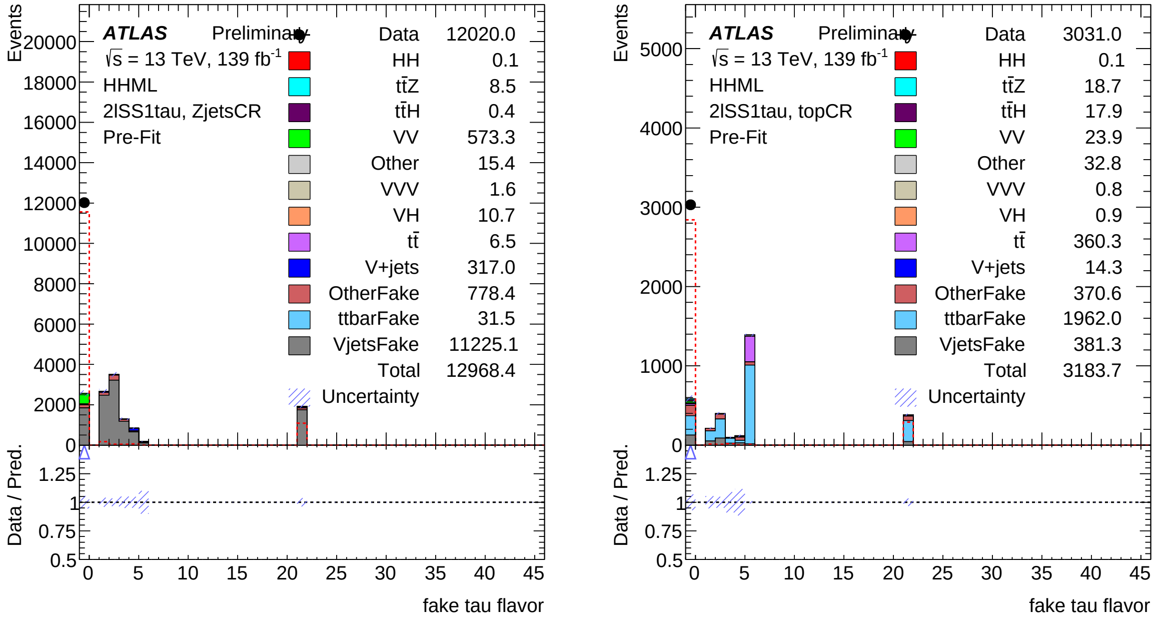

(a) (b)

Figure 3.22: Truth jet flavor composition of fake tau in alternative Zjets and $t\bar{t}$ CRs. Bins: -1: unknown, 1-3: light, 4: c, 5: b, 6: t, 21: gluon.

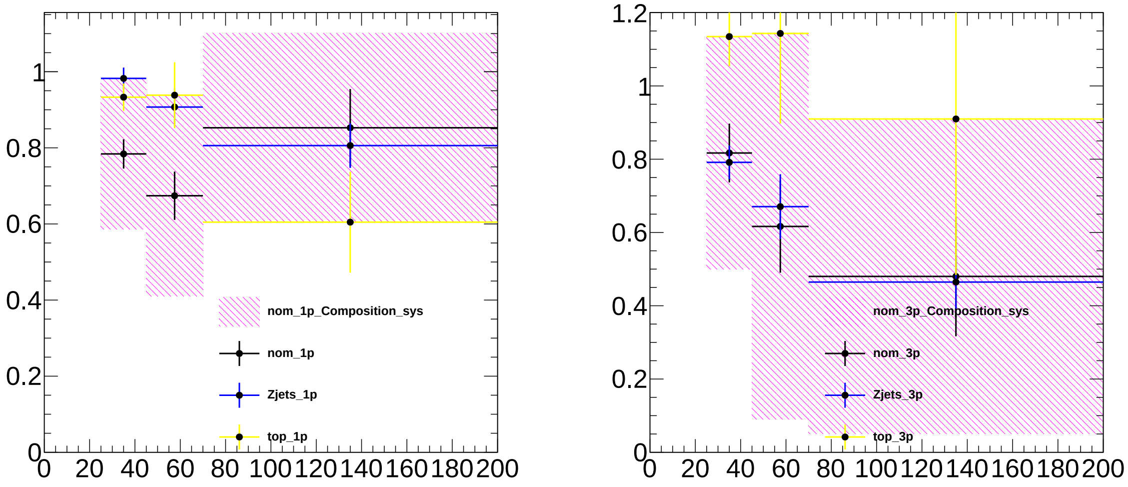

(a) (b)

Figure 3.23: Fake tau scale factors with difference in alternative CRs as composition systematic for (a) 1-prong and (b) 3-prong tau.

3.6.5.4. Fake Tau Numerator Systematic

As mentioned earlier, a systematic is assigned to the subtraction of events containing real taus and fake taus from leptons when calculating the fake tau SF. This consists of assigning a conservative estimate of 50% uncertainty to these events, resulting in a systematic on the fake tau SF for 1(3)-prong taus as in Figure 3.24.

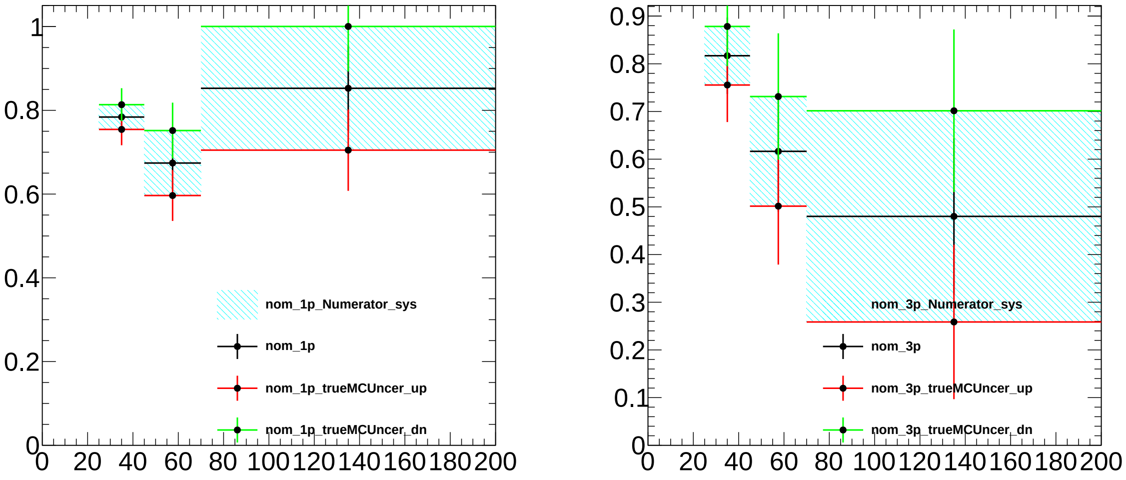

(a) (b)

Figure 3.24: Fake tau scale factors with true tau MC subtraction systematic for (a) 1-prong and (b) 3-prong tau.

3.6.5.5. Closure test

The closure test is performed by applying the fake tau SF back to the nominal $2\ell\mathrm{OS}+1\tau_{\mathrm{had}}$ control region. The closure test result can be seen in Figure 3.25, which shows good agreement of MC with data.

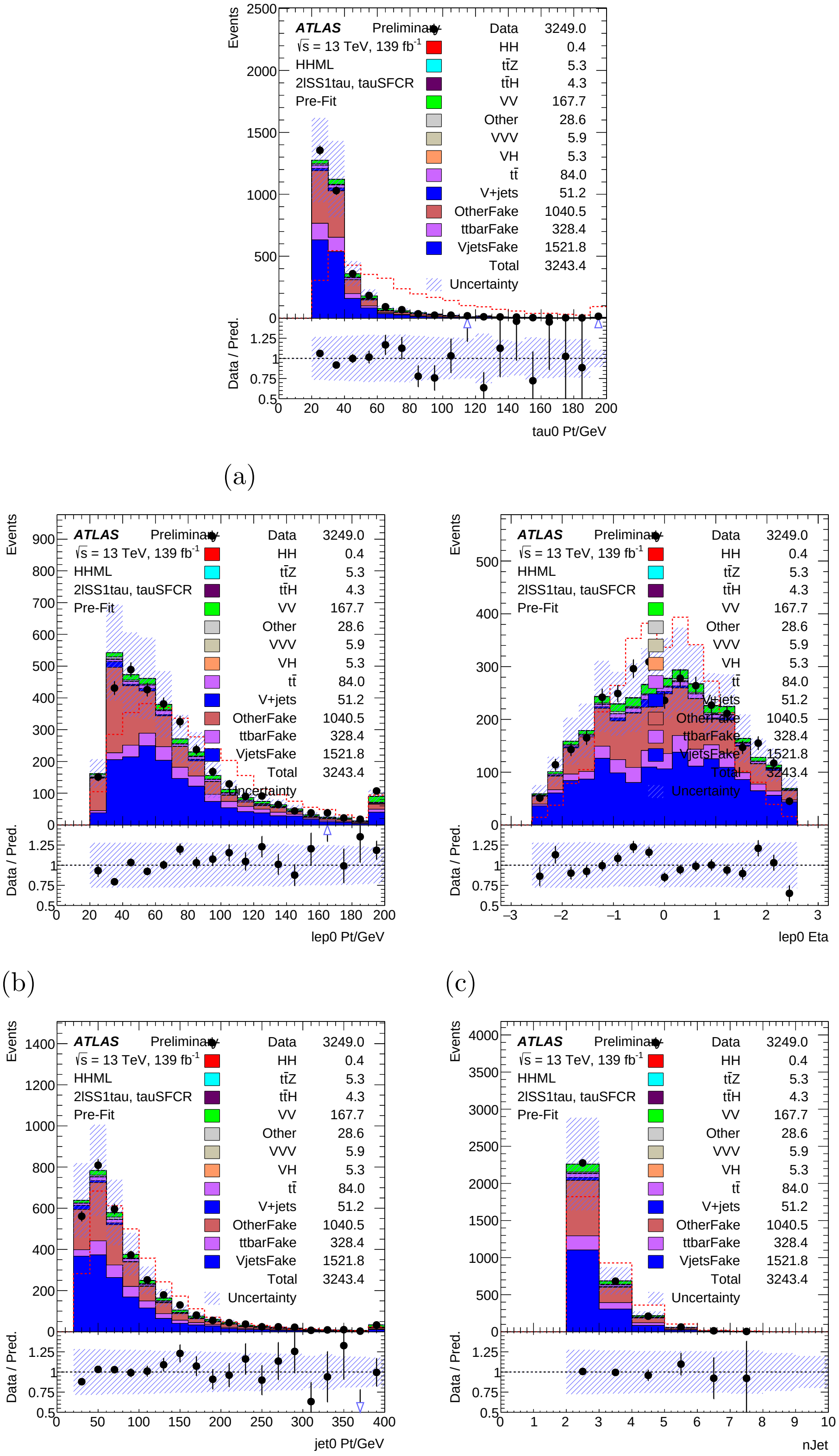

(a)

(b)

(c)

(d)

(e)

Figure 3.25: Showing closer test by applying the nominal SF back to nominal CR shown in (a) τ_{had} p_{T}, (b) leading lepton p_{T}, (c) leading lepton η, (d) leading jet p_{T}, (e) jet multiplicity. Uncertainty band includes SF systematics.

3.7. Validation Region

The validation region is a distinct subset of data used to assess the robustness and accuracy of the analysis. It enables an independent evaluation of the analysis strategy to determine whether the selection criteria and methodology perform effectively on data not used in the control or signal regions. In this study, the validation region is defined by inverting the jet multiplicity requirement, specifically requiring events to have at least two jets in addition to the preselection criteria described in Section 3.5. This definition ensures that the validation region remains statistically independent from both the signal and control regions. The distribution of the BDT output in the validation region, shown in Figure 3.26, demonstrates good agreement between MC predictions and data.

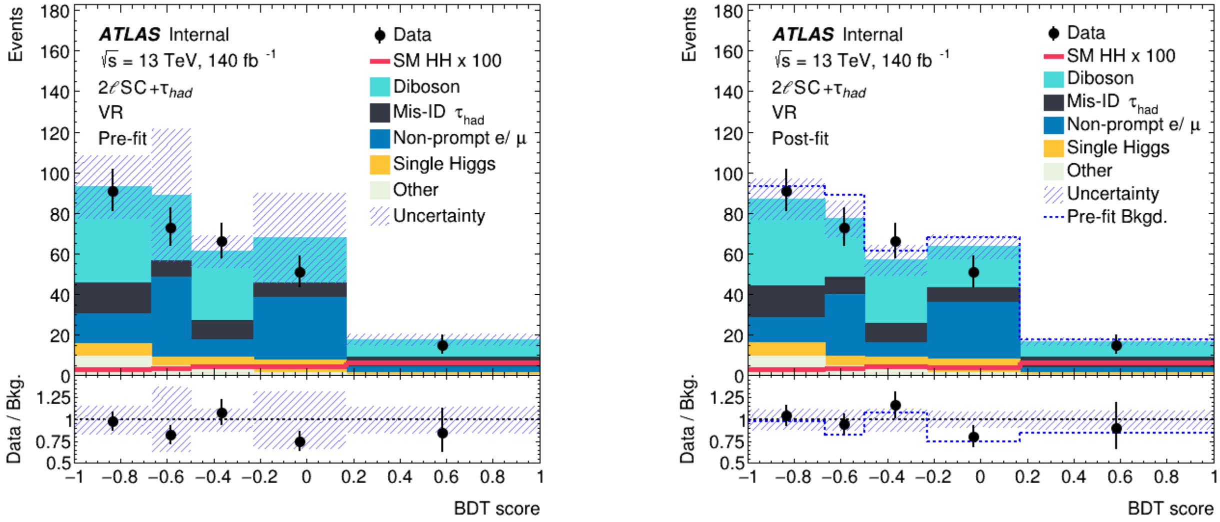

Figure 3.26: Distributions of the BDT output score in the validation region for $2\ell\mathrm{SC}1\tau_{\mathrm{had}}$ channel showing pre-fit (left) and post-fit (right). The non-prompt distribution is reweighted using a linear fit, see Section 3.6.1. The total pre-fit background (and its ratio to data) is also shown, as is the SM HH signal scaled up by a factor of 100. The uncertainty bands include all sources of statistical and systematic uncertainties in the background prediction.

3.8. Systematic Uncertainties

Uncertainties arising in this analysis can be broadly grouped into two groups: statistical and systematic. Statistical uncertainties arise from the random fluctuation or sampling from a limited number of samples. The uncertainty for simulating finite events for the MC samples is captured by MC statistical uncertainties. Moreover, it is common in high-energy physics to use histograms to represent the data. Histograms represent data by categorizing data into bins and measuring the frequency in each bin. For data, statistical uncertainties in each histogram bin are computed assuming Poisson statistics, i.e., the square root of the number of observed events in the bin. For Monte Carlo (MC) samples, where each event can carry a weight, the statistical uncertainty in each bin is computed as the square root of the sum of squared weights of the events in that bin.

Systematic uncertainties arise from limitations in detector performance, theoretical calculations, modeling, and other sources. Systematic uncertainties are biases that consistently affect the experiment in one direction, leading to deviations from the actual value. Thus, to account for such uncertainties, nuisance parameters are introduced which can be varied either up or down. These nuisances parameters can represent a single uncertainty, a component of an uncertainty, or a combination of related and partially correlated uncertainties. For the analysis, the total uncertainty is dominated by the statistical uncertainty in the number of data events in the signal region.

3.8.1. Experimental Uncertainties

Some of the major experimental uncertainties are briefly discussed below.

- **Luminosity:** The uncertainty of the combined Run-2 dataset is 0.83%. It is derived, following a methodology similar to that detailed in [103], from a preliminary calibration of the luminosity scale using x-y beam-separation scans performed from 2015 to 2018.

- **Pileup:** The pileup reweighing procedure is based on the comparing the average number of interactions per pp collision ($< \mu >$) in data to the corresponding simulated samples. The uncertainty on this method is obtained by varying the scaling factor in data.

- **Trigger:** Uncertainty on the efficiency of the electron and muon trigger selection are taken into account by using the related trigger scale factor. For leptonic channels SLT or DLT strategy triggers are used and the corresponded scale factor is applied [130,131].

- **Muons:** The uncertainties on efficiency, energy scale, resolution, object reconstruction, identification and isolation are taken into account.

- **Electrons:** Similarly to muons, the uncertainties on resolution, scale, efficiency, identification, isolation and so on were considered.

- **Taus:** Trigger, identification, reconstruction, and energy scale were considered.

- **Jets:** The jet energy scale (JES) calibration consists of several consecutive stages derived from a combination of MC-based methods and in situ techniques. The Jet energy resolution (JER) uncertainties is also considered [132].

- **Flavor Tagging:** A b-jet veto is applied at 77% tagging efficiency to be orthogonal with other HH analysis. The uncertainties arise from the efficiency to select jets containing a true b-hadron [133], charmed hadron [134], light hadrons [135] or coming from hadronically-decaying taus.

- **Missing Transverse Momentum:** The systematic variations are considered for the scale, parallel resolution, and perpendicular resolution of the soft term E_T^{miss}.

3.8.2. Theoretical Uncertainties

This subsection summarizes the sources of theoretical uncertainties considered in the analysis.

ggF HH: The inclusive gluon-gluon fusion (ggF) cross sections for Higgs boson pair production are taken from [136], assuming $m_H = 125$ GeV and central scale $\mu_0 = \mu_R = \mu_F = M_{HH}/2$. The recommended uncertainty components from the LHC Higgs Cross Section Working Group [137] include PDF and α_s (combined as "PDF + α_s"), scale, and m_{top} (combined as "Scale + m_{top}"). The corresponding relative uncertainties are:

- QCD scale: $^{+2.1\%}_{-4.9\%}$
- PDF + α_s: $\pm 3.0\%$
- m_{top} : $^{+4.0\%}_{-18.0\%}$

VBF HH: The cross-section uncertainties for vector boson fusion (VBF) Higgs pair production are taken from the same LHC-HH group recommendations [137].

For single SM Higgs boson production processes, the following theoretical uncertainties are considered:

ttH: Cross sections are calculated at next-to-leading order (NLO) in both QCD and electroweak (EW) accuracy. The uncertainties from QCD scale and PDF, as reported in CERN Yellow Report 4 [138], are:

- QCD scale: $^{+5.8\%}_{-9.2\%}$
- PDF + α_s: $\pm 3.6\%$

VH: For parton shower (PS) uncertainties:

- A 10% variation is applied for the 2ℓ and 3ℓ channels, following the VH, $H \to WW$ Run 2 analysis, which reports up to 8% PS uncertainty [139].
- A 40% uncertainty is used based on the $HH \to b\bar{b}\tau\tau$ analysis, which quotes up to 38% PS uncertainty for single Higgs VH production [43].

For other background processes, including $t\bar{t}V$, multiboson (VV, VVV), $V\gamma$, and rare processes (such as tZ, WtZ, $t\bar{t}WW$), the associated cross-sections and treatments of theoretical and data-driven uncertainties are summarized in Table 3.13.

Table 3.13: The background sample normalizations and their uncertainties used in the analysis.

Process	Precision order	Cross section central value	Cross section uncertainty	modeling uncertainty	Normalized to data
MC samples contributing to fake lepton templates					
$t\bar{t}$	NNLO+NNLL	832 pb	-	alternative MC	Yes
s-, t-channel single top	NLO	227 pb	-	-	Yes
Wt single top	NNLO approx	71.7 pb	-	-	Yes
$Z/\gamma^* \to l^+l^-$	NNLO	0.9751×SHERPA	-	-	
$W \to \ell\nu$	NNLO	0.9751×SHERPA	-	-	
MC samples of irreducible background processes					
$t\bar{t}W$	NLO	601 fb	-	alternative MC scale variations	Yes
$t\bar{t}t\bar{t}$	NLO	12 fb	20%	alternative MC	No
$t\bar{t}(Z/\gamma^* \to l^+l^-)$	NLO	839 fb	-	alternative MC scale variations	Yes
$t\bar{t}H$	NLO	507 fb	11%	alternative MC scale variations	No
WH	NLO	1102 fb		scale variations	No
ZH	NLO	601 fb		scale variations	No
VV, $qqVV$	NLO	SHERPA	-	10% (+LF jets), scale variations	Yes (+HF jets)
$t(Z/\gamma^*)$	LO	240 fb	5%	-	No
$t\bar{t}t$	LO	1.6 fb	50%	-	No
$tW(Z/\gamma^*)$	NLO	16 fb	50%	-	No
$t\bar{t}W^+W^-$	NLO	9.9 fb	50%	-	No
VVV	NLO	SHERPA	50%	-	No

3.9. Statistical Analysis

The statistical interpretation of the analysis is based on a binned likelihood function that incorporates both signal and control regions. The primary goal is to extract the cross section for $pp \to hh$ production. In a blinded analysis, the observed data event yields in the signal regions are taken from the sum of expected yields from MC for SM processes. The likelihood is defined as follows.

$$\mathcal{L} = \prod_{c \in \text{channels}} \prod_{b \in \text{bins}} \text{Poisson}(n^{\text{obs}}_{c,b} | n^{S}_{c,b}, n^{B}_{c,b}) \times \prod_{s \in \mathbb{S}} \mathcal{G}(0|\theta_s, 1), \tag{3.3}$$

Where, c stands for the channel index, b is the bin index for each channel. The Poisson terms Poisson are given by

$$\text{Poisson}(n^{\text{obs}}_{c,b} | n^{S}_{c,b}, n^{B}_{c,b}) = \frac{1}{n^{\text{obs}}_{c,b}!} \left(\mu * S_{c,b} + n^{B}_{c,b}\right)^{n^{\text{obs}}_{c,b}} \exp^{-\left(\mu * S_{c,b} + n^{B}_{c,b}\right)} \tag{3.4}$$

Where the number of events observed in each bin is marked as $n^{\text{obs}}_{c,b}$, and the expected numbers of signal and background in the corresponding bin are $n^{S}_{c,b}$ and $n^{B}_{c,b}$, respectively. The Parameter-of-interest (POI) μ is the signal strength, which is shared among different bins and channels. To represent the nuisance parameter (NP) constraint terms, a Gaussian function, $\mathcal{G}(0|\theta_s, 1)$, is considered, where θ_s is the NP term.

3.9.1. Profile Likelihood Ratio Test

To evaluate the consistency of the data with different values of μ, the profile likelihood ratio is used. It compares the global maximum likelihood to the conditional likelihood where μ is fixed:

$$\lambda(\mu) = -2 \ln \left(\frac{\mathcal{L}(\mu, \hat{\boldsymbol{\theta}}(\mu))}{\mathcal{L}(\hat{\mu}, \hat{\boldsymbol{\theta}})} \right), \tag{3.5}$$

Where, $\hat{\mu}$ and $\hat{\boldsymbol{\theta}}$ are the maximum likelihood estimators, and $\hat{\boldsymbol{\theta}}(\mu)$ is the profile of the nuisance parameters for a fixed μ.

3.9.2. Test statistic

The hypothesis testing relies on the profile likelihood ratio, denoted by $\tilde{q}_\mu$, which compares the likelihood for a fixed signal strength μ against the best-fit hypothesis. The test statistic is defined based on the profiled likelihood ratio,

$$\tilde{\lambda}(\mu) = \begin{cases} \dfrac{\mathcal{L}(\mu, \hat{\boldsymbol{\theta}}(\mu))}{\mathcal{L}(\hat{\mu}, \hat{\boldsymbol{\theta}})} & \text{if } \hat{\mu} \geq 0, \\ \dfrac{\mathcal{L}(\mu, \hat{\boldsymbol{\theta}}(\mu))}{\mathcal{L}(0, \hat{\boldsymbol{\theta}}(0))} & \text{if } \hat{\mu} < 0, \end{cases} \tag{3.6}$$

Where $\hat{\mu}$ and $\hat{\boldsymbol{\theta}}$ are the unconditional maximum likelihood estimates (MLEs) for the signal strength and nuisance parameters, respectively. The term $\hat{\boldsymbol{\theta}}(\mu)$ denotes the conditional MLE of the nuisance parameters for a fixed value of μ.

The test statistic $\tilde{q}_\mu$ is then defined as:

$$\tilde{q}_\mu = \begin{cases} -2 \ln \dfrac{\mathcal{L}(\mu, \hat{\boldsymbol{\theta}}(\mu))}{\mathcal{L}(0, \hat{\boldsymbol{\theta}}(0))} & \text{if } \hat{\mu} < 0, \\ -2 \ln \dfrac{\mathcal{L}(\mu, \hat{\boldsymbol{\theta}}(\mu))}{\mathcal{L}(\hat{\mu}, \hat{\boldsymbol{\theta}})} & \text{if } 0 \leq \hat{\mu} \leq \mu, \\ 0 & \text{if } \hat{\mu} > \mu. \end{cases} \tag{3.7}$$

Upper limits on the non-resonant Higgs boson pair production cross section are derived at the 95% confidence level using the CL_s method and the asymptotic approximation as described in Ref. [140].

This one-sided test statistic ensures that upward fluctuations (i.e., $\mu < \hat{\mu}$) do not contribute to the exclusion power.

3.9.3. p-values and the $\mathrm{CL_s}$ Method

The p-value associated with a given hypothesis quantifies the probability of obtaining a result at least as extreme as the observed one. For the test statistic $\tilde{q}_\mu$, the p-value is defined as:

$$p_\mu = \int_{\tilde{q}_\mu^{\mathrm{obs}}}^{\infty} f(\tilde{q}_\mu \mid \mu)\, d\tilde{q}_\mu, \tag{3.8}$$

where $f(\tilde{q}_\mu \mid \mu)$ is the probability density function under the signal hypothesis with strength μ. To set upper limits, the $\mathrm{CL_s}$ method is used:

$$\mathrm{CL}_s = \frac{p_{s+b}}{p_b}, \tag{3.9}$$

where p_{s+b} and p_b are the p-values for the signal-plus-background and background-only hypotheses, respectively:

$$p_{s+b} = \int_{\tilde{q}_\mu^{\mathrm{obs}}}^{\infty} f(\tilde{q}_\mu \mid \mu = 1)\, d\tilde{q}_\mu, \tag{3.10}$$

$$p_b = \int_{\tilde{q}_\mu^{\mathrm{obs}}}^{\infty} f(\tilde{q}_\mu \mid \mu = 0)\, d\tilde{q}_\mu. \tag{3.11}$$

A signal hypothesis is excluded at 95% confidence level if $\mathrm{CL}_s < 0.05$.

3.9.4. Significance of Observed Excess

The significance of an observed deviation from the background-only hypothesis is expressed in terms of standard deviations (Z-score) of a normal distribution:

$$Z = \Phi^{-1}(1 - p), \tag{3.12}$$

where Φ^{-1} is the inverse cumulative distribution function of the standard normal distribution. In particle physics, evidence and discovery of a new process are traditionally defined as:

- $Z = 3$: evidence for a signal ($p < 1.35 \times 10^{-3}$),
- $Z = 5$: discovery of a signal ($p < 2.87 \times 10^{-7}$).

3.10. Results

A profile likelihood fit is performed in the signal and control regions using the available dataset, following the methodology outlined in Section 3.9. The BDT output distribution is employed as the final discriminant in the fit. To avoid biases, the analysis was initially blinded; i.e., data from the signal region were excluded during the early stages. This ensures the analysis is conducted objectively, without influence from preliminary observations. During the blinded phase, the templates were fitted to data in the control regions only. The normalization factors (NFs) extracted from this blinded fit were incorporated into the full fit model to evaluate the expected sensitivity using the Asimov dataset, a simulated dataset based on expected signal and background contributions. After unblinding, a simultaneous fit including the signal region was performed, allowing the normalization factors to be derived from all relevant regions.

Systematic uncertainties are incorporated as nuisance parameters (NPs). Object-related NPs are treated according to the recommendations from the respective performance groups, as discussed in Section 3.8. The NPs with negligible impact are excluded specifically, those for which normalization or shape variations remain below 1% across all bins. The pulls of the retained nuisance parameters are shown in Figure 3.28. The absence of significant pulls indicates good agreement between the post-fit and nominal values. The impact of each NP on the fitted signal strength is assessed by varying the NP by its uncertainty while keeping all other parameters free. Figure 3.29 presents the ranking of NPs by their impact on the signal strength. The dominant uncertainty arises from the bin-by-bin statistical fluctuations in the BDT discriminant, indicating that limited data statistics are the main constraint on the measurement precision. The unblinded post-fit and pre-fit BDT distributions in the signal region are shown in Figure 3.27.

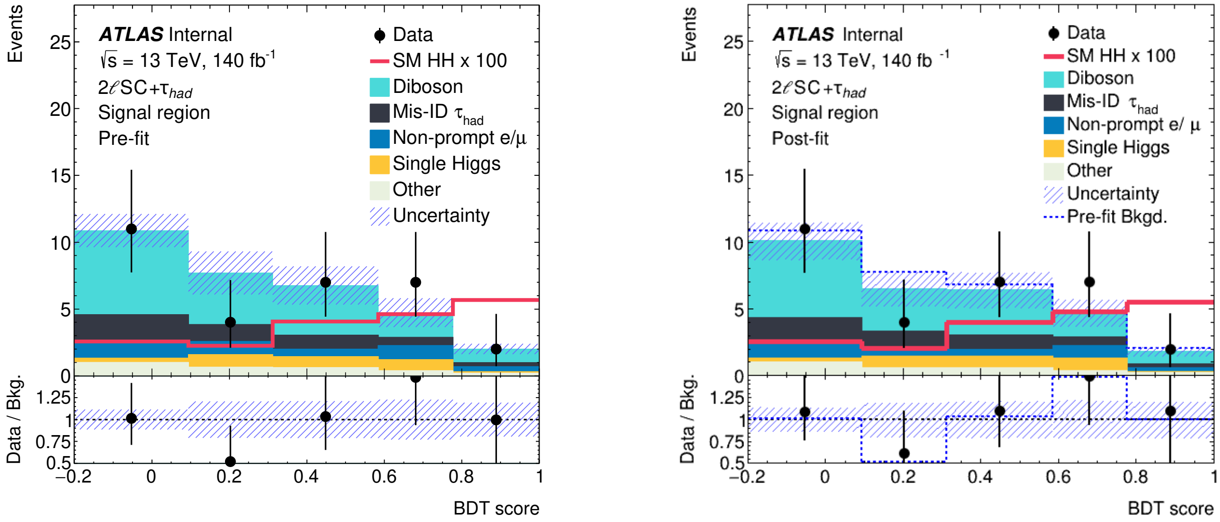

Figure 3.27: Distributions of the BDT output score in the signal region for $2\ell SC1\tau_{\mathrm{had}}$ channel before (left) and after (right) background fit. The non-prompt distribution is reweighted using a linear fit, see Section 3.6.1. The total pre-fit background (and its ratio to data) is also shown, as is the SM HH signal scaled up by a factor of 100. The uncertainty bands include all sources of statistical and systematic uncertainties in the background prediction.

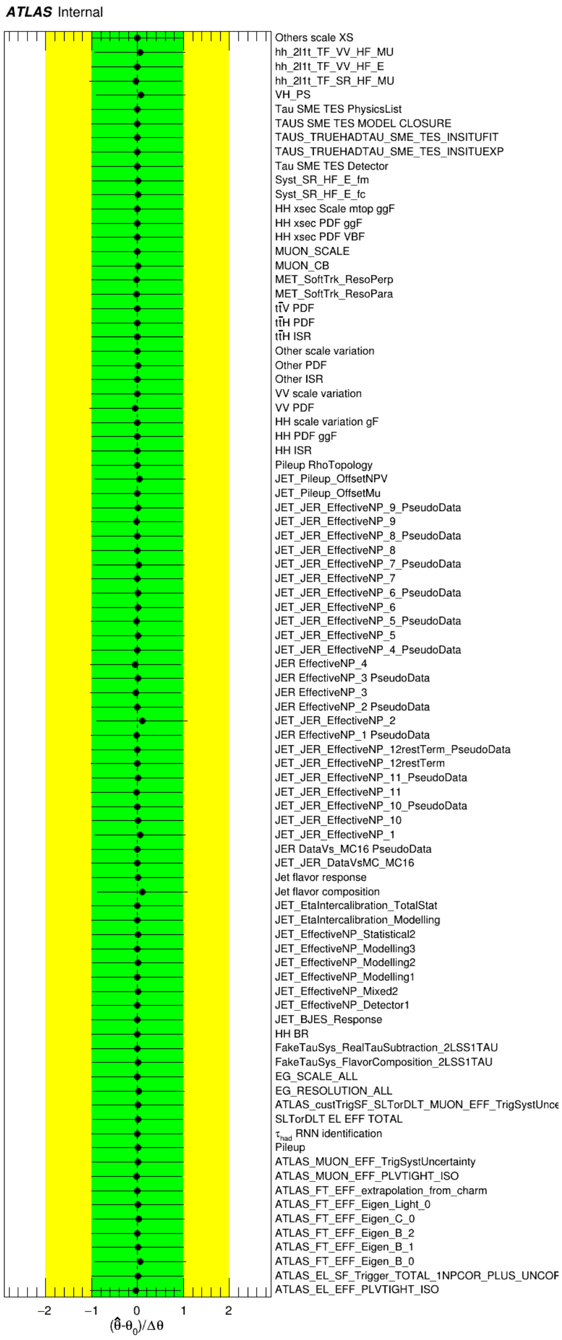

Figure 3.28: Pulls and constraints of nuisance parameters.

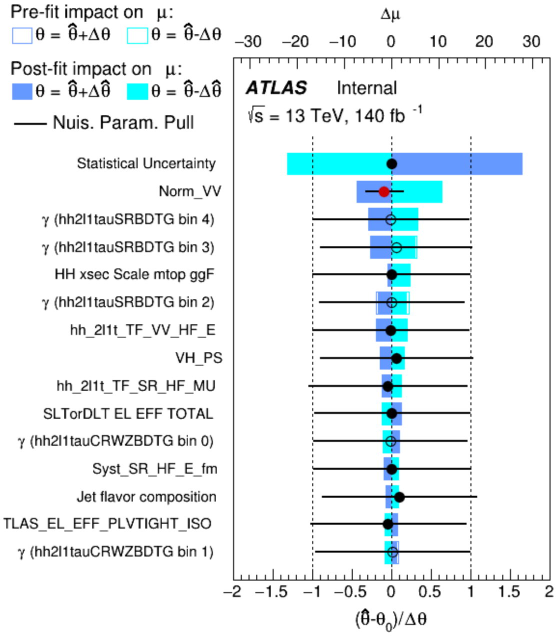

Figure 3.29: Impact of nuisance parameters on the signal strength in the signal region.

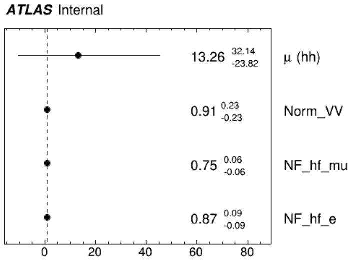

Figure 3.30: Fitted normalization factors for template components, including signal strength. The signal strength of non-resonant SM HH production is defined as the ratio of the signal cross-section to the SM prediction.

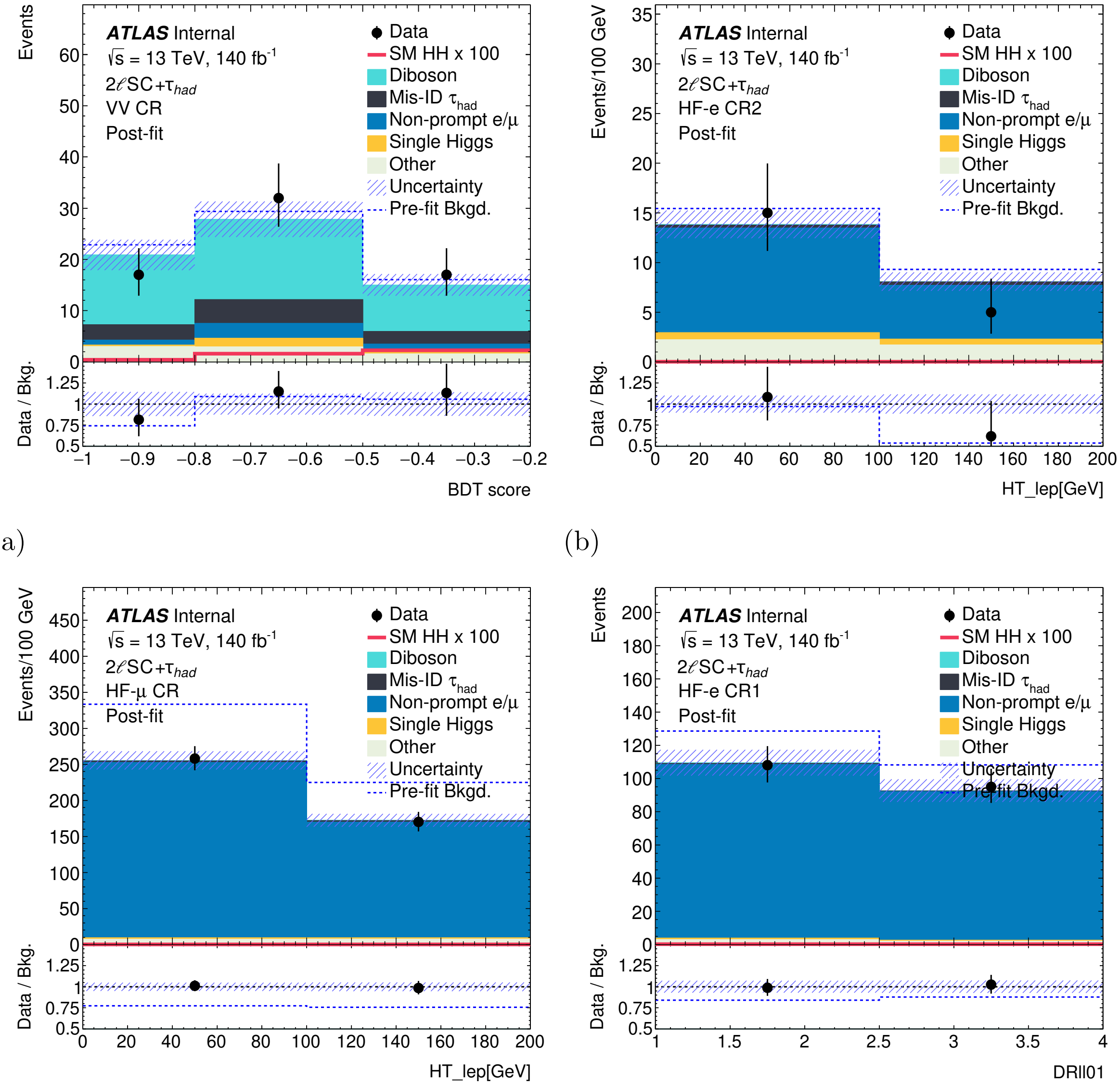

(a)

(b)

(c)

(d)

Figure 3.31: Post-fit distributions in the template fit control regions. Top left: VV CR. Top right and bottom: HF-e and HF-μ control regions.

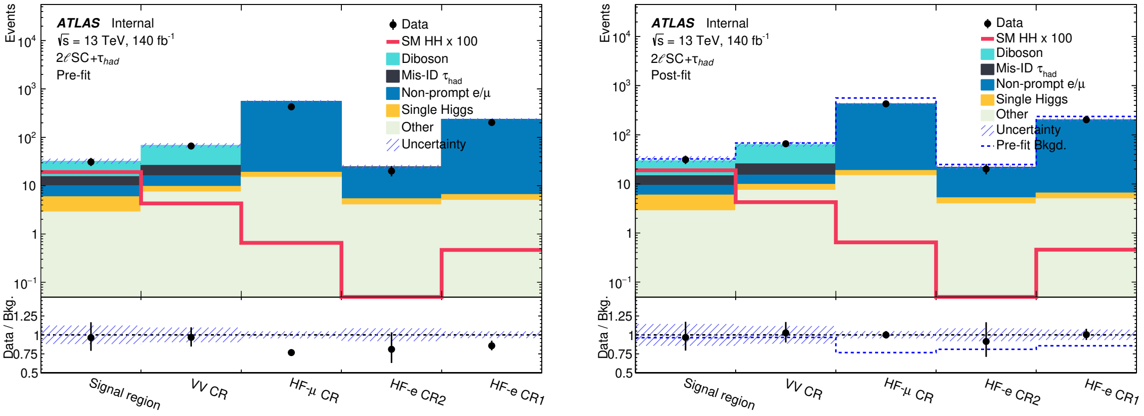

(a) (b)

Figure 3.32: (a) Pre-fit and (b) post-fit yield summary in signal and control regions.

An observed (expected) 95% confidence level (CL) upper limit on the signal strength of 82.94 (64.78) times the Standard Model (SM) prediction is obtained, as shown in Table 3.14 (see also Section 3.9.3 for CLs method). The expected limit is derived under the background-only hypothesis, where the signal strength is set to zero, implying no injected signal. The observed limit indicates that the data in the $2\ell\mathrm{SC}1\tau_{\mathrm{had}}$ channel is consistent with a signal strength up to 82.94 times the SM expectation. This implies that any potential signal contribution above this threshold would be incompatible with the observed data. The range of expected upper limits, from 28.61 to 176.2 times the SM prediction, reflects the analysis sensitivity and the statistical fluctuations expected under the background-only scenario.

Table 3.14: Expected and observed 95% CL exclusion limit on the signal strength in $2lSC1\tau_{had}$ final state.

	-2σ	-1σ	Expected	$+1\sigma$	$+2\sigma$	Observed
$\sigma_{HH}/\sigma_{HH}^{SM}$	28.61	41.24	64.78	106.7	176.2	82.94

In addition to the 95% CL upper limits on the SM non-resonant HH production cross-section results, the limits as a function of the Higgs self-coupling parameter κ_λ are also determined. This parameter is unity in the SM, and in order to evaluate the sensitivity to BSM scenarios, a reweighting from the nominal SM signal samples ($\kappa_\lambda = 1$) to a signal representing different κ_λ values. The constraints on the Higgs boson self-coupling strength, expressed as 68% and 95% CL intervals, are determined using a profile-likelihood-ratio, where the POIs in α is the coupling strength modifier κ_λ. The same signal and control regions, as defined in this thesis, are used for these results. This analysis does not target VBF production with a dedicated strategy. However, a similar likelihood can be used to extract a best-fit value for κ_{2V} with its 68% and 95% confidence intervals as well. In this case the SM scenario is assumed with $\kappa_\lambda = 1$, and the same signal and control regions are used as before. The 2ℓSS+1τ channel provides the observed (expected) 68% CL and 95% CL constraints on κ_λ correspond to $[-9.4, 15.2]$ and $[-15.4, 21.1]$ ($[-12.7, 18.6]$ and $[-18.3, 24.1]$), respectively. The observed (expected) 68% CL and 95% CL constraints on κ_{2V} correspond to $[-5.3, 7.5]$ and $[-8.4, 10.6]$ ($[-7.2, 9.3]$ and $[-10.0, 12.2]$), respectively.

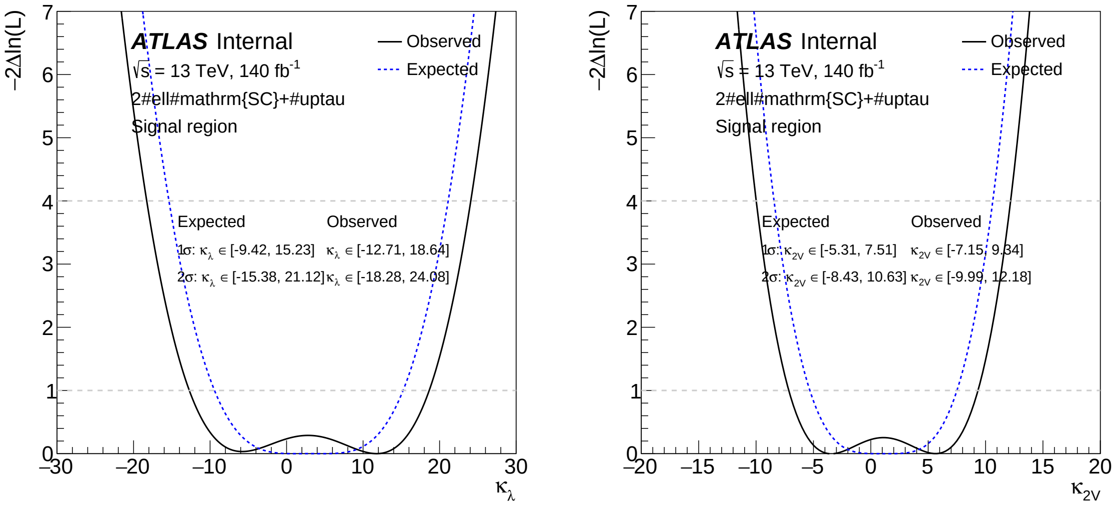

Figure 3.33: Expected (dashed line) and observed (solid line) likelihood-ratio scans as a function of κ_λ (left) and κ_{2V} (right) for the 2ℓSS+1τ channel. The intersection of the solid curves and the horizontal dashed lines indicate the 68% and 95% confidence intervals.

Chapter 4

Conclusion

In this thesis, a search for Higgs boson pair production in the final state with two same-sign leptons and one hadronically decaying tau lepton is presented. The analysis is based on proton-proton collision data at a center-of-mass energy of $\sqrt{s} = 13$ TeV, collected by the ATLAS detector during Run 2 of the Large Hadron Collider (LHC), corresponding to an integrated luminosity of 140 fb^{-1}.

No significant excess above the Standard Model (SM) background expectation is observed. Consequently, upper limits are set on the non-resonant SM Higgs boson pair production cross section. An observed (expected) 95% confidence level (CL) upper limit on the signal strength of 82.94 (64.78) times the SM prediction is derived. The analysis is statistically limited due to the low number of expected signal events. However, when combined with other multi-lepton channels, a more stringent constraint on the SM HH production cross section is achieved, as seen in Figure 4.1.

The significance of this result lies in its contribution to the broader ATLAS program to search for non-resonant Higgs boson pair production. The combination of various channels, including the $2\ell\text{SC}1\tau_{\text{had}}$ final state studied here, enhances the overall sensitivity to the Higgs self-coupling parameter. This is particularly crucial for the Run3 and High-Luminosity LHC (HL-LHC) phases, where improving sensitivity to di-Higgs production is a key goal.

Beyond the immediate results, this analysis opens a novel avenue for future exploration. The study of final states with two same-sign leptons and a hadronic tau highlights the potential of previously underexplored channels. Continued development of the tools and techniques presented in this thesis will be instrumental in future searches, aiding the physics community in its pursuit of observing SM di-Higgs production and probing the shape of the Higgs potential.

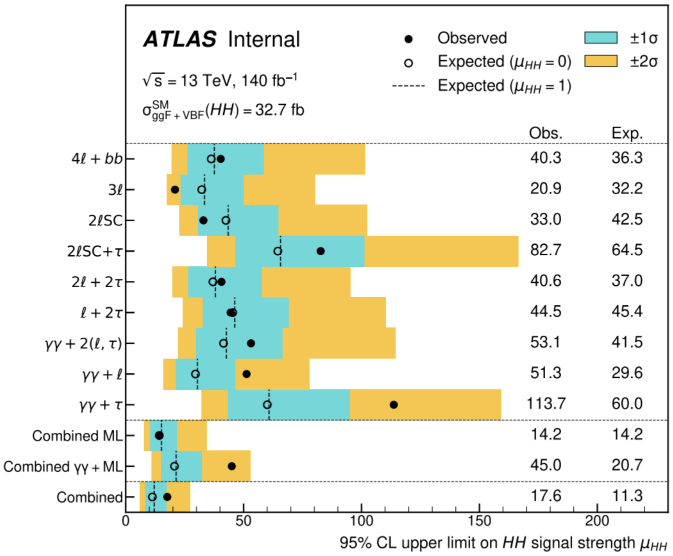

Figure 4.1: Observed (filled circles) and expected (open circles) 95% CL upper limits on the signal strength for HH production in the background-only (μHH $= 0$) hypothesis. The dashed lines indicate the expected 95% CL upper limits on μHH in the SM hypothesis (μHH $= 1$). The inner and outer bands indicate the $\pm 1\sigma$ and $\pm 2\sigma$ variations on the expected limit under the background-only hypothesis due to statistical and systematic uncertainties, respectively. Results are shown individually for the different search channels, the statistical combination of ML and $\gamma\gamma$+ML channels separately, and the statistical combination of all channels [14].

BIBLIOGRAPHY

[1] H. Hartley, *John dalton, f. r. s. (1766-1844) and the atomic theory—a lecture to commemorate his bicentenary*, Proceedings of the Royal Society of London. Series B. Biological Sciences **168** (1967) 335–359. 1

[2] G. E. Smith, *J. j. thomson and the electron: 1897-1899 an introduction*, Chem. Educator **2** (1997) 1–42. 1

[3] E. Rutherford, *Lxxix. the scattering of α and β particles by matter and the structure of the atom*, The London, Edinburgh, and Dublin Philosophical Magazine and Journal of Science **21** (1911) 669–688, [`https://doi.org/10.1080/14786440508637080`]. 1

[4] J. C. Maxwell, *A Dynamical Theory of the Electromagnetic Field*, *Philosophical Transactions of the Royal Society of London Series I* **155** (Jan., 1865) 459–512. 1

[5] M. Gell-Mann, *A Schematic Model of Baryons and Mesons*, Phys. Lett. **8** (1964) 214–215. 2

[6] G. Zweig, *An SU(3) model for strong interaction symmetry and its breaking. Version 2*, pp. 22–101. 2, 1964. 10.17181/CERN-TH-412. 2

[7] S. L. Glashow, *The renormalizability of vector meson interactions*, Nuclear Physics **10** (1959) 107–117. 2

[8] S. Weinberg, *A model of leptons*, Phys. Rev. Lett. **19** (Nov, 1967) 1264–1266. 2

[9] A. Salam and J. C. Ward, *Weak and electromagnetic interactions*, Il Nuovo Cimento (1955-1965) **11** (1959) 568–577. 2

[10] UA2 collaboration, P. Bagnaia et al., *Evidence for $Z^0 \to e^+e^-$ at the CERN $\bar{p}p$ Collider*, Phys. Lett. B **129** (1983) 130–140. 2

[11] CDF Collaboration collaboration, F. Abe, H. Akimoto, A. Akopian, M. G. Albrow, S. R. Amendolia, D. Amidei et al., *Observation of top quark production in $\overline{p}p$ collisions with the collider detector at fermilab*, Phys. Rev. Lett. **74** (Apr, 1995) 2626–2631. 2

[12] G. Aad, T. Abajyan, B. Abbott, J. Abdallah, S. Abdel Khalek, A. Abdelalim et al., *Observation of a new particle in the search for the standard model higgs boson with the atlas detector at the lhc*, Physics Letters B **716** (Sept., 2012) 1–29. 2

[13] S. Chatrchyan, V. Khachatryan, A. Sirunyan, A. Tumasyan, W. Adam, E. Aguilo et al., *Observation of a new boson at a mass of 125 gev with the cms experiment at the lhc*, Physics Letters B **716** (Sept., 2012) 30–61. 2

[14] ATLAS collaboration, G. Aad et al., *Search for non-resonant Higgs boson pair production in final states with leptons, taus, and photons in pp collisions at* $\sqrt{s} = 13$ *TeV with the ATLAS detector*, JHEP **08** (2024) 164, [2405.20040]. xiii, 3, 18, 100

[15] T. Chen and C. Guestrin, *Xgboost: A scalable tree boosting system*, in *Proceedings of the 22nd ACM SIGKDD International Conference on Knowledge Discovery and Data Mining*, pp. 785–794, ACM, Aug., 2016. DOI. 3

[16] A. Collaboration, "The coupling of the Higgs boson to fermions and bosons as a function of the particle's mass." 2015. ix, 5

[17] L. H. Ryder, *Quantum Field Theory*, ch. 8, pp. 290–315. Cambridge Univ. Press, Cambridge, 1994. 6

[18] N. Cabibbo, *Unitary symmetry and leptonic decays*, Phys. Rev. Lett. **10** (Jun, 1963) 531–533. 7

[19] M. Kobayashi and T. Maskawa, *Cp-violation in the renormalizable theory of weak interaction*, Progress of Theoretical Physics **49** (02, 1973) 652–657, [`https://academic.oup.com/ptp/article-pdf/49/2/652/5257692/49-2-652.pdf`]. 7

[20] Y. Fukuda, T. Hayakawa, E. Ichihara, K. Inoue, K. Ishihara, H. Ishino et al., *Evidence for oscillation of atmospheric neutrinos*, Physical Review Letters **81** (Aug., 1998) 1562–1567. 7

[21] SNO COLLABORATION collaboration, Q. R. Ahmad, R. C. Allen, T. C. Andersen, J. D. Anglin, G. Bühler, J. C. Barton et al., *Measurement of the rate of* $\nu_e + d \to p + p + e^-$ *interactions produced by* ^8b *solar neutrinos at the sudbury neutrino observatory*, Phys. Rev. Lett. **87** (Jul, 2001) 071301. 7

[22] T. D. Lee and C. N. Yang, *Parity nonconservation and a two-component theory of the neutrino*, Phys. Rev. **105** (Mar, 1957) 1671–1675. 7

[23] ATLAS collaboration, *Constraint of the Higgs boson self-coupling from Higgs boson differential production and decay measurements*, tech. rep., CERN, Geneva, 2019. ix, 14, 15

[24] S. Dawson, S. Dittmaier and M. Spira, *Neutral Higgs boson pair production at hadron colliders: QCD corrections*, Phys. Rev. D **58** (1998) 115012, [hep-ph/9805244]. 15

[25] S. Borowka, N. Greiner, G. Heinrich, S. P. Jones, M. Kerner, J. Schlenk et al., *Higgs Boson Pair Production in Gluon Fusion at Next-to-Leading Order with Full Top-Quark Mass Dependence*, Phys. Rev. Lett. **117** (2016) 012001, [1604.06447]. 15

[26] J. Baglio, F. Campanario, S. Glaus, M. Mühlleitner, M. Spira and J. Streicher, *Gluon fusion into Higgs pairs at NLO QCD and the top mass scheme*, Eur. Phys. J. C **79** (2019) 459, [1811.05692]. 15

[27] D. de Florian and J. Mazzitelli, *Higgs Boson Pair Production at Next-to-Next-to-Leading Order in QCD*, Phys. Rev. Lett. **111** (2013) 201801, [1309.6594]. 15

[28] D. Y. Shao, C. S. Li, H. T. Li and J. Wang, *Threshold resummation effects in Higgs boson pair production at the LHC*, JHEP **07** (2013) 169, [1301.1245]. 15

[29] D. de Florian and J. Mazzitelli, *Higgs pair production at next-to-next-to-leading logarithmic accuracy at the LHC*, *JHEP* **09** (2015) 053, [`1505.07122`]. 15

[30] M. Grazzini, G. Heinrich, S. Jones, S. Kallweit, M. Kerner, J. M. Lindert et al., *Higgs boson pair production at NNLO with top quark mass effects*, *JHEP* **05** (2018) 059, [`1803.02463`]. 15

[31] J. Baglio, F. Campanario, S. Glaus, M. Mühlleitner, J. Ronca and M. Spira, $gg \to HH$ *: Combined uncertainties*, *Phys. Rev. D* **103** (2021) 056002, [`2008.11626`]. 15

[32] S. Dawson, S. Dittmaier and M. Spira, *Neutral higgs-boson pair production at hadron colliders: Qcd corrections*, *Physical Review D* **58** (nov, 1998) 115012. 15

[33] J. Baglio, A. Djouadi, R. Gröber, M. M. Mühlleitner, J. Quevillon and M. Spira, *The measurement of the Higgs self-coupling at the LHC: theoretical status*, *JHEP* **04** (2013) 151, [`1212.5581`]. 16

[34] R. Frederix, S. Frixione, V. Hirschi, F. Maltoni, O. Mattelaer, P. Torrielli et al., *Higgs pair production at the LHC with NLO and parton-shower effects*, *Phys. Lett. B* **732** (2014) 142–149, [`1401.7340`]. 16

[35] L.-S. Ling, R.-Y. Zhang, W.-G. Ma, L. Guo, W.-H. Li and X.-Z. Li, *NNLO QCD corrections to Higgs pair production via vector boson fusion at hadron colliders*, *Phys. Rev. D* **89** (2014) 073001, [`1401.7754`]. 16

[36] F. A. Dreyer and A. Karlberg, *Fully differential Vector-Boson Fusion Higgs Pair Production at Next-to-Next-to-Leading Order*, *Phys. Rev. D* **99** (2019) 074028, [`1811.07918`]. 16

[37] F. A. Dreyer and A. Karlberg, *Vector-Boson Fusion Higgs Pair Production at* N^3LO, *Phys. Rev. D* **98** (2018) 114016, [`1811.07906`]. 16

[38] F. A. Dreyer, A. Karlberg, J.-N. Lang and M. Pellen, *Precise predictions for double-Higgs production via vector-boson fusion*, *Eur. Phys. J. C* **80** (2020) 1037, [`2005.13341`]. 16

[39] F. Monti, C. E. Pandini, F. L. Lucio Alves, H. Yang, Y. Huang, J. Wang et al., *Modelling of the single-Higgs simplified template cross-sections (STXS 1.2) for the determination of the Higgs boson trilinear self-coupling*, tech. rep., CERN, Geneva, 2022. ix, 17

[40] R. Frederix, S. Frixione, V. Hirschi, F. Maltoni, O. Mattelaer, P. Torrielli et al., *Higgs pair production at the lhc with nlo and parton-shower effects*, *Physics Letters B* **732** (may, 2014) 142–149. ix, 18

[41] ATLAS COLLABORATION collaboration, G. Aad, B. Abbott, K. Abeling, S. H. Abidi, A. Aboulhorma, H. Abramowicz et al., *Search for nonresonant pair production of higgs bosons in the* $b\bar{b}b\bar{b}$ *final state in pp collisions at* $\sqrt{s} = 13$ TeV *with the atlas detector*, *Phys. Rev. D* **108** (Sep, 2023) 052003. 18

[42] G. Aad, E. Aakvaag, B. Abbott, S. Abdelhameed, K. Abeling, N. Abicht et al., *Search for pair production of boosted higgs bosons via vector-boson fusion in the bb ¯bb ¯ final state using pp collisions at s=13tev with the atlas detector*, *Physics Letters B* **858** (2024) 139007. 18

[43] G. Aad, E. Aakvaag, B. Abbott, K. Abeling, N. Abicht, S. Abidi et al., *Search for the nonresonant production of higgs boson pairs via gluon fusion and vector-boson fusion in the $b\bar{b}\tau^+\tau^-$ final state in proton-proton collisions at $\sqrt{s} = 13$ TeV with the atlas detector*, Physical Review D **110** (Aug., 2024) . 18, 87

[44] G. Aad, B. Abbott, K. Abeling, N. J. Abicht, S. H. Abidi, A. Aboulhorma et al., *Studies of new higgs boson interactions through nonresonant hh production in the $b\bar{b}\gamma\gamma$ final state in pp collisions at $\sqrt{s} = 13$ tev with the atlas detector*, Journal of High Energy Physics **2024** (Jan., 2024) . 18

[45] G. Aad, B. Abbott, K. Abeling, N. J. Abicht, S. H. Abidi, A. Aboulhorma et al., *Search for non-resonant higgs boson pair production in the $2b + 2\ell + E_T^{miss}$ final state in pp collisions at $\sqrt{s} = 13$ tev with the atlas detector*, Journal of High Energy Physics **2024** (Feb., 2024) . 18

[46] ATLAS collaboration, G. Aad et al., *Combination of searches for Higgs boson pair production in pp collisions at $\sqrt{s} = 13$ TeV with the ATLAS detector*, `2406.09971`. x, 18, 19

[47] A. Tumasyan, W. Adam, J. Andrejkovic, T. Bergauer, S. Chatterjee, K. Damanakis et al., *Search for higgs boson pair production in the four b-quark final state in proton-proton collisions at $\sqrt{s} = 13$ TeV*, Physical Review Letters **129** (Aug., 2022) . 18

[48] A. Tumasyan, W. Adam, J. Andrejkovic, T. Bergauer, S. Chatterjee, K. Damanakis et al., *Search for nonresonant pair production of highly energetic higgs bosons decaying to bottom quarks*, Physical Review Letters **131** (July, 2023) . 18

[49] A. Tumasyan, W. Adam, J. Andrejkovic, T. Bergauer, S. Chatterjee, K. Damanakis et al., *Search for nonresonant higgs boson pair production in the final state with two bottom quarks and two tau leptons in proton-proton collisions at $\sqrt{s} = 13$ TeV*, Physics Letters B **842** (July, 2023) 137531. 18

[50] A. M. Sirunyan, A. Tumasyan, W. Adam, T. Bergauer, M. Dragicevic, A. Escalante Del Valle et al., *Search for nonresonant higgs boson pair production in final states with two bottom quarks and two photons in proton-proton collisions at $$ \sqrt{s} $$= 13 tev*, Journal of High Energy Physics **2021** (2021) 257. 18

[51] A. Tumasyan, W. Adam, J. W. Andrejkovic, T. Bergauer, S. Chatterjee, K. Damanakis et al., *Search for higgs boson pairs decaying to ww^*ww^*, $ww^*\tau\tau$, and $\tau\tau\tau\tau$ in proton-proton collisions at $\sqrt{s} = 13$ tev*, Journal of High Energy Physics **2023** (July, 2023) . 18, 68

[52] CMS collaboration, A. Tumasyan et al., *Search for nonresonant Higgs boson pair production in the four leptons plus twob jets final state in proton-proton collisions at $\sqrt{s}$ = 13 TeV*, JHEP **06** (2023) 130, [`2206.10657`]. 18

[53] A. Tumasyan, W. Adam, J. W. Andrejkovic, T. Bergauer, S. Chatterjee, K. Damanakis et al., *A portrait of the higgs boson by the cms experiment ten years after the discovery*, Nature **607** (2022) 60–68. 18

[54] B. Di Micco, M. Gouzevitch, J. Mazzitelli, C. Vernieri, J. Alison, K. Androsov et al., *Higgs boson pair production at colliders: status and perspectives. Higgs boson potential at colliders: Status and perspectives*, Rev. Phys. **5** (2020) 100045, [`1910.00012`]. ix, 19

[55] L. R. Evans and P. Bryant, *LHC Machine*, *JINST* **3** (2008) S08001. 20, 21, 22

[56] Y. Nakahama and on behalf of the ATLAS Collaboration, *The atlas trigger system: Ready for run-2*, *Journal of Physics: Conference Series* **664** (dec, 2015) 082037. 20, 36

[57] N. Garelli, *Performance of the ATLAS Detector in Run-2*, *EPJ Web Conf.* **164** (2017) 01021. 20, 36

[58] B. Salvachua, *Overview of Proton-Proton Physics during Run 2*, . x, xiv, 21, 22

[59] R. Scrivens, M. Kronberger, D. Küchler, J. Lettry, C. Mastrostefano, O. Midttun et al., *Overview of the status and developments on primary ion sources at CERN**, . 22

[60] *The Large Electron-Positron Collider*, . 22

[61] J. P. Blewett, *200-gev intersecting storage accelerators., pp 501-4 of Proceedings of the 8th International Conference on High- Energy Accelerators, CERN 1971. /Blewett, M. Hildred (ed.). Geneva European Organization for Nuclear Research (1971).* (01, 1971) . 23

[62] E. Bleser, J. Cottingham, P. Dahl, R. Engelmann, R. Fernow, M. Garber et al., *Superconducting magnets for the cba project*, *Nuclear Instruments and Methods in Physics Research Section A: Accelerators, Spectrometers, Detectors and Associated Equipment* **235** (1985) 435–463. 23

[63] Brookhaven National Laboratory, *Colliding beam accelerator*, *CBA Newsletter* (Nov., 1982) 27–31. 23

[64] LHCb collaboration, A. A. Alves, L. M. Andrade, F. Barbosa-Ademarlaudo, I. Bediaga, G. Cernicchiaro, G. Guerrer et al., *The LHCb Detector at the LHC*, *JINST* **3** (2008) S08005. 23

[65] ALICE collaboration, K. Aamodt et al., *The ALICE experiment at the CERN LHC*, *JINST* **3** (2008) S08002. 23

[66] CMS collaboration, S. Chatrchyan, G. Hmayakyan, V. Khachatryan, A. M. Sirunyan, R. Adolphi, G. Anagnostou et al., *The CMS experiment at the CERN LHC. The Compact Muon Solenoid experiment*, *JINST* **3** (2008) S08004. 23

[67] ATLAS collaboration, G. Aad, S. Bentvelsen, G. J. Bobbink, K. Bos, H. Boterenbrood, G. Brouwer et al., *The ATLAS Experiment at the CERN Large Hadron Collider*, *JINST* **3** (2008) S08003. x, xiv, 23, 25, 27, 28, 29, 30, 33, 34, 35

[68] E. Mobs, *The CERN accelerator complex - August 2018. Complexe des accélérateurs du CERN - Août 2018*, . x, 24

[69] B. Mindur, *ATLAS Transition Radiation Tracker (TRT): Straw tubes for tracking and particle identification at the Large Hadron Collider*, tech. rep., CERN, Geneva, 2017. 10.1016/j.nima.2016.04.026. 29

[70] A. Lechner, *Particle interactions with matter*, *CERN Yellow Rep. School Proc.* **5** (2018) 47. 29

[71] W. Heitler, *The Quantum Theory of Radiation.* Clarendon Press, Oxford, 1954. 30

[72] ATLAS collaboration, *ATLAS tile calorimeter: Technical Design Report*. Technical design report. ATLAS. CERN, Geneva, 1996, 10.17181/CERN.JRBJ.7O28. 32

[73] ATLAS collaboration, *ATLAS muon spectrometer: Technical Design Report*. Technical design report. ATLAS. CERN, Geneva, 1997. 34

[74] ATLAS collaboration, Z. Marshall, *Simulation of Pile-up in the ATLAS Experiment*, *J. Phys. Conf. Ser.* **513** (2014) 022024. 35

[75] ATLAS collaboration, *ATLAS level-1 trigger: Technical Design Report*. Technical design report. ATLAS. CERN, Geneva, 1998. 36

[76] ATLAS collaboration, P. Jenni, M. Nessi, M. Nordberg and K. Smith, *ATLAS high-level trigger, data-acquisition and controls: Technical Design Report*. Technical design report. ATLAS. CERN, Geneva, 2003. 36

[77] T. A. collaboration, *Operation of the atlas trigger system in run 2*, *Journal of Instrumentation* **15** (oct, 2020) P10004. x, 36

[78] J. M. Campbell, J. W. Huston and W. J. Stirling, *Hard interactions of quarks and gluons: a primer for lhc physics*, *Reports on Progress in Physics* **70** (Dec., 2006) 89–193. 38

[79] ATLASandCMSs collaboration, A. D. Pilkington, *Soft-QCD at the LHC*, tech. rep., CERN, Geneva, 2012. 38

[80] S. Höche, *Introduction to parton-shower event generators*, in *Theoretical Advanced Study Institute in Elementary Particle Physics: Journeys Through the Precision Frontier: Amplitudes for Colliders*, pp. 235–295, 2015. `1411.4085`. DOI. 38

[81] ATLAS Collaboration, "Introduction to monte carlo simulation." https://atlassoftwaredocs.web.cern.ch/analysis-software/AnalysisSWTutorial/mc_intro/, n.d. 38

[82] J. Alwall, R. Frederix, S. Frixione, V. Hirschi, F. Maltoni, O. Mattelaer et al., *The automated computation of tree-level and next-to-leading order differential cross sections, and their matching to parton shower simulations*, *Journal of High Energy Physics* **2014** (2014) 79. 38

[83] E. Bothmann, G. S. Chahal, S. Höche, J. Krause, F. Krauss, S. Kuttimalai et al., *Event generation with Sherpa 2.2*, *SciPost Phys.* **7** (2019) 034. 38

[84] S. Alioli, P. Nason, C. Oleari and E. Re, *A general framework for implementing nlo calculations in shower monte carlo programs: the powheg box*, *Journal of High Energy Physics* **2010** (2010) 43. 38

[85] T. Sjöstrand, S. Mrenna and P. Skands, *A brief introduction to PYTHIA 8.1*, *Comput. Phys. Commun.* **178** (2008) 852–867, [`0710.3820`]. 38, 49

[86] M. Bähr, S. Gieseke, M. A. Gigg, D. Grellscheid, K. Hamilton, O. Latunde-Dada et al., *Herwig++ physics and manual*, *The European Physical Journal C* **58** (2008) 639–707. 38

[87] GEANT4 collaboration, S. Agostinelli et al., *GEANT4 - A Simulation Toolkit*, *Nucl. Instrum. Meth. A* **506** (2003) 250–303. 38, 49

[88] ATLAS collaboration, *The ATLAS Collaboration Software and Firmware*, tech. rep., CERN, Geneva, 2021. 39

[89] M. Aaboud, G. Aad, B. Abbott, J. Abdallah, O. Abdinov, B. Abeloos et al., *Performance of the atlas track reconstruction algorithms in dense environments in lhc run 2*, The European Physical Journal C **77** (Oct., 2017) . 39

[90] ATLAS Collaboration, "Vertex Reconstruction Performance of the ATLAS Detector at $\sqrt{s} = 13$ TeV." ATL-PHYS-PUB-2015-026, 2015. 40

[91] G. Aad, B. Abbott, J. Abdallah, O. Abdinov, R. Aben, M. Abolins et al., *Topological cell clustering in the atlas calorimeters and its performance in lhc run 1*, The European Physical Journal C **77** (July, 2017) . 40

[92] T. Vazquez Schroeder, R. Polifka, X. Poveda Torres, M. N. Agaras, B. Ali, S. Angelidakis et al., *Search for the Associated Production of a Higgs Boson and a Top Quark Pair in multilepton final states in 80 fb^{-1} pp Collisions at $\sqrt{s} = 13$ TeV with the ATLAS Detector*, tech. rep., CERN, Geneva, 2018. 41

[93] M. Cacciari, G. P. Salam and G. Soyez, *FastJet User Manual*, Eur. Phys. J. C **72** (2012) 1896, [`1111.6097`]. 43

[94] M. Cacciari, G. P. Salam and G. Soyez, *The anti-k_t jet clustering algorithm*, JHEP **04** (2008) 063, [`0802.1189`]. 43

[95] ATLAS collaboration, *Identification of hadronic tau lepton decays using neural networks in the ATLAS experiment*, tech. rep., CERN, Geneva, 2019. 43

[96] T. Barillari, E. Bergeaas Kuutmann, T. Carli, J. Erdmann, P. Giovannini, K. J. Grahn et al., *Local Hadronic Calibration*, tech. rep., CERN, Geneva, 2008. 43

[97] ATLAS collaboration, *Measurement of the tau lepton reconstruction and identification performance in the ATLAS experiment using pp collisions at $\sqrt{s} = 13$ TeV*, tech. rep., CERN, Geneva, 2017. 44, 61, 76

[98] M. Aaboud, G. Aad, B. Abbott, J. Abdallah, O. Abdinov, B. Abeloos et al., *Jet reconstruction and performance using particle flow with the atlas detector*, The European Physical Journal C **77** (2017) 466. 44

[99] G. Aad, B. Abbott, J. Abdallah, O. Abdinov, R. Aben, M. Abolins et al., *Performance of pile-up mitigation techniques for jets in $$pp$$collisions at $$\sqrt{s}=8$$ tev using the atlas detector*, The European Physical Journal C **76** (2016) 581. 44

[100] ATLAS collaboration, G. Aad et al., *ATLAS flavour-tagging algorithms for the LHC Run 2 pp collision dataset*, Eur. Phys. J. C **83** (2023) 681, [`2211.16345`]. 45

[101] ATLAS collaboration, G. Aad et al., *The performance of missing transverse momentum reconstruction and its significance with the ATLAS detector using 140 fb^{-1} of $\sqrt{s} = 13$ TeV pp collisions*, `2402.05858`. 45

[102] ATLAS collaboration, A. Hrynevich, *ATLAS jet and missing energy reconstruction, calibration and performance in LHC Run-2*, Tech. Rep. 06, CERN, Geneva, 2017. 10.1088/1748-0221/12/06/C06038. 45

[103] G. Aad, B. Abbott, K. Abeling, S. H. Abidi, A. Aboulhorma, H. Abramowicz et al., *Luminosity determination in pp collisions at $$\sqrt{s}=13$$ tev using the atlas detector at the lhc*, The European Physical Journal C **83** (2023) 982. 46, 84

[104] G. Avoni et al., *The new LUCID-2 detector for luminosity measurement and monitoring in ATLAS*, *JINST* **13** (2018) P07017. 46

[105] ATLAS Collaboration, "ATLAS Pythia 8 tunes to 7 TeV data." ATL-PHYS-PUB-2014-021, 2014. 47, 48

[106] NNPDF collaboration, R. D. Ball et al., *Parton distributions for the LHC Run II*, *JHEP* **04** (2015) 040, [1410.8849]. 47, 48, 50

[107] D. J. Lange, *The EvtGen particle decay simulation package*, *Nucl. Instrum. Meth. A* **462** (2001) 152. 47, 48, 49

[108] ATLAS Collaboration, "The simulation principle and performance of the ATLAS fast calorimeter simulation FastCaloSim." ATL-PHYS-PUB-2010-013, 2010. 47, 48

[109] ATLAS collaboration, *Validation of signal Monte Carlo event generation in searches for Higgs boson pairs with the ATLAS detector*, tech. rep., CERN, Geneva, 2019. 47

[110] J. Alwall, R. Frederix, S. Frixione, V. Hirschi, F. Maltoni, O. Mattelaer et al., *The automated computation of tree-level and next-to-leading order differential cross sections, and their matching to parton shower simulations*, *JHEP* **07** (2014) 079, [1405.0301]. 48, 49

[111] ATLAS Collaboration, "The Pythia 8 A3 tune description of ATLAS minimum bias and inelastic measurements incorporating the Donnachie–Landshoff diffractive model." ATL-PHYS-PUB-2016-017, 2016. 49

[112] ATLAS Collaboration, *The ATLAS Simulation Infrastructure*, *Eur. Phys. J. C* **70** (2010) 823, [1005.4568]. 49

[113] T. Sjöstrand, S. Mrenna and P. Skands, *A brief introduction to pythia 8.1*, *Comput. Phys. Commun.* **178** (2008) 852, [0710.3820]. 49

[114] J. Bellm et al., *Herwig 7.0/Herwig++ 3.0 release note*, *Eur. Phys. J. C* **76** (2016) 196, [1512.01178]. 49

[115] T. Gleisberg et al., *Event generation with sherpa 1.1*, *JHEP* **02** (2009) 007, [0811.4622]. 49

[116] F. Cascioli, P. Maierhöfer and S. Pozzorini, *Scattering Amplitudes with Open Loops*, *Phys. Rev. Lett.* **108** (2012) 111601, [1111.5206]. 49

[117] T. Gleisberg and S. Höche, *Comix, a new matrix element generator*, *JHEP* **12** (2008) 039, [0808.3674]. 49

[118] S. Schumann and F. Krauss, *A parton shower algorithm based on Catani–Seymour dipole factorisation*, *JHEP* **03** (2008) 038, [0709.1027]. 49

[119] S. Höche, F. Krauss, M. Schönherr and F. Siegert, *QCD matrix elements + parton showers. The NLO case*, *JHEP* **04** (2013) 027, [1207.5030]. 49

[120] P. Golonka and Z. Was, *PHOTOS Monte Carlo: a precision tool for QED corrections in Z and W decays*, *Eur. Phys. J. C* **45** (2006) 97–107, [`hep-ph/0506026`]. 49

[121] S. Frixione, G. Ridolfi and P. Nason, *A positive-weight next-to-leading-order monte carlo for heavy flavour hadroproduction*, *JHEP* **09** (2007) 126, [`0707.3088`]. 50

[122] E. Re, *Single-top wt-channel production matched with parton showers using the powheg method*, *Eur. Phys. J. C* **71** (2011) 1547, [`1009.2450`]. 50

[123] S. Alioli, P. Nason, C. Oleari and E. Re, *Nlo single-top production matched with shower in powheg: $s-$ and $t-$channel contributions*, *JHEP* **09** (2009) 111, [`0907.4076`]. 50

[124] R. Brun and F. Rademakers, *Root — an object oriented data analysis framework*, *Nuclear Instruments and Methods in Physics Research Section A: Accelerators, Spectrometers, Detectors and Associated Equipment* **389** (1997) 81–86. 51

[125] TMVA collaboration, A. Hocker et al., *TMVA - Toolkit for Multivariate Data Analysis*, `physics/0703039`. 51

[126] J. Ye, J.-H. Chow, J. Chen and Z. Zheng, *Stochastic gradient boosted distributed decision trees*, pp. 2061–2064, 11, 2009. DOI. 51

[127] T. Akiba, S. Sano, T. Yanase, T. Ohta and M. Koyama, *Optuna: A next-generation hyperparameter optimization framework*, in *Proceedings of the 25th ACM SIGKDD International Conference on Knowledge Discovery and Data Mining*, 2019. 55

[128] S. Geisser, *The predictive sample reuse method with applications*, *Journal of the American Statistical Association* **70** (1975) 320–328. 56

[129] M. N. Agaras et al., *Search for non-resonant di-Higgs production with multiple lepton final states using 139 fb^{-1} proton-proton collision data at $\sqrt{s} = 13$ TeV recorded by the ATLAS detector*, 2020. 70

[130] ATLAS collaboration, G. Aad et al., *Electron and photon efficiencies in LHC Run 2 with the ATLAS experiment*, *JHEP* **05** (2024) 162, [`2308.13362`]. 85

[131] ATLAS collaboration, G. Aad et al., *Muon reconstruction and identification efficiency in ATLAS using the full Run 2 pp collision data set at $\sqrt{s} = 13$ TeV*, *Eur. Phys. J. C* **81** (2021) 578, [`2012.00578`]. 85

[132] ATLAS Collaboration, *Jet energy scale measurements and their systematic uncertainties in proton–proton collisions at $\sqrt{s} = 13$ TeV with the ATLAS detector*, *Phys. Rev. D* **96** (2017) 072002, [`1703.09665`]. 85

[133] ATLAS collaboration, G. Aad et al., *Atlas b-jet identification performance and efficiency measurement with $t\bar{t}$ events in pp collisions at $\sqrt{s} = 13$ tev*, *Eur. Phys. J. C* **79** (2019) 970, [`1907.05120`]. 85

[134] ATLAS collaboration, G. Aad et al., *Measurement of the c-jet mistagging efficiency in $t\bar{t}$ events using pp collision data at $\sqrt{s} = 13$ TeV collected with the ATLAS detector*, *Eur. Phys. J. C* **82** (2022) 95, [`2109.10627`]. 85

[135] ATLAS collaboration, G. Aad et al., *Calibration of the light-flavour jet mistagging efficiency of the b-tagging algorithms with Z+jets events using 139 fb*$^{-1}$ *of ATLAS proton–proton collision data at* $\sqrt{s} = 13$ *TeV*, *Eur. Phys. J. C* **83** (2023) 728, [`2301.06319`]. 85

[136] M. Grazzini, G. Heinrich, S. Jones, S. Kallweit, M. Kerner, J. M. Lindert et al., *Higgs boson pair production at nnlo with top quark mass effects*, *Journal of High Energy Physics* **2018** (May, 2018) 59. 86

[137] "LHCHXSWGHH." https://twiki.cern.ch/twiki/bin/view/LHCPhysics/LHCHWGHH?redirectedfrom=LHCPhysics.LHCHXSWGHH. 86

[138] "ttH cross section." https://twiki.cern.ch/twiki/bin/view/LHCPhysics/CERNYellowReportPageAt13TeV. 86

[139] ATLAS, *Measurement of the Higgs boson production cross section in association with a vector boson and decaying into* WW^* *with the ATLAS detector at* $\sqrt{s} = 13\,\text{TeV}$, tech. rep., CERN, Geneva, 2021. 87

[140] G. Cowan, K. Cranmer, E. Gross and O. Vitells, *Asymptotic formulae for likelihood-based tests of new physics*, *Eur. Phys. J. C* **71** (2011) 1554, [`1007.1727`]. 90